FRICTION IN ELASTO-HYDRODYNAMIC LUBRICATION

Benoit Jacod

The research project was supported by and carried out at SKF Engineering and Research Centre in Nieuwegein. The support is gratefully acknowledged.

ISBN: 90-365-1782-6

Printed by FEBOdruk B.V., Enschede.

FRICTION IN ELASTO-HYDRODYNAMIC LUBRICATION

ter verkrijging van
de graad van doctor aan de Universiteit Twente,
op gezag van de rector magnificus,
prof.dr. F.A. van Vught,
volgens besluit van het College voor Promoties
in het openbaar te verdedigen
op donderdag 29 augustus 2002 te 16.45 uur

door

Benoit Clément Jacod

geboren op 16 april 1976
te Parijs, Frankrijk

Dit proefschrift is goedgekeurd door:

Promotor:	Prof.dr.ir. H.W.M. Hoeijmakers
Assistent–promotor:	Dr.ir. C.H. Venner

à Anne-Laure

Abstract

The purpose of rolling bearings in mechanical systems is to transmit force while permitting rotary motion with a minimal contribution to the frictional losses. Their successful operation depends on the presence of a very thin lubricant film in the contacts between the rolling elements and the rings. The lubrication regime characteristic for such contacts is referred to as elasto-hydrodynamic lubrication (EHL). In this regime the friction in the lubricated contact is caused by the shear of the highly pressurized lubricant film. In recent years down-sizing and increasingly severe operating conditions have led to a reduction of the film thickness levels in practical applications to the point where the influence of surface roughness becomes significant. Accurate prediction of the friction for the purpose of control and optimisation requires detailed understanding of the response of a highly pressurized lubricant film under shear and of the influence of roughness on this response.

Many experiments have been carried out over the years in which the friction coefficient has been measured in EHL contacts between smooth surfaces. Theoretical predictions by means of numerical simulations aimed at the derivation of general formula to predict this friction are rare. With respect to the specific influence of roughness on friction in the EHL regime very little is known. The objective of this thesis is to fill this gap and to study the friction generation mechanism in EHL contacts under rolling/sliding in a systematic way. This is done by means of numerical simulations. Existing rheological models have been incorporated in numerical solvers for the EHL contact problem. These solvers are based on multilevel techniques which by their efficiency allow very detailed simulations in short computing times. As a result computations could be done for many cases varying the operating conditions over the entire range relevant for practical applications in bearings.

First the case of smooth isothermal EHL contacts was considered using the Eyring model and limiting shear stress models to describe the lubricant behaviour. It is shown that the friction generation mechanisms can be characterized by a shear stress. The friction data calculated for these models are shown to form one curve when plotted as a function of this characteristic shear stress. This curve forms a generalized traction curve and its shape is shown to reflect the rheological model that is used to describe the lubricant behaviour. Curve fit relations are presented for these mastercurves. They constitute simple and accurate engineering tools for the prediction of the (nominal level of the) friction. Subsequently these mastercurves have been validated by comparing the predictions with experimental results published in the literature.

Because of the assumption of isothermal behaviour the derived relations are only accurate for small slip values. To extend the range of validity of the friction mastercurves to higher shear rates where frictional heating becomes significant a thermal correction approach has been developed. The friction mastercurves combined with a thermal dry contact analysis enable the calculation of an estimate of the maximum temperature increase in the centre of the film and the temperature at the surface. Subsequently a correction to the computed friction coefficient due to increased temperature can be given. The results of this simplified approach have been compared with the results of full numerical simulations in which thermal effects are taken into account. It is shown that, even though the approach involves major simplifications, it gives an accurate estimate of the effect of the temperature rise on the friction. Moreover, for cases where the lubricant characteristics are accurately known the agreement of the predictions with experimentally measured friction values is good.

Finally the effect of surface roughness on the friction is investigated. The study is restricted to the case of longitudinal roughness which is the predominant pattern found on bearing rings. Using the Eyring model to describe the lubricants rheological behaviour numerical simulations have been carried out. First the relative friction variations caused by a single harmonic roughness component were computed as a function of the amplitude and wavelength for a wide range of operating conditions. From the results a curve fit formula has been derived for the relative friction variation as a function of the out-of-contact geometry of the waviness and a newly derived parameter characterizing the response of the lubricant to pressure variations. Subsequently, the case of a superposition of two harmonic components has been considered. It is shown that for the effect on friction such a combined pattern can be represented by a single equivalent wave. The amplitude and the wavelength of the equivalent wave can be determined from a non-linear relation in terms of the amplitudes and wavelengths of the individual harmonic components. Finally the approach has been applied to the prediction of the effect of a real roughness profile (many components) on the friction. By means of full numerical simulations it is shown that even for the case of a real measured longitudinal roughness pattern this simplified approach based on the definition of an equivalent single component gives accurate results. It is concluded that the single component curve-fit formula and the definition of the equivalent waviness together form a simple engineering tool for the prediction of the effect on friction of any arbitrary longitudinal roughness profile.

Samenvatting

In veel mechanische systemen wordt een wentellager toegepast om de wrijving als gevolg van een roterende beweging te minimaliseren. Om een lange levensduur te garanderen is het noodzakelijk dat zich tussen de rollende elementen en de ringen van het lager een smeerfilm bevindt die de oppervlakken volledig scheidt. In dit smeringsregime, aangeduid met de term elastohydrodynamische smering (EHL), wordt de wrijving veroorzaakt door de afschuiving in de smeerfilm. De steeds extremere condities waaronder wentellagers de laaste jaren moeten functioneren hebben geleid tot een afname van de filmdikte met als gevolg dat de ruwheid van de oppervlakken van steeds grotere invloed wordt op het functioneren van het contact. Om de wrijving in applicaties dan goed te kunnen voorspellen en te kunnen optimaliseren is het noodzakelijk dat zowel de afschuiving van de oliefilm onder hoge druk als de effecten van de ruwheid op dit gedrag nauwkeurig voorspeld kunnen worden.

In de loop der jaren zijn veel experimenten uitgevoerd waarbij de wrijvingscoëfficiënt in een EHL contact is gemeten voor het geval van zeer gladde oppervlakken. Theoretische resultaten gericht op het gebied van voorspelling door middel van bijvoorbeeld numerieke simulaties zijn echter zeldzaam en naar de effecten van de ruwheid op de wrijving is nauwelijks experimenteel of theoretisch onderzoek gedaan. Het doel van dit onderzoek is om in deze lacune te voorzien. Door middel van numerieke simulaties is het wrijvingsgedrag van EHL contacten in relatie tot de operationele condities in kaart gebracht. Voor deze numerieke simulaties is een algoritme gebaseerd op multilevel technieken gebruikt. Deze technieken maken het door hun efficiëncy mogelijk om nauwkeurige simulaties uit te voeren in korte tijd. Ze zijn dus uitermate geschikt voor parameter studies waarbij veel berekeningen nodig zijn als gevolg van de vele mogelijke praktische condities.

Als eerste stap is de situatie van ideaal gladde oppervlaken en isotherme condities beschouwd. Voor het reologische gedrag van de vloeistof zijn de twee meest geaccepteerde modellen gebruikt, te weten het Eyring model en het limiting shear stress model. De resultaten van de numerieke simulaties laten zien dat voor beide modellen de wrijving in het EHL contact nauwkeurig beschreven kan worden met behulp van een unieke parameter, een karakteristieke schuifspanning. Voor elk van de modellen kunnen de resultaten voor alle mogelijke operationele condities met een gegeneraliseerde wrijvingscurve beschreven worden. Voor deze curves worden eenvoudige formules gegeven die in de praktijk als hulpmiddel bij het ontwerpen van lager-produkten gebruikt kunnen worden. Het gevonden gedrag is vervolgens gevalideerd met de resultaten van experimenten zoals die in de literatuur gepubliceerd

zijn.

Wanneer de afschuifsnelheden groot zijn is de aanname van isotherme condities niet meer gerechtvaardigd. Om de geldigheid van de gegeneraliseerde wrijvingscurves uit te breiden naar situaties van hogere afschuifsnelheden waar warmteontwikkeling een rol gaat spelen is een vereenvoudigd model ontwikkeld. De gevonden relaties voor de isotherme situatie zijn gecombineerd met een eenvoudig model dat de warmteontwikkeling in een droog contact voorspelt. Met deze aanpak is het mogelijk om op een eenvoudige manier een benadering te krijgen van zowel de temperatuur in het midden van de smeerfilm als de temperatuur van de beide oppervlakken en het effect van de temperatuurverhoging op de wrijvingscoëfficiënt. Een vergelijking van de resultaten van dit model met de resultaten van een volledige analyse laat zien dat deze eenvoudige benadering al een goede voorspelling geeft. Bovendien is er een goede overeenkomst tussen de voorspellingen en experimentele resultaten. Voorwaarde voor een goed resultaat is wel dat de eigenschappen van het smeermiddel nauwkeurig bekend moeten zijn.

Nadat het wrijvingsgedrag voor het geval van ideaal gladde oppervlakken nauwkeurig in kaart is gebracht wordt de invloed van oppervlakteruwheid op de wrijving bestudeerd voor het geval van longitudinale patronen. Dit is de meest voorkomende vorm van ruwheid op de binnen en buiten ringen van wentellagers. Voor de beschrijving van het vloeistofgedrag is gebruik gemaakt van het Eyring model. Als eerste stap is de relatieve verandering van de wrijving berekend als gevolg van een enkele harmonische ruwheidscomponent als functie van de amplitude en golflengte van de component en de condities van het contact. Uit de resultaten van de numerieke simulaties zijn curve-fit formules afgeleid die de relatieve verandering van de wrijving voorspellen als functie van de golfgeometrie en een nieuw ontwikkelde parameter die de reactie van het smeermiddel op de drukvariaties vertegenwoordigt. Vervolgens is het geval van een patroon bestaande uit twee harmonische componenten beschouwd. Met behulp van de resultaten voor de enkele harmonische component wordt aangetoond dat het effect van de combinatie van twee harmonische componenten op de wrijving beschreven kan worden als het effect van een equivalente enkele component. De golflengte en amplitude van deze equivalente component kunnen bepaald worden uit een niet-lineaire combinatie van de amplitudes en golflengtes van de twee harmonische componenten. Deze aanpak van het representeren van meerdere harmonische componenten door een enkele equivalente harmonische component is vervolgens toegepast op het geval van gemeten ruwheidsprofielen. Met behulp van volledige numerieke simulaties wordt aangetoond dat ook voor deze situatie met behulp van de definitie van de equivalente enkele component en de bijbehorende curve-fit formule voor de wrijvingsverandering een goede voorspelling gegeven kan worden van het effect van het ruwheidsprofiel op de wrijving. Met de afgeleide relaties kan op eenvoudige wijze het effect van een willekeurig longitudinaal ruwheidsprofiel op de wrijving voorspeld worden zonder dat daarvoor uitgebreide numerieke simulaties nodig zijn. Dit maakt de relaties tot een uitstekend gereedschap voor een ontwerp omgeving.

Contents

Nomenclature

a	Hertzian half-contact length (elliptic contact)	$a = (3fR/E')^{1/3}(2\kappa\mathcal{E}/\pi)^{1/3}$	[m]
A	amplitude of the waviness		[m]
$\mathcal{A}$	dimensionless amplitude	$\mathcal{A} = A/c$	-
$\mathcal{A}^*$	dimensionless equivalent amplitude		-
$\bar{\mathcal{A}}$	dimensionless relative amplitude	$\bar{\mathcal{A}} = \mathcal{A}/H_c$	-
b	Hertzian half-contact width (elliptic contact)	$b = \kappa/a$	[m]
	Hertzian half-contact length (line contact)	$b = \sqrt{8wR/(\pi E')}$	[m]
c	Hertzian approach	$c = (a^2/(2R))(\mathcal{K}/\mathcal{E})$	[m]
D	ellipticity ratio	$D = R_x/R_y$	-
E	modulus of elasticity	[Pa]	
E'	reduced modulus of elasticity	$2/E' = (1-\nu_1^2)/E_1 + (1-\nu_2^2)/E_2$	[Pa]
$\mathcal{E}$	elliptic integral (second kind)		-
f	load (elliptic contact)		[N]
h	film thickness		[m]
	mesh-size		-
h_0	integration constant		[m]
H	dimensionless film thickness	$H = h/c$	-
H_c	dimensionless central film thickness	$H_c = h/(R_x(\eta_0 u_s/(E'R_x))^{1/2})$	-
K	kernel		-
	thermal conductivity		[$\mathrm{Wm^{-1}K^{-1}}$]
$\mathcal{K}$	elliptic integral (first kind)		-
L	dimensionless lubricant parameter (elliptic contact)	$L = \alpha E'(\eta_0 u_s/(E'R_x))^{1/4}$	-
	(line contact)	$L = \alpha E'(\eta_0 u_s/(E'R))^{1/4}$	-
M	dimensionless load parameter (elliptic contact)	$M = f/(E'R_x^2)(E'R_x/(\eta_0 u_s))^{3/4}$	-
	(line contact)	$M = w/(E'R)(E'R_x/(\eta_0 u_s))^{1/2}$	-
n	rheological index		-
	number of discretization points		-
N_1	dimensionless non-Newtonian number	$N_1 = \lambda p_H^2 \mathcal{K}/(6E'\tau_r)$	-
N_2	dimensionless non-Newtonian number	$N_2 = 2p_H^2 \mathcal{K}/(E'\tau_r)$	-

p	pressure		[Pa]
p_H	maximum Hertzian pressure		
	(elliptic contact)	$p_H = 3f/(2\pi ab)$	[Pa]
	(line contact)	$p_H = 2w/(\pi b)$	[Pa]
p^*	reduced pressure	$p^* = p_H(1 - \chi p_H/(10^9 + p_H))$	[Pa]
p_r	constant	$p_r = 1.96\ 10^8$	[Pa]
P	dimensionless pressure	$P = p/p_H$	-
Pe	Péclet number	$Pe = (u_2 - u_1)a/\kappa$	-
R_x	reduced radius of curvature in the x-direction	$R_x^{-1} = R_{x1}^{-1} + R_{x2}^{-1}$	[m]
R_y	reduced radius of curvature in the y-direction	$R_y^{-1} = R_{y1}^{-1} + R_{y2}^{-1}$	[m]
R	reduced radius of curvature		
	(elliptic contact)	$R^{-1} = R_y^{-1} + R_x^{-1}$	[m]
	(line contact)	$R^{-1} = R_1^{-1} + R_2^{-1}$	[m]
R_q	rms of the surface roughness		[m]
S	slide/roll ratio	$S = 2(u_2 - u_1)/(u_2 + u_1)$	-
$\bar{S}$	dimensionless non-Newtonian parameter	$\bar{S} = SE'/\tau_r(\eta_0 u_s/(E'R_x))^{1/2}$	-
$\mathcal{S}$	shape factor	$\mathcal{S} = (\mathcal{E} - \kappa^2\mathcal{K})/(\mathcal{K}(1-\kappa^2))$	-
T	temperature		[°C]
T_0	inlet temperature		[°C]
δT	temperature increase		[°C]
u	velocity in the running direction		[m s^{-1}]
u_s	sum speed	$u_s = u_1 + u_2$	[m s^{-1}]
u_m	average speed	$u_m = (u_1 + u_2)/2$	[m s^{-1}]
v	velocity in the transverse direction		[m s^{-1}]
w	load (line contact)		[N]
W	wavelength of the waviness		[m]
$\mathcal{W}$	dimensionless waviness	$\mathcal{W} = W/b$	-
$\mathcal{W}^*$	dimensionless equivalent waviness		-
x	coordinate in the running direction		[m]
x_0	characteristic length (line contact)		[m]
X	dimensionless coordinate		
	(elliptic contact)	$X = x/a$	-
	(line contact)	$X = x/b$	-
y	coordinate in the transverse direction		[m]
Y	dimensionless coordinate	$Y = y/b$	-
z	coordinate in the vertical direction		[m]
z_R	pressure viscosity index (Roelands)	$z_R = p_r\alpha/(\ln(\eta_0) + 9.67)$	-
Z	dimensionless coordinate	$Z = z/c$	-
α	pressure viscosity coefficient		[Pa^{-1}]
$\bar{\alpha}$	dimensionless viscosity parameter	$\bar{\alpha} = \alpha p_H$	-
β	temperature viscosity coefficient		[°C^{-1}]
γ	pressure limiting shear stress coefficient		-

Γ	roughness parameter	$\Gamma = p_H/\bar{\mu}(\partial\bar{\mu}/\partial\bar{\tau}_c)(\partial\bar{\tau}_c/\partial P)$	-
$\dot{\gamma}$	shear rate		[s^{-1}]
δ	mutual approach		[m]
Δ	dimensionless mutual approach	$\Delta = \delta/c$	-
ϵ	coefficient	$\epsilon = \bar{\rho}H^3/(\bar{\eta}\lambda)$	-
η	viscosity		[Pa s]
η_0	viscosity at ambiant pressure		[Pa s]
$\eta_{x,y}$	effective viscosity		[Pa s]
$\bar{\eta}$	dimensionless viscosity	$\bar{\eta} = \eta/\eta_0$	-
$\bar{\eta}_{X,Y}$	dimensionless effective viscosity	$\bar{\eta}_{X,Y} = \eta_{x,y}/\eta_0$	-
θ	constant		-
κ	ellipticity ratio	$\kappa = a/b$	-
	diffusivity		[m^{2}s^{-1}]
λ	dimensionless parameter		
	(elliptic contact)	$\lambda = 6u_s\eta_0 a/(c^2 p_H)$	-
	(line contact)	$\lambda = 12\eta_0 u_m R^2/(b^3 p_H)$	-
μ	coefficient of friction		-
$\bar{\mu}$	reduced coefficient of friction	$\bar{\mu} = \mu p_H/\tau_r$	-
ρ	density		[kg m^3]
ρ_0	density at ambiant pressure		[kg m^3]
$\bar{\rho}$	dimensionless density	$\bar{\rho} = \rho/\rho_0$	-
σ	standard deviation		-
Σ	non-Newtonian coefficient (line contact)	$\Sigma = N_2 H(\partial P)/(\partial X)$	-
τ	shear stress		[Pa]
τ_0	Eyring stress		[Pa]
τ_L	limiting shear stress	$\tau_L = \tau_{L0} + \gamma P$	[Pa]
τ_{L0}	constant		[Pa]
τ_m	mean shear stress		[Pa]
τ_r	shear stress (Eyring)	$\tau_r = \tau_0$	[Pa]
	(limiting shear stress)	$\tau_r = \tau_L$	[Pa]
$\bar{\tau}$	dimensionless shear stress	$\bar{\tau} = \tau/\tau_r$	-
$\bar{\tau}_c$	characteristic dimensionless shear stress	$\bar{\tau}_c = \bar{S}\bar{\eta}/H_c$	-
ϕ	waviness phaseshift		-
χ	constant		-
ψ	coefficient	$\psi = \tau_L/\tau_0$	-
ω	temperature characteristic shear stress coefficient		-

subscript for θ:

$_h$	high-speed asymptotic solution
$_l$	low-speed asymptotic solution
$_r$	rolling asymptotic solution
$_s$	sliding asymptotic solution

subscript for δT:

$_S$	surface temperature increase
$_l$	lubricant film temperature increase

subscript for μ and σ:

$_R$	rough surface
$_S$	smooth surface

subscript:

$_1$	body number 1
$_2$	body number 2

Chapter 1

Introduction

In many of the objects surrounding us in everyday life, from washing machines to cars, rolling bearings are present to permit rotary motion. They represent some sort of hidden technology, the kind that gets noticed only when it fails. Nevertheless as one of the elements allowing motion to be transmitted they contribute in many cases to a significant part of the power loss of the application. As part of the current drive for energy-saving there is a strong interest in optimizing the frictional behaviour of rolling bearings.

Rolling bearings are based on the very old principle that it requires "less effort to move a body over rollers than to let it slide over the same surface" [39]. A rolling bearing is usually made of one or two rows of balls or rollers between an inner and outer ring one of which is fixed to a shaft and the other to a housing, see Fig. 1.1. A cage may be interposed to control the distance between the rolling elements. The transmission of load takes place in two concentrated contacts on either side of each rolling elements where very high pressures are reached (up to 3 GPa) lubricated with a very thin lubricant film (thickness $\leq 1\mu$m).

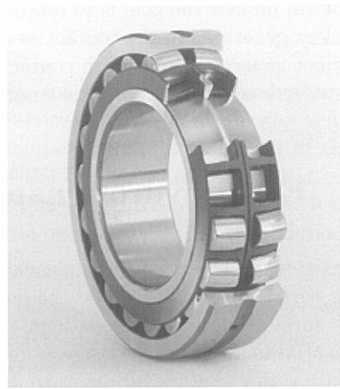

Figure 1.1: Spherical roller bearing.

To prevent failure of the rolling bearing the amount of metallic contact between surface roughness asperities breaking through the film in the contact area has to remain very small i.e. the film thickness of the lubricant film should be larger than the combined roughness of the surfaces. Traditionally this has been achieved by making the surfaces as smooth as possible and in designing the bearings such that thick films would be created. In recent years down-sizing and increasingly severe operating conditions have fostered a new approach in which surface roughness

becomes also a design parameter. The goal then is to design complex surface patterns that enhance rather than hinder lubrication. For both approaches the accurate prediction of the lubricant film thickness is crucial to prevent failure. As a consequence a large number of numerical studies has been performed over the years relating the film thickness to the operating conditions. Design curves have been established to predict the film thickness and more recently the deformation of the roughness in the contact for a wide range of operating conditions.

The topography of the surface roughness is designed first and foremost to enhance lubrication and prevent failure. It will however also have consequences on the level of friction generated in the contacts. In most cases this level should be as low as possible but for certain applications, in spherical roller bearings (SRB) for instance, a difference in the friction generated in the inner ring-roller and outer ring-roller contacts is needed for the optimum operation of the rolling bearing [50]. The differential of friction is created by using different surface texture on each ring. In that case an accurate prediction of the effects of roughness on friction is crucial. However by contrast with the state of the art in film thickness prediction no systematic approach has been applied to the numerical simulation of the friction generated in the lubricant film. There are no general predictive formulas for the coefficient of friction in smooth contacts and the consequences of the introduction of roughness patterns on friction are almost completely ignored.

The objective of this thesis is to apply the systematic approach used in film thickness simulations to friction prediction. Based on the currently existing numerical tools and rheological models the goal is to establish general engineering formulas giving the friction coefficient generated in the contact as a function of the operating conditions. The friction coefficient generated in smooth contacts needs to be considered first to allow an analysis of the effects of roughness on the smooth level of friction.

1.1 Elastohydrodynamic lubrication

The existence of a very thin lubricant film in the concentrated contact between two rolling surfaces is explained by the combination of two effects: the elastic deformation of the surfaces under the very high pressures occurring in the contact and the nearly exponential increase of the viscosity of the lubricant with pressure. The first effect helps to create a gap to allow lubricant to pass through whereas the second prevents lubricant to flow around the contact by "freezing" by an increase of viscosity a small part just in front of the contact. This part is then transported by hydrodynamic action in the contact area. This lubrication regime is called elastohydrodynamic lubrication (EHL).

Fig. 1.2(a) shows a schematic cross-section of a contact between a ball and a flat surface. Assuming that all the elastic deformation takes place in the ball, the part of the ball close to the plane surface is flattened leading to an almost constant lubricant film thickness in the contact. Due to hydrodynamic effects a constriction appears at the outlet of the contact. The pressure distribution in the contact exhibits a semi ellipsoidal shape

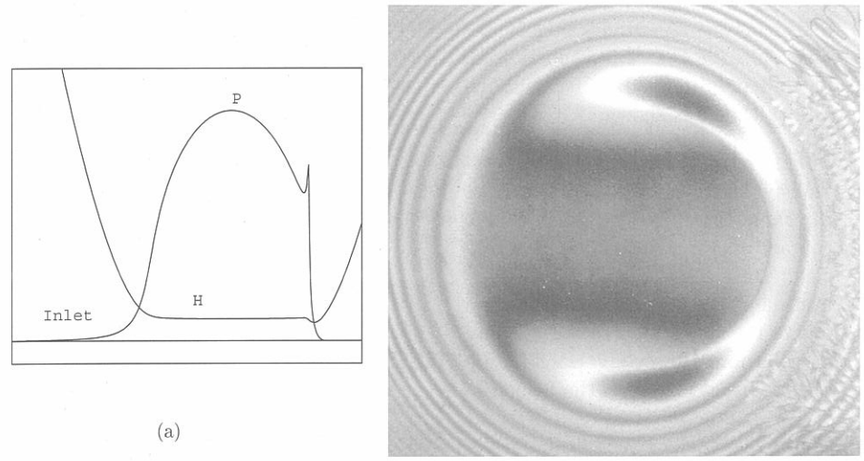

(a) (b)

Figure 1.2: (a): Schematic representation of a cross-section in the running direction of a point contact. P denotes the pressure profile whereas H indicates the film thickness. (b): Film thickness map of a point contact obtained using optical interferometry. In both cases the inlet is on the left.

with a pressure spike just before the location of the constriction and a gradual pressure buildup in the inlet region of the contact. With increasing load or decreasing velocities the pressure profile tends towards the perfectly semi-ellipsoidal distribution of the dry contact situation (Hertzian contact). A picture of the film thickness in circular contact obtained using optical interferometry is shown in Fig. 1.2(b) (courtesy of M. Kaneta). One recognizes the central flat plateau ending in the outlet side by the constriction with a typical horseshoe shape.

The first numerical solution of pressure and film thickness in an EHL contact was obtained in 1951 by Petrusevitch [63] for a line contact. The next landmark was the paper of Dowson and Higginson in 1959 [22] reporting extensive numerical calculations of the film thickness for line contacts followed in 1976-77 by a series of publications of Hamrock and Dowson for the point contact problem [37, 38]. The general predictive formula derived by the authors from their numerical results is still used today. In 1987 Lubrecht [55] followed by Venner [71] in 1991 improved considerably the efficiency of numerical solvers by introducing multilevel techniques. Thanks to these techniques the analysis of transient surface roughness effects came within reach. The progress on the experimental side has also been substantial in the last decades. The first images of film thickness in an EHL contact were obtained in 1963 by Gohar and Cameron [32] using interferometry techniques. Since then the development of spacer layer techniques has allowed the measurements of film thickness only a few nanometers thick [19].

The agreement between numerical and experimental results is quite remarkable, see Fig. 1.3 where a comparison of measured and calculated film thickness is shown.

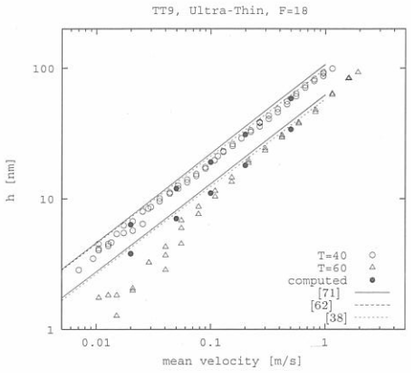

Figure 1.3: Comparison of calculated and measured film thickness as a function of speed for two temperatures $T = 40$ and 60^oC. Prediction of various film thickness formulas are also shown. Measurements performed by C.H. Venner with the spacer layer technique at Imperial College, London.

In almost all of the studies cited previously the contacting bodies have the same velocities. In that case the contact operates with almost no friction. Only a very small pure-rolling friction coefficient can be measured due to the asymmetry of the pressure distribution. However as soon as slip is introduced i.e. when the velocities of the contacting bodies differ, the friction coefficient increases quickly to reach a value of $0.03 \leq \mu \leq 0.12$. In EHL contacts the slip difference is mainly accommodated in the lubricant film. Recalling both the very high viscosity of the lubricant in the contact and the thinness of the film, the shear rates imposed on the lubricant are very large. At these shear rate values the lubricant behaves in a non-Newtonian way.

The evidence of non-Newtonian behaviour is provided by the shape of measured traction curves where the friction coefficient is measured as a function of slip. A schematic example of such a traction curve is shown in Fig. 1.4. This figure shows that the friction coefficient increases linearly with increasing slip, i.e. behaves as a Newtonian fluid, for a small range of slip values only. Quickly the traction curve bends off, stays on a constant level and even decreases with increasing slip. This nonlinear behaviour cannot be entirely explained by thermal effects as postulated by Crook in 1961 [21] but requires the existence of some sort of non-Newtonian behaviour.

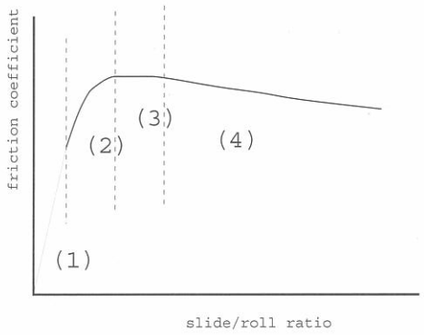

Figure 1.4: Schematic traction curve.

Four regions can be distinguished in a typical traction curve: (1) an initial linear increase of the friction coefficient with slip followed by (2) a leveling of the traction curve at higher slip rates. (3) At even higher slip rates the value of the friction coefficient appears

to become independent of the slip. (4) Finally the friction coefficient decreases with slip. The general opinion is now that thermal effects become significant mainly in the fourth region. To explain and predict the second and third regions of the traction curve accurately the non-Newtonian behaviour of the lubricant under EHL conditions has to be characterized and implemented in numerical solvers.

The next section gives an overview of the history of modeling non-Newtonian effects in EHL contacts. Because this thesis considers friction simulation the emphasis lies on the models implemented in numerical solvers more than on the experimental characterization of non-Newtonian behaviour.

1.2 Modeling non-Newtonian behaviour

By the mid 1970s there was a general consensus that an explanation of the non-linear shape of measured traction curves based entirely on thermal effects was not valid. Several papers had already described the response of the lubricant as nonlinear, notably that of Trachman and Cheng [69] in 1972 and of Hirst and Moore [40] in 1974, when Johnson and Tevaarwerk published their classical paper in 1977 [48]. This last paper presented a nonlinear Maxwell constitutive equation in which the nonlinear viscous response of the lubricant was described using Eyring theoretical sinh law. Note that a significant amount of friction is generated in EHL contacts such that the shear stresses are usually large enough for the non-linear viscous flow to dominate the strain rate in the lubricant film. Consequently, in the rest of this work elastic effects are neglected. The rheological behaviour of the lubricant is based only on viscous effects. The viscous component of the model of Johnson and Tevaarwerk relating the shear rate $\dot{\gamma}$ to the shear stress is given by:

$$\dot{\gamma} = \frac{\tau_0}{\eta} \sinh\left(\tau_e/\tau_0\right) \tag{1.1}$$

with τ_e an equivalent shear stress. The characteristic parameter in this model is the Eyring stress τ_0 which represents the value of the shear stress beyond which the response of the fluid to shear becomes nonlinear. Eyring's activation theory gives only an order of magnitude for τ_0: $\tau_0 \sim 4$ MPa [49]. Johnson and Tevaarwerk showed that their model could describe experimental traction curves measured on a two-disk machine. However a major drawback of the approach with respect to friction prediction is the fact that the values of the parameters of the model need to be curve-fitted from measured traction curves.

Two years later a radically different approach was presented by Bair and Winer in two companion papers [3, 4]. Their analysis of non-Newtonian behaviour of lubricants at high shear rate was based on primary laboratory experiments using constant pressure stress strain apparatuses and high-shear viscometers. They showed that the lubricants exhibited a limiting shear stress and proposed the following relation between shear rate and shear

stress:

$$\dot{\gamma} = -\frac{\tau_L}{\eta} \ln\left(1 - \frac{\tau}{\tau_L}\right) \tag{1.2}$$

The characteristic parameter of the model is the limiting shear stress τ_L. It was shown to vary approximately linearly with pressure $\tau_L = \tau_{L0} + \gamma p$ where τ_{L0} is small (O(1)MPa) and $0.03 \leq \gamma \leq 0.12$.

These two models have coexisted until today although they are very different both in the constitutive equation and in the approach taken. Most of the corpus of numerical studies of non-Newtonian effects in EHL contacts up to this date are either based on the Eyring model or on some variation of Eq. 1.2. Only a small number of studies have considered another type of model. Among them Jacobson and Hamrock presented [46] a model in 1984 in which limiting shear stress behaviour was obtained by allowing slip to occur at the surfaces. Recently Ehret et al. [24] have also implemented slip-at-the-wall boundary conditions in a non-Newtonian EHL analysis.

In order to predict friction, the shear stress distribution has to be solved and integrated numerically using the previously described rheological models. The complexity of the numerical studies has increased over the years. The first analyses of Johnson and Tevaarwerk [48] and Bair and Winer [4] and later of Gecim and Winer [30] assumed simplified pressure and film thickness profiles or a Grubin-like inlet analysis and concentrated on calculating the shear stresses and resulting friction coefficient. The first full numerical solution for a line contact incorporating non-Newtonian effects was presented in 1984 by Jacobson and Hamrock [46] for a slip-at-the-wall limiting shear stress model. It was followed in 1987 by Conry et al. [20] and in 1991 by Sui and Sadeghi [68] for the Eyring model. Later on several variations of the limiting shear stress model were implemented in line contact studies: the linear model introduced by Wang et al. [76] and later used by Iivonen and Hamrock [45]; the circular model by Lee and Hamrock [53], also used by Hsiao and Hamrock [43, 44]. A useful generalization of the limiting shear stress models is given by Elsharkawy and Hamrock

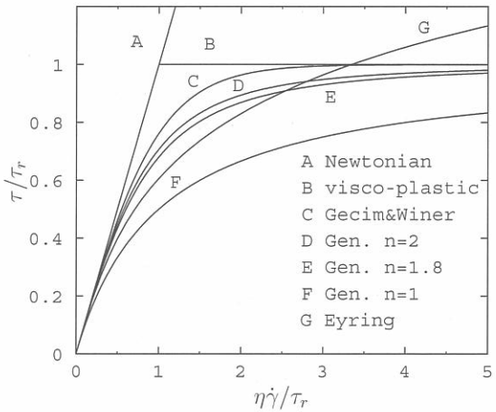

Figure 1.5: Rheological models. Limiting shear stress model: $\tau_r = \tau_L$, Eyring model $\tau_r = \tau_0 = \tau_L/3$.

[27]:

$$\dot{\gamma} = \frac{\tau}{\eta}\left(1 - \left(\frac{\tau}{\tau_L}\right)^n\right)^{-1/n} \tag{1.3}$$

where the linear model corresponds to $n = 1$ and the circular model to $n = 2$. A good approximation of Eq. 1.2 is given by $n = 1.8$ whereas Gecim and Winer model [30] can be approximated by $n = 2.8$. Fig. 1.5 illustrates the different rheological models mentioned. It shows the rheological function giving the shear stress as a function of the shear rate for the different models.

The analysis has been extended to point and elliptic contacts by Kim and Sadeghi [51], Holt et al. [42], Ehret et al. [24] for the Eyring model and Ehret et al. [24] and Sharif et al. [67] for limiting shear stress models. In general for this configuration the implementation of non-Newtonian effects in a numerical solver is not straightforward. Except for [51] and [67] some approximation of the rheological function is used in the other works.

As can be seen in the previous paragraphs, the number of full numerical studies of non-Newtonian EHL contacts is small. Moreover in most cases these studies focus on the effect of the non-Newtonian behaviour on the film thickness and pressure profiles rather than on friction prediction. When friction results are presented either the range of variation of the operating condition is small and no general prediction formula is given, with the exception of Jacobson and Hamrock [46], or the objective is to compare with experimental results in specific cases.

In recent years it has become increasingly clear that to model accurately non-Newtonian behaviour in EHL contacts not only the constitutive equation had to be correctly modeled but also the other lubricant characteristics such as its piezo-viscosity. Since 1984 one group of researchers has introduced viscosity pressure relations taken from high-pressure physics to describe the viscosity pressure data they obtained with falling-body viscometers and high-pressure viscometers [78, 6]. They have shown that the shape of the pressure viscosity curve could have an influence on the shape of the calculated traction curves and therefore on the kind of rheological model appropriate to describe non-Newtonian effects in EHL contacts [7, 8]. Similarly they have shown that implementing shear thinning effects could play a big role in the position and shape of the nonlinear region of the predicted traction curves [9]. Generally speaking they have tried to introduce concepts and approaches commonly used in rheology to elastohydrodynamic lubrication [11]. At this point, however, this approach is only starting to be implemented in full numerical analyses [52].

Summarizing, the state-of-the-art in modeling of non-Newtonian behaviour in EHL contacts is composed of a few full numerical studies of elliptic contacts based on rheological models described in their principle at the end of the 1970s. The results for line contacts are more numerous but all in all no wide-ranging systematic analysis of the friction coefficient in EHL contacts has been reported yet. The divide existing at the time between the two approaches used for describing non-Newtonian effects has not been reduced. On the contrary recent attempts to broaden the field of rheological studies in EHL contacts

to piezo-viscous effects and shear thinning has only increased it.

1.3 Roughness

In elastohydrodynamic lubrication the rolling surfaces are generally fully separated by a lubricant film. However, as a result of down-sizing and increasingly severe operating conditions the film thickness in contacts in actual applications has decreased to a level where the effects of surface roughness on the operation can no longer be neglected. This does not necessarily imply that in response the surfaces have to be made smoother during the manufacturing process. Alternatively, surface roughness can be designed in such a way that it mainly consists of components that will deform elastically in the contact and thereby prevent film break-through. This method is generally preferred considering the cost of the surface finishing operations required to smooth the surfaces. To make this approach successful requires a detailed understanding of the way surface roughness deforms inside a contact. As measuring this deformation in-situ is only possible in model contacts (between glass disk and steel ball) the main way to acquire such knowledge has been by means of numerical simulations. At present, as a result of the improvements in computational capability, numerical simulations can be performed using an explicit description of the roughness.

One way to study the influence of roughness is then to consider measured rough profiles on one or both surfaces. The film thickness and pressure distributions are then calculated as a function of time as the roughness goes through the contact [1, 77]. This approach seems to be the closest approximation to "reality" but there are several drawbacks: a very large number of discretization points is needed to represent the roughness profile and to obtain an accurate estimate of the effect of these components on the pressure and film thickness. Even with efficient algorithms the computing time for the transient calculation will quickly be very large. Secondly, because of the complexity of most roughness distributions it is very difficult to draw general conclusions let alone derive formulas that can be of practical use in engineering design.

An alternative approach consists of a description of surface roughness in terms of its harmonic components. The effect of each component can be studied individually. The influence of complex roughness distribution can then be understood by superposition of the individual components, see [72, 57] and references therein. This approach has proved very efficient and has lead to simple engineering formulas for the prediction of roughness deformation in EHL contacts.

The emphasis in the numerical studies has been the prediction of the roughness deformation i.e. the film thickness and the pressure fluctuations, and most studies were restricted to the case of Newtonian lubricant behaviour. By contrast very little work has been done regarding the prediction of the effects of roughness on friction. One of the few publications in which the friction generation in rough EHL contacts is studied is the paper of Xu and Sadeghi [77] in which the effect of a real roughness distributions on friction is

considered for a thermal Newtonian contact. In this paper a relation is inferred between the statistical parameters characterizing the roughness distribution and the values of the maximum friction coefficient, temperature, and pressure. The practical value of this relation is questionable considering the difficulty of adequately characterizing a complex roughness distribution with statistical parameters. Moreover non-Newtonian effects are not taken into account.

1.4 Outline

Since the mid 1970s it has become clear that the frictional behaviour observed in EHL contacts is mainly caused by a non-Newtonian response of the lubricant to shear and only at high shear rates also by thermal effects. The number of numerical studies in which frictional behaviour is investigated is very small compared to the number of numerical studies in which emphasis is on the prediction of the film thickness in smooth and rough EHL contacts. Also the nature of the studies on friction is very different. This may be attributed to the fact that friction can relatively easily be measured whereas film thickness measurements are only possible in model contacts. In any case this has led to the situation where the level of knowledge regarding the prediction of film thickness is much higher than that regarding the prediction of friction. So far no systematic theoretical study of friction generation has been conducted.

Yet, the basis on which such a systematic analysis could be built exists. From a numerical point of view stable and efficient solvers based on multilevel techniques are available for the Newtonian problem. From a rheological point of view several models have already been defined and implemented describing a large range of lubricant response. For elliptic contacts specifically the incorporation of non-Newtonian effects in a full numerical analysis has been reported for the Eyring model and can be used in that case without modifications. However, for limiting shear stress models some work will have to be done to increase the efficiency and accuracy of the methods published until now. Finally, with respect to the influence of roughness, an approach based on the study of harmonic components has proved very useful for film thickness prediction and can also be used for friction.

The objective of this thesis is therefore to start a systematic study of friction generation in EHL contacts by combining the existing numerical techniques, rheological models and approaches for considering roughness effects. The equations describing the non-Newtonian EHL problem and a description of the numerical methods used in the numerical solver are described in Chapt. 2 and Chapt. 3 respectively. The numerical solver is then applied extensively to the isothermal prediction of the friction coefficient for the rolling sliding contacts in Chapt. 4. A simplified analysis giving a correction of the friction coefficient due to thermal effects is described in Chapt. 5. Finally the consequences of introducing roughness on the level of the friction obtained for the smooth contacts is studied in Chapt. 6.

Chapter 2

Theory

The introduction of non-Newtonian lubricant behaviour in EHL contact models involves the derivation of a modified Reynolds equation to describe the flow of lubricant. Non-Newtonian effects are usually taken into account by means of effective viscosities so that the flow equation keeps the same form as the Reynolds equation for Newtonian lubricants. The complexity of the expressions giving the effective viscosities depends on the rheological model considered and the number of assumptions made regarding the distribution of the shear stresses in the film. For line contacts the expressions are simple. For elliptic contacts, the expressions are in general complex but simplified expressions can be obtained by making assumptions on the form of the rheological function [42] or by using a perturbational approach [24].

In this chapter the derivation of a non-Newtonian Reynolds equation for elliptic contacts is given based on a perturbational approach. It results in new and more accurate expressions for the effective viscosities for limiting shear stress models. For the Eyring model the expressions given by [24] are used. Subsequently, the film thickness, force balance, and friction coefficient equations are presented. For completeness the corresponding set of equations for the line contact problem is also given. The Hertzian dry contact parameters are used to obtain the dimensionless equations. The equations describing the dependence of the lubricant viscosity and density on pressure are listed next. The chapter ends with the derivation of a set of independent parameters characterizing the contact.

2.1 Rheological models

The different types of rheological response of a lubricant subjected to shear in a rolling/sliding EHL contact have already been described in Chapt. 1. The mathematical formulation of the models considered in this work is presented here. Of interest are the rheological function $f(\tau/\tau_r)$ which relates the shear rate to the shear stress and a characteristic shear stress τ_r. The characteristic shear stress for the Eyring model is named the Eyring stress

and denoted $\tau_r = \tau_0$. It represents the shear stress beyond which the fluid starts to behave as a non-Newtonian fluid. In practice its value is obtained from the slope of measured traction curves [59]. For the limiting shear stress models the characteristic shear stress is the limiting shear stress $\tau_r = \tau_L$ where τ_L is taken to depend linearly on pressure: $\tau_L(p) = \tau_{L0} + \gamma p$ with τ_{L0} small (10^5 Pa in this work) and $0.03 \leq \gamma \leq 0.15$. The limiting shear stress proportionality coefficient γ can be obtained independently of traction tests using a constant pressure stress-strain apparatus [3, 5], a high-pressure chamber [41] or a falling ball apparatus [47] (see also [64, 65]).

The rheological function $f(\tau/\tau_r)$ relating the shear rate $\dot{\gamma}$ to the shear stress τ is defined by:

$$\eta\dot{\gamma} = \tau f(\tau/\tau_r) \tag{2.1}$$

Eyring	$f(\tau/\tau_0) = \tau_0/\tau \sinh(\tau/\tau_0)$
General model Limiting shear stress	$f(\tau/\tau_L) = (1 - (\tau/\tau_L)^n)^{-1/n}$
Gecim & Winer	$f(\tau/\tau_L) = \tau_L/\tau \tanh^{-1}(\tau/\tau_L)$

Table 2.1: Rheological functions.

For the models considered: the Eyring model, the general limiting shear stress model [27] with $n = 1$ (linear model [45]), $n = 1.8$ and $n = 2$ (circular model [53]) and Gecim and Winer's model [30], $f(\tau/\tau_r)$ is given in Table 2.1. Its behaviour as a function of (τ/τ_r) is shown in Fig. 2.1. The main difference between the limiting shear stress models is the rate at which they approach the limiting shear stress τ_L.

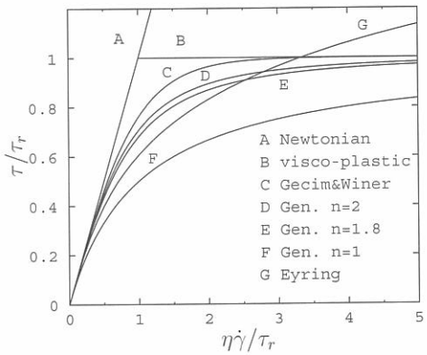

Figure 2.1: Rheological models. Limiting shear stress model: $\tau_r = \tau_L$, Eyring model $\tau_r = \tau_0 = \tau_L/3$.

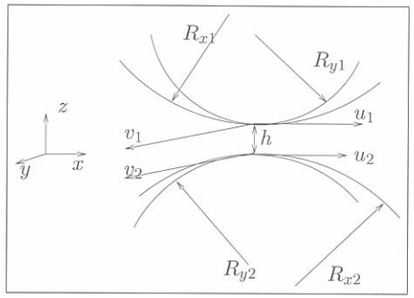

Figure 2.2: Geometry of the gap.

2.2 Elliptic contact

2.2.1 Non-Newtonian Reynolds equation

In this section, an equation describing the flow of a non-Newtonian lubricant through a narrow gap of known geometry is derived. See Fig. 2.2 for a description of the geometry of the gap. If the lubricant behaves as a Newtonian fluid the equation reduces to the traditional Reynolds equation.

The following assumptions are made about the contact and the flow:

1. The forces due to inertia are neglected.
2. The thickness of the lubricant film is small compared to the characteristic dimensions of the contact area.
3. In addition, because in this work sliding occurs only along the running direction (x-direction) the shear stresses in both direction are taken to be only partially coupled, i.e. the equivalent shear stress equals the shear stress in the main direction of shear $\tau_e = \sqrt{\tau_x^2 + \tau_y^2} \sim \tau_x$ and the mean shear stress in the y-direction is negligible. Then the shear stresses are given by:

$$\tau_x = \tau_m + z\frac{\partial p}{\partial x}, \qquad \tau_y = z\frac{\partial p}{\partial y} \tag{2.2}$$

with τ_m the mean shear stress in the running direction. Starting from the shear rate shear-stress relations the flow equation relating the pressure to the film thickness is derived for both the Eyring and the limiting shear stress models. The shear stress shear-rate relations read:

$$\eta\frac{\partial u}{\partial z} = \tau_x f(\tau_x), \qquad \eta\frac{\partial v}{\partial z} = \tau_y f(\tau_x) \tag{2.3}$$

Substituting Eq. 2.2 in Eq. 2.3 gives:

$$\eta\frac{\partial u}{\partial z} = (\tau_m + z\frac{\partial p}{\partial x})f(\tau_m + z\frac{\partial p}{\partial x}), \qquad \eta\frac{\partial v}{\partial z} = z\frac{\partial p}{\partial y}f(\tau_m + z\frac{\partial p}{\partial x}) \tag{2.4}$$

For a Newtonian lubricant Eq. 2.4 can be integrated twice with respect to z in closed form. The Reynolds equation is obtained after substitution of the resulting equation in the integrated equation of continuity. The introduction of non-Newtonian effects by means of the rheological function $f(\tau)$ makes the integration in closed form impossible. The alternative is either to approximate the rheological function at this point in such a way that it becomes possible to integrate Eq. 2.3 in closed form or to keep the integrals and try to find a way to evaluate them simply at a later stage. The first method has been used by Ehret et al. [24] and by Holt et al. [42]. In [24] a perturbational method based on a first-order Taylor expansion of $f(\tau_m + z(\partial p/\partial x)$ with respect to z is used leading to:

$$f(\tau_m + z\frac{\partial p}{\partial x}) = f(\tau_m) + z\frac{\partial p}{\partial x}f'(\tau_m) \tag{2.5}$$

The resulting shear stress-shear rate equation can be integrated twice with respect to z in closed form to obtain a modified Reynolds equation just as in the Newtonian case. Greenwood [34] has shown that for the Eyring model, the loss of accuracy is negligible.

For the limiting shear stress model however, because of the asymptotic behaviour of the rheological function, using a first-order approximation at this stage leads to large errors. The modified Reynolds equation is therefore derived in a different way for the Eyring and the limiting shear stress models. For the Eyring model the approach described in [24] is used whereas for the limiting shear stress models the integrals are kept.

Eq. 2.4 and Eq. 2.5 are integrated once with respect to z to obtain the velocity distribution across the film. No-slip boundary conditions are used: $u = u_1,\ v = 0$ at $z = -h/2$ and $u = u_2,\ v = 0$ at $z = h/2$.

Limiting shear stress

$$\eta u(z) = \eta u_1 + \tau_m \int_{-h/2}^{z} f(\tau_x)\,dz' + \frac{\partial p}{\partial x}\int_{-h/2}^{z} f(\tau_x) z' dz'$$

$$\eta v(z) = \frac{\partial p}{\partial y}\int_{-h/2}^{z} f(\tau_x) z'\,dz' \tag{2.6}$$

Eyring

$$\eta u(z) = \frac{\eta(u_2 - u_1)}{2} + (z - \frac{h}{2})\tau_m f(\tau_m) + \frac{z^2}{2}(f(\tau_m) + \tau_m f'(\tau_m))\frac{\partial p}{\partial x}$$

$$\eta v(z) = \frac{z^2}{2}\frac{\partial p}{\partial y} \tag{2.7}$$

At the same time an equation for the mean shear stress is obtained:

Limiting shear stress

$$\tau_m = \frac{\eta(u_2 - u_1) - \frac{\partial p}{\partial x} I_2}{I_1} \tag{2.8}$$

Eyring

$$\tau_m f(\tau_m/\tau_r) = \frac{\eta(u_2 - u_1)}{h} \tag{2.9}$$

where I_1 and I_2 are defined below. Eqs. 2.6 and 2.7 are integrated once more with respect to z to obtain the volume flow rates. Using mass conservation finally results in the modified Reynolds equation:

Limiting shear stress

$$\frac{\partial}{\partial x}\left[\left(\frac{I_4 I_1}{I_2} - I_3\right)\frac{\rho}{\eta}\frac{\partial p}{\partial x}\right] - \frac{\partial}{\partial y}\left[I_4\frac{\rho}{\eta}\frac{\partial p}{\partial y}\right] - \frac{\partial}{\partial x}\left[\left(u_1 h + (u_2 - u_1)\frac{I_3}{I_1}\right)\rho\right] = 0 \tag{2.10}$$

Eyring

$$\frac{\partial}{\partial x}\left[(f(\tau_m) + \tau_m f'(\tau_m))\frac{\rho h^3}{12\eta}\frac{\partial p}{\partial x}\right] + \frac{\partial}{\partial y}\left[f(\tau_m)\frac{\rho h^3}{12\eta}\frac{\partial p}{\partial y}\right] - \frac{\partial}{\partial x}\left[\frac{u_2 + u_1}{2} h\rho\right] = 0 \tag{2.11}$$

with:

$$I_1 = \int_{-h/2}^{h/2} f(\tau_x)\,dz, \qquad I_2 = \int_{-h/2}^{h/2} f(\tau_x) z\,dz$$

$$I_3 = \int_{-h/2}^{h/2}\int_{-h/2}^{z} f(\tau_x)\,dz'dz, \qquad I_4 = \int_{-h/2}^{h/2}\int_{-h/2}^{z} f(\tau_x) z'\,dz'dz \tag{2.12}$$

The modified Reynolds equation is defined on the domain $x_a \le x \le x_b,\ y_a \le y \le y_b$. On the boundaries of the domain $p = 0$ and a complementarity cavitation condition $p \ge 0$ is imposed everywhere. Compared to Eq. 2.11 obtained for the Eyring model, Eq. 2.10 still contains integrals that have to be evaluated. This adds to the complexity of the problem and makes the numerical solution of the flow equation rather cumbersome.

At this point however the rheological function $f(\tau)$ for the limiting shear stress models can be replaced by a first-order Taylor expansion with respect to z with little loss of accuracy. Indeed by using the first order Taylor expansion once that the Reynolds equation has been completely derived rather than in the first stages of its derivation, the loss of significant terms in the equation can be prevented. In that case the integrals I_1 to I_4 can all be

evaluated straightforwardly yielding:

$$
\begin{aligned}
I_1 &= hf(\tau_m) \\
I_2 &= \frac{h^3}{12}\frac{\partial p}{\partial x}f'(\tau_m) \\
I_3 &= \frac{h^2}{2}f(\tau_m) - \frac{h^3}{12}\frac{\partial p}{\partial x}f'(\tau_m) \\
I_4 &= \frac{-h^3}{12}f(\tau_m) + \frac{h^4}{24}\frac{\partial p}{\partial x}f'(\tau_m)
\end{aligned} \tag{2.13}
$$

Substitution of Eq. 2.13 in the modified Reynolds equation, Eq. 2.10, gives:

$$
\frac{\partial}{\partial x}\left[f(\tau_m)\frac{\rho h^3}{12\eta}\frac{\partial p}{\partial x}\right] + \frac{\partial}{\partial y}\left[\left(f(\tau_m) - \frac{h}{2}\frac{\partial p}{\partial x}f'(\tau_m)\right)\frac{\rho h^3}{12\eta}\frac{\partial p}{\partial y}\right] - \frac{\partial}{\partial x}\left[\left(\frac{u_2+u_1}{2} - (u_2-u_1)\frac{h}{12}\frac{\partial p}{\partial x}\frac{f'(\tau_m)}{f(\tau_m)}\right)\rho h\right] = 0 \tag{2.14}
$$

The influence of non-Newtonian effects can now be represented by effective viscosities giving the following Reynolds equation for the two models:

Limiting shear stress

$$
\frac{\partial}{\partial x}\left[\frac{\rho h^3}{12\eta_x}\frac{\partial p}{\partial x}\right] + \frac{\partial}{\partial y}\left[\frac{\rho h^3}{12\eta_y}\frac{\partial p}{\partial y}\right] - \frac{\partial}{\partial x}\left[\tilde{u}_m \rho h\right] = 0 \tag{2.15}
$$

Eyring

$$
\frac{\partial}{\partial x}\left[\frac{\rho h^3}{12\eta_x}\frac{\partial p}{\partial x}\right] + \frac{\partial}{\partial y}\left[\frac{\rho h^3}{12\eta_y}\frac{\partial p}{\partial y}\right] + \frac{\partial}{\partial x}\left[u_m \rho h\right] = 0
$$

where $\tilde{u}_m = u_m - (u_2 - u_1)/12(\partial p/\partial x)f'(\tau_m)/f(\tau_m)$. The effective viscosities can be obtained from flexible and easy to evaluate relations.

Limiting shear stress

$$
\begin{aligned}
\frac{\eta}{\eta_x} &= f(\tau_m) \\
\frac{\eta}{\eta_y} &= f(\tau_m) - \frac{h}{2}\frac{\partial p}{\partial x}f'(\tau_m)
\end{aligned} \tag{2.16}
$$

Eyring

$$
\begin{aligned}
\frac{\eta}{\eta_x} &= f(\tau_m) + \tau_m f'(\tau_m) \\
\frac{\eta}{\eta_y} &= f(\tau_m)
\end{aligned} \tag{2.17}
$$

In the case of the limiting shear stress model a correction to the wedge term also appears giving an explicit dependence of the Reynolds equation on the slip velocity. Both models depend on the value of the mean shear stress given in both cases by:

$$
\tau_m f(\tau_m/\tau_r) = \frac{\eta(u_2 - u_1)}{h} \tag{2.18}
$$

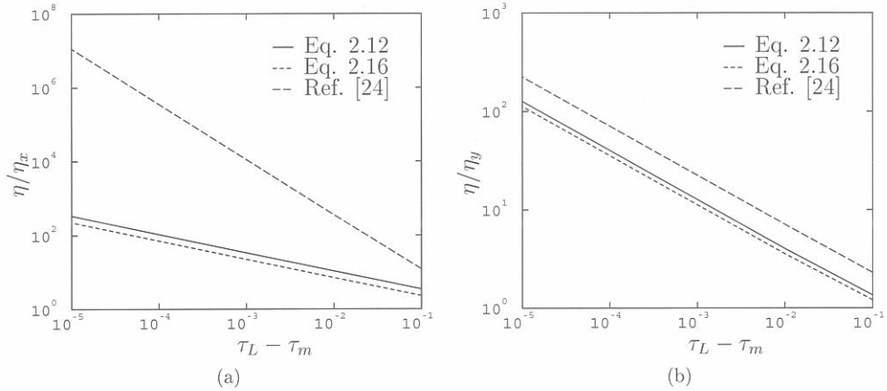

Figure 2.3: Comparison between η/η_x(a) and η/η_y(b) obtained using an analytical integration of Eq. 2.12 for the calculation of η_x and η_y given in Eq. 2.10, Eq. 2.16 and the relation given in [24]. $n = 2$, $(h/2)(\partial p/\partial x) = \tau_L - \tau_m$.

To check the accuracy of Eq. 2.16 η/η_x and η/η_y following from this equation are compared with the exact analytic solution in the particular case of $n = 2$ for which the integrals of Eq. 2.12 can be evaluated in closed form. In order to give an upper bound for the error $(h/2)(\partial p/\partial x)$ is taken at its maximum value, $\tau_L - \tau_m$. The result can be seen in Fig. 2.3 in which the expression obtained with the perturbational method of [24] (Eq. 2.17) has also been plotted. Eq 2.16 leads to a slight underestimation of the effective viscosities and therefore of the non-Newtonian effects whereas Eq. 2.17 results in a very large overestimation.

Summarizing, by applying the perturbation approach at the end of the derivation of the modified Reynolds equation rather than at the beginning, the simplicity and flexibility shown in [24] is preserved but a much more accurate approximation of the effective viscosities is obtained.

2.2.2 Film thickness equation

The contact dimensions are very small compared to the dimensions of the bodies in contact such that their undeformed geometries can be approximated by parabolas, see Fig. 2.2. The gap $h(x, y)$ is obtained by adding the elastic deformation due to a pressure distribution $p(x, y)$ to the undeformed geometry described by parabolas. The mutual

approach δ represents the distance by which both bodies come closer to each other.

$$h(x,y) = -\delta + \frac{x^2}{2R_x} + \frac{y^2}{2R_y} + \frac{2}{\pi E'} \iint_S \frac{p(x',y')\,dx'\,dy'}{\sqrt{(x-x')^2 + (y-y')^2}} \tag{2.19}$$

2.2.3 Force balance equation

For steady state conditions the equation of motion reduces to:

$$\iint_S p(x,y)\,dx\,dy = f \tag{2.20}$$

The value of the mutual approach δ in the film thickness equation must be found such that the force balance equation is always satisfied.

2.2.4 Friction coefficient

The friction coefficient is calculated in the middle of the film by integrating τ_m over the computational domain:

$$\mu = \frac{\iint_S \tau_m dx\,dy}{\iint_S p\,dx\,dy} \tag{2.21}$$

2.2.5 Dimensionless equations

Eqs. 2.15 to 2.21 are made dimensionless using the Hertzian dry contact parameters:

$$\begin{aligned} X &= x/a, & Y &= y/b, \\ H &= h/c, & \Delta &= \delta/c \\ P &= p/p_H, & \bar{\tau}_m &= \tau_m/\tau_r \end{aligned}$$

with:

$$a = \left(\frac{3fR}{E'}\right)^{1/3} \left(\frac{2\kappa\mathcal{E}}{\pi}\right)^{1/3}, \qquad b = a/\kappa,$$
$$c = \frac{a^2}{2R}\frac{\mathcal{K}}{\mathcal{E}}, \qquad p_H = \frac{3f}{2\pi ab}, \qquad R = \left(R_x^{-1} + R_y^{-1}\right)^{-1}$$

The ellipticity ratio κ depends uniquely on R_x/R_y:

$$\frac{R_x}{R_y} = \kappa^2 \frac{\mathcal{K} - \mathcal{E}}{\mathcal{E} - \kappa^2\mathcal{K}} \tag{2.22}$$

where $\mathcal{K} \equiv \mathcal{K}(1-\kappa^2)$ and $\mathcal{E} \equiv \mathcal{E}(1-\kappa^2)$ are the complete elliptic integral of the first and second kind respectively, see [75].

Eqs. 2.15 to 2.21 can now be written in dimensionless form.

2.2.5.1 Modified Reynolds equation

The dimensionless modified Reynolds equation for the elliptic contact can be written as:

Limiting shear stress

$$\frac{\partial}{\partial X}\left[\frac{\bar{\rho}H^3}{\lambda\bar{\eta}_X}\frac{\partial P}{\partial X}\right] + \frac{\partial}{\partial Y}\left[\frac{\bar{\rho}H^3}{\lambda\bar{\eta}_Y}\frac{\partial P}{\partial Y}\right] - \frac{\partial}{\partial X}\left[\left(1 - \frac{S}{6}N_2\frac{\partial P}{\partial X}\frac{f'(\bar{\tau}_m)}{f(\bar{\tau}_m)}\right)\bar{\rho}H\right] = 0 \tag{2.23}$$

Eyring

$$\frac{\partial}{\partial X}\left[\frac{\bar{\rho}H^3}{\lambda\bar{\eta}_X}\frac{\partial P}{\partial X}\right] + \frac{\partial}{\partial Y}\left[\frac{\bar{\rho}H^3}{\lambda\bar{\eta}_Y}\frac{\partial P}{\partial Y}\right] - \frac{\partial}{\partial X}\left[\bar{\rho}H\right] = 0 \tag{2.24}$$

with $\lambda = (6\eta_0 u_s a)/(c^2 p_H)$. On the boundary of the domain $X_a \le X \le X_b$, $Y_a \le Y \le Y_b$ $P = 0$ and a complementarity cavitation condition $P \ge 0$ is imposed everywhere. The dimensionless mean shear stress $\bar{\tau}_m$ is given by the same relation in both cases:

$$\bar{\tau}_m f(\bar{\tau}_m) = N_1 \frac{\bar{\eta}S}{H} \tag{2.25}$$

where:

$$N_1 = \frac{\lambda p_H^2 \mathcal{K}}{6E'\tau_r}, \qquad N_2 = \frac{2p_H^2\mathcal{K}}{E'\tau_r} \tag{2.26}$$

The dimensionless effective viscosities are given by:

Limiting shear stress

$$\begin{aligned} \frac{\bar{\eta}}{\bar{\eta}_X} &= f(\bar{\tau}_m) \\ \frac{\bar{\eta}}{\bar{\eta}_Y} &= f(\bar{\tau}_m) - N_2 H \frac{\partial P}{\partial X} f'(\bar{\tau}_m) \end{aligned} \tag{2.27}$$

Eyring

$$\begin{aligned} \frac{\bar{\eta}}{\bar{\eta}_X} &= f(\bar{\tau}_m) + \bar{\tau}_m f'(\bar{\tau}_m) \\ \frac{\bar{\eta}}{\bar{\eta}_Y} &= f(\bar{\tau}_m) \end{aligned} \tag{2.28}$$

2.2.5.2 Film thickness equation

The dimensionless film thickness equation reads:

$$H(X,Y) = -\Delta + \mathcal{S}X^2 + (1-\mathcal{S})Y^2 + \frac{1}{\pi\mathcal{K}} \iint_S \frac{P(X',Y')\,dX'\,dY'}{\sqrt{\kappa^2(X-X')^2 + (Y-Y')^2}} \tag{2.29}$$

where $\mathcal{S} = \mathcal{S}(\kappa)$ is a shape factor due to the ellipticity of the contact:

$$\mathcal{S}(\kappa) = \frac{\mathcal{E} - \kappa^2\mathcal{K}}{\mathcal{K}(1-\kappa^2)} \tag{2.30}$$

The value of the dimensionless mutual approach Δ is determined by the dimensionless force balance equation.

2.2.5.3 Force balance equation

$$\iint_S P\,dX\,dY = \frac{2\pi}{3} \tag{2.31}$$

2.2.5.4 Friction coefficient

Finally a reduced friction coefficient is defined as:

Limiting shear stress

$$\bar{\mu} = \mu\frac{p_H}{\tau_L(p_H)} = \frac{\iint_S \tau_L(p_H P)\bar{\tau}_m\,dX\,dY}{\tau_L(p_H)\iint_S P\,dX\,dY} \tag{2.32}$$

Eyring

$$\bar{\mu} = \mu\frac{p_H}{\tau_0} = \frac{\iint_S \bar{\tau}_m\,dX\,dY}{\iint_S P\,dX\,dY} \tag{2.33}$$

2.3 Line contact

The present study is mainly about friction in elliptic contacts. However for completeness line contact situations are also studied as they represent the limit case for very wide elliptic contacts $\kappa \ll 1$. The equations describing line contacts are listed below.

2.3.1 Non-Newtonian Reynolds equation

For the Eyring model, the non-Newtonian Reynolds equation has been derived by Conry et al. [20]:

$$\frac{\partial}{\partial x}\left[\frac{\rho h^3}{12\eta_x}\frac{\partial p}{\partial x}\right] - \frac{\partial}{\partial x}[u_m \rho h] = 0 \tag{2.34}$$

on the domain $x_a \le x \le x_b$ with $p(x_a) = p(x_b) = 0$ and a complementarity cavitation condition imposed everywhere $p \ge 0$. The effective viscosity is given by:

$$\eta/\eta_x = -3\frac{\sinh\Sigma - \Sigma\cosh\Sigma}{\Sigma^3}\cosh(\tau_m/\tau_0), \text{ with: } \Sigma = \frac{h}{2\tau_0}\frac{\partial p}{\partial x} \tag{2.35}$$

The mean shear stress follows from:

$$\sinh(\tau_m/\tau_0) = \frac{\eta(u_2-u_1)}{h\tau_0}\frac{\Sigma}{\sinh\Sigma} \tag{2.36}$$

For limiting shear stress models, the non-Newtonian Reynolds equation can be directly deducted from the analysis for the elliptic contacts, see Sect. 2.2, as $\tau_e = \tau_x$. In that case it reads:

$$\frac{\partial}{\partial x}\left[\frac{\rho h^3}{12\eta_x}\frac{\partial p}{\partial x}\right] - \frac{\partial}{\partial x}[\tilde{u}_m \rho h] = 0 \tag{2.37}$$

where the effective viscosity is given by:

$$\eta/\eta_x = f(\tau_m), \qquad \tilde{u}_m = u_m - \frac{u_2-u_1}{12}\frac{\partial p}{\partial x}\frac{f'(\tau_m)}{f(\tau_m)} \tag{2.38}$$

The mean shear stress follows from:

$$\tau_m f(\tau_m/\tau_r) = \frac{\eta(u_2-u_1)}{h} \tag{2.39}$$

2.3.2 Film thickness equation

Introducing the reduced radius of curvature $R^{-1} = R_1^{-1} + R_2^{-2}$, the film thickness equation reads:

$$h(x) = h_0 + \frac{x^2}{2R} - \frac{4}{\pi E'}\int_S \ln\left|\frac{x-x'}{x_0}\right| p(x')\,dx' \tag{2.40}$$

with x_0 the distance at which the elastic deformation is zero and h_0 a constant such that the force balance equation is satisfied.

2.3.3 Force balance equation

The force balance equation is given by:

$$\int_S p(x)\,dx = w \tag{2.41}$$

2.3.4 Friction coefficient

The friction coefficient is calculated in the middle of the film by integrating τ_m over the computational domain:

$$\mu = \frac{\int_S \tau_m\,dx}{\int_S p\,dx} \tag{2.42}$$

2.3.5 Dimensionless equations

Eqs. 2.34 to 2.42 are made dimensionless using the Hertzian dry contact parameter for this problem:

$$X = x/b, \qquad H = hR/b^2, \qquad H_0 = h_0 R/b^2 \tag{2.43}$$

$$P = p/p_H, \qquad \bar{\tau}_m = \tau_m/\tau_r \tag{2.44}$$

with:

$$b = \sqrt{\frac{8wR}{\pi E'}}, \qquad p_H = \frac{2w}{\pi b} \tag{2.45}$$

2.3.5.1 Non-Newtonian Reynolds equation

For the Eyring model, the dimensionless Reynolds equation is defined on the domain $X_a \le X \le X_b$ with $P(X_a) = P(X_b) = 0$ and the complementarity cavitation condition $P \ge 0$ everywhere.

$$\frac{\partial}{\partial X}\left[\frac{\bar{\rho}H^3}{\bar{\eta}_x \lambda}\frac{\partial P}{\partial X}\right] - \frac{\partial}{\partial X}[\bar{\rho}H] = 0 \tag{2.46}$$

with $\lambda = (12\eta_0 u_m R^2)/(b^3 p_H)$. The effective viscosity is given by:

$$\bar{\eta}/\bar{\eta}_X = -3\frac{\sinh\Sigma - \Sigma\cosh\Sigma}{\Sigma^3}\cosh(\tau_m/\tau_0), \text{ with: } \Sigma = N_2 H\frac{\partial P}{\partial X} \tag{2.47}$$

The mean shear stress follows from:

$$\sinh(\bar{\tau}_m) = N_1\frac{\bar{\eta}S}{H}\frac{\Sigma}{\sinh\Sigma} \tag{2.48}$$

with:

$$N_1 = \frac{\eta_0 u_m E'}{16 p_H b}, \qquad N_2 = \frac{p_H b}{2R\tau_r} \tag{2.49}$$

For the limiting shear stress models, the corresponding equations are:

$$\frac{\partial}{\partial X}\left[\frac{\bar{\rho}H^3}{\bar{\eta}_x\lambda}\frac{\partial P}{\partial X}\right] - \frac{\partial}{\partial X}\left[\left(1 - \frac{S}{6}N_2\frac{\partial P}{\partial X}\frac{f'(\bar{\tau}_m)}{f(\bar{\tau}_m)}\right)\bar{\rho}H\right] = 0 \tag{2.50}$$

$$\bar{\eta}/\bar{\eta}_X = f(\bar{\tau}_m) \tag{2.51}$$

$$\bar{\tau}_m f(\bar{\tau}_m) = N_1\frac{\bar{\eta}S}{H} \tag{2.52}$$

Finally, the dimensionless film thickness, force balance and friction coefficient equations become:

2.3.5.2 Film thickness equation

$$H(x) = H_0 + \frac{X^2}{2} - \frac{1}{\pi}\int_S \ln|X - X'|\,P(X')\,dX' \tag{2.53}$$

2.3.5.3 Force balance equation

$$\int_S P(X)\,dX = \frac{\pi}{2} \tag{2.54}$$

2.3.5.4 Friction coefficient

Limiting shear stress

$$\bar{\mu} = \mu\frac{p_H}{\tau_L(p_H)} = \frac{\int_S \tau_L(p_H P)\bar{\tau}_m\,dX}{\tau_L(p_H)\int_S P\,dX} \tag{2.55}$$

Eyring

$$\bar{\mu} = \mu\frac{p_H}{\tau_0} = \frac{\int_S \bar{\tau}_m dX}{\int_S P\,dX} \tag{2.56}$$

the value of α that would be used for Barus' pressure-viscosity relation. The introduction of non-Newtonian effects results in a fourth parameter $\bar{S}$ taking into account the amount of slip in the contact and the rheological behaviour of the lubricant:

$$\bar{S} = \frac{SE'}{\tau_r}\left(\frac{\eta_0 u_s}{E' R_x}\right)^{1/2} = \frac{S(L/\alpha)^2}{E'\tau_r} \tag{2.69}$$

where τ_r is τ_0 for the Eyring model and $\tau_L(p_H)$ for the limiting shear stress models.

The parameters $\bar{\alpha}$ and λ used in the set of dimensionless equations are given in terms of M, L and κ by:

$$\lambda = \left(\frac{128\pi^3}{3M^4}\right)^{1/3}\left(\frac{16\pi(\mathcal{E}-\kappa^2\mathcal{K})^5}{\kappa^4(1-\kappa^2)^5\mathcal{K}^6}\right)^{1/3} \tag{2.70}$$

$$\bar{\alpha} = \frac{L}{\pi}\left(\frac{3M}{2}\right)^{1/3}\left(\frac{\pi^2\kappa(1-\kappa^2)^2}{16(\mathcal{E}-\kappa^2\mathcal{K})^2}\right)^{1/3} \tag{2.71}$$

In the rest of this work the operating conditions are described by specifying the values of M, L, α, D, S and τ_r.

Chapter 3

Numerical techniques

The system of dimensionless equations describing non-Newtonian EHL contacts has been derived in Chapt. 2. This chapter describes the numerical methods used to solve this system. They are based on multilevel techniques. The application of multilevel techniques to EHL problems has meant a real breakthrough in the complexity of the problems that can be studied. The use of multilevel techniques, pioneered by Lubrecht [55] and Venner [71], is now becoming quite widespread owing to publications describing the method in great detail, see [74]. In the field of computational EHL the method has become almost common knowledge. Consequently, only a short description is given here. The reader interested in more details is referred to [74].

The chapter starts by listing the discretized system of equations for non-Newtonian elliptic contacts. The numerical approach used to solve this system is introduced by a short description of multilevel techniques. A description of a suitable relaxation scheme for each equation and of some implementation details follow. Subsequently, a few typical examples of shear stress distributions and traction curves are shown. The chapter is concluded with an illustration of the numerical accuracy of the friction coefficient calculations.

3.1 Discretized equations

The dimensionless system of equations describing the lubrication of non-Newtonian EHL contacts derived in Chapt. 2 can not be solved analytically in most cases. A numerical solution using an iterative procedure based on some sort of relaxation is generally required. The system of equations is therefore discretized with second-order accuracy using finite differences on a grid of mesh-size $h_X = h_Y = h$. The discretized non-Newtonian Reynolds equation is given by:

$$\frac{\epsilon^X_{i-1/2,j}P_{i-1,j} - (\epsilon^X_{i-1/2,j} + \epsilon^X_{i+1/2,j})P_{i,j} + \epsilon^X_{i+1/2,j}P_{i+1,j}}{h^2} + \kappa^2 \frac{\epsilon^Y_{i,j-1/2}P_{i,j-1} - (\epsilon^Y_{i,j-1/2} + \epsilon^Y_{i,j+1/2})P_{i,j} + \epsilon^Y_{i,j+1/2}P_{i,j+1}}{h^2} - \frac{1.5\breve{\rho}_{i,j}H_{i,j} - 2\breve{\rho}_{i-1,j}H_{i-1,j} + 0.5\breve{\rho}_{i-2,j}H_{i-2,j}}{h} = 0 \quad (3.1)$$

where:

$$\epsilon^X_{i-1/2,j} = \frac{(\bar{\rho}H^3/\bar{\eta}_X)_{i,j} + (\bar{\rho}H^3/\bar{\eta}_X)_{i-1,j}}{2\lambda} \quad , \quad \epsilon^X_{i+1/2,j} = \frac{(\bar{\rho}H^3/\bar{\eta}_X)_{i+1,j} + (\bar{\rho}H^3/\bar{\eta}_X)_{i,j}}{2\lambda}$$
$$\epsilon^Y_{i,j-1/2} = \frac{(\bar{\rho}H^3/\bar{\eta}_Y)_{i,j} + (\bar{\rho}H^3/\bar{\eta}_Y)_{i,j-1}}{2\lambda} \quad , \quad \epsilon^Y_{i,j+1/2} = \frac{(\bar{\rho}H^3/\bar{\eta}_Y)_{i,j+1} + (\bar{\rho}H^3/\bar{\eta}_Y)_{i,j}}{2\lambda} \quad (3.2)$$

For the Eyring model $\breve{\rho}_{i,j} = \bar{\rho}_{i,j}$ while for the limiting shear stress models:

$$\breve{\rho}_{i,j} = \bar{\rho}_{i,j}\left(1 - N_{2(i,j)}\frac{S}{6}\frac{(P_{i,j} - P_{i-1,j})}{h}\frac{f'(\bar{\tau}_{m(i,j)})}{f(\bar{\tau}_{m(i,j)})}\right) \quad (3.3)$$

The Reynolds equation is defined on the domain $X_a \leq X \leq X_b$, $Y_a \leq X \leq Y_b$ with boundary conditions $P = 0$ on the domain boundary. A complementarity cavitation condition is imposed on the pressure $P_{i,j} \geq 0$, $\forall i, j$.

The elastic deformation, i.e. the last term in Eq. 2.29 is discretized by approximating the pressure by a piecewise constant function $P_{k,l}$ in $X'_k - h/2 \leq X \leq X'_k + h/2$ and $Y'_k - h/2 \leq Y \leq Y'_k + h/2$. The discrete deformation at (X_i, Y_j) is given by:

$$W_{i,j} = \sum_{k=0}^{n_X}\sum_{l=0}^{n_Y} K_{ikjl}P_{k,l} \quad (3.4)$$

with K_{ikjl}:

$$K_{ikjl} = \frac{1}{\pi\mathcal{K}}\int_{Y_l-h/2}^{Y_l+h/2}\int_{X_k-h/2}^{X_k+h/2}\frac{dX'dY'}{\sqrt{\kappa^2(X_i - X')^2 + (Y_j - Y')^2}} \quad (3.5)$$

An analytical solution can be found for Eq. 3.5 reading:

$$\begin{aligned} K_{ikjl} = \frac{1}{\pi\mathcal{K}}(&|X_p|\sinh^{-1}(Y_p/X_p) + |Y_p|\sinh^{-1}(X_p/Y_p) \\ &-|X_m|\sinh^{-1}(Y_p/X_m) + |Y_p|\sinh^{-1}(X_m/Y_p) \\ &-|X_p|\sinh^{-1}(Y_m/X_p) + |Y_m|\sinh^{-1}(X_p/Y_m) \\ &+|X_m|\sinh^{-1}(Y_m/X_m) + |Y_m|\sinh^{-1}(X_m/Y_m)) \end{aligned} \quad (3.6)$$

where:

$$\begin{aligned} X_p &= X_i - X_k + h/2, & X_m &= X_i - X_k - h/2, \\ Y_p &= (Y_j - Y_l + h/2)/\kappa, & Y_m &= (Y_j - Y_l - h/2)/\kappa \end{aligned} \quad (3.7)$$

Finally, the discretized force-balance equation is given by:

$$\sum_{i=0}^{n_X}\sum_{j=0}^{n_Y} P_{i,j} = \frac{2\pi}{3} \quad (3.8)$$

3.2 Multilevel techniques

Iteratively solving systems of equations resulting from the discretization of partial differential equations on a domain with a large number of discretization points using relaxation is generally a very time consuming process. Most relaxation schemes significantly reduce the error in the first few relaxations but then the convergence stalls. Multilevel methods aim at finding a solution in the same number of operations as there are discretization points i.e. at developing a solver of $O(n)$ complexity where n is the number of points on the discretization grid. To achieve this multilevel techniques rely on an understanding of the local nature of relaxation processes which causes the slow convergence [14].

In many cases an analysis of the relaxation process shows that the high-frequency components of the error are quickly reduced in the first relaxations hence the good initial performance of the algorithm. Lower frequency components then dominate the error and as they are only slowly reduced the convergence stalls. Here, high and low frequency are relative to the discretization mesh-size. Most relaxation schemes can therefore be described as good smoothers but bad solvers.

The good smoothing properties of relaxation schemes can be used to develop fast solvers in the following way: consider the error on a grid of mesh size h. After a few relaxations the error is smooth and can be represented without loss of accuracy on a coarser grid, say a grid of mesh-size $H = 2h$. On the coarse grid, the relaxation scheme can be applied once more to solve the error. The convergence will automatically be faster because the mesh-size has increased. Moreover, on a coarser grid the error is not so smooth anymore and fast convergence can be expected in the first few relaxations. Once the solution has been found on the coarse grid it can be interpolated to the fine grid to correct the solution obtained there. If the fine grid has a large number of discretization points it is likely that on the coarse grid the number of points will still be significant and the rate of convergence will accordingly be low. However, an even coarser grid can then be used to increase the convergence speed of the solution process on the coarse grid in the same manner. In this way a recursive algorithm can be built which quickly reduces all the components of the error using different grids. Eventually a grid is reached containing only a few points where the equations can be solved in only a few iterations. To increase the convergence even further the coarse grids can also be used to provide an accurate initial approximation: the problem is defined on a coarse grid, solved using the recursive algorithm described above and its solution interpolated to the fine grid where it is used as an initial approximation. This procedure can also be applied recursively and is called Full MultiGrid or FMG.

Summarizing, the multigrid principle is to use grids of different size and to reduce on each

grid the high-frequency components corresponding to this grid. A few relaxations only are needed on each grid as smoothing is required and not solving. For more information, the reader is referred to Brandt [14], Briggs [17] and Venner and Lubrecht [74].

The relaxation schemes ensuring acceptable convergence rates and stability are described next for the modified Reynolds, film thickness and force balance equations. Note that the discretized equations shown above correspond to the equations on the finest grid. On the coarser grids the right hand side of the equations changes to reflect the fact that on those levels the error is solved. Because the equations are non-linear the Full Approximation Scheme (FAS) is used, see [74].

3.3 Reynolds equation

3.3.1 Newtonian case

The treatment of the Reynolds equation for a Newtonian lubricant is explained first as it forms the basis on which non-Newtonian effects are incorporated. The Reynolds equation is an integro-differential equation as the film thickness depends on the pressure with coefficients that change abruptly and significantly over the domain. The domain can be divided in two regions: a low-pressure region where the differential character of the equation dominates and a high-pressure region where due to piezo-viscous effects the Poiseuille terms become negligible and the integral character of the equation dominates.

In the low-pressure region, the Reynolds equation reduces to the anisotropic Poisson equation with varying coefficients:

$$\frac{\partial}{\partial X}\left[\epsilon\frac{\partial P}{\partial X}\right]+\kappa^2\frac{\partial}{\partial Y}\left[\epsilon\frac{\partial P}{\partial Y}\right]=f(X,Y) \tag{3.9}$$

Simple one-point Gauss-Seidel relaxation is stable and efficient if the anisotropy is not too pronounced. If the ellipticity is important, one direction becomes loosely coupled to the other and the convergence rate decreases [75]. An acceptable convergence rate can be restored if the coupling is artificially reinforced by means of line relaxation [2].

In the high-pressure region, the Reynolds equation reduces to:

$$\frac{\partial(\bar{\rho}H)}{\partial X}=0 \tag{3.10}$$

In this case too, there is a loss of coupling in one direction and line relaxation is required. Line Gauss-Seidel relaxation is however not stable in this case. Due to the integral character of the equation the changes introduced by the relaxation do not remain local

[71]. The changes can be forced to remain local using distributive relaxation in which changes are applied not only at one point but are also distributed to its neighbours according to a given pattern.

The boundary between the two regions is set by the value of ϵ/h^2. It can be shown that when $\epsilon/h^2 \leq 0.3$ line distributive Jacobi relaxation should be used whereas when $\epsilon/h^2 > 0.3$ line Gauss-Seidel may be used without stability problems [71]. In practice, when solving for one line, the criterion is applied on the preceeding and following lines. If for both lines, $\epsilon/h^2 > 0.3$, line Gauss-Seidel is applied. If not line distributed Jacobi is applied. This ensures that, in highly loaded cases, line distributive Jacobi is used whenever there is a risk of instability.
In addition to these two regions, one may also distinguish a third: the cavitated region. The analysis of the effect of cavitation on the convergence rate of the multigrid solver has shown that an additional point Gauss-Seidel relaxation sweep along the cavitation boundary is needed to restore a good convergence rate. In the solver build here, point Gauss-Seidel has been used in this region.
Finally, because the equations are non-linear under-relaxation is needed. The under-relaxation factors used in this work range from 0.8 to 0.3 for the line Gauss-Seidel, 0.6 to 0.1 for line distributed Jacobi and 0.6 to 0.1 for the point Gauss-Seidel scheme used along the cavitation boundary.

3.3.2 Influence of non-Newtonian effects

The introduction of non-Newtonian behaviour affects the character of the Reynolds equation in several ways:

1. The anisotropy is increased due to the difference between $\bar{\eta}_X$ and $\bar{\eta}_Y$. However this is not harmful for the stability and efficiency of the solver as line relaxation is already applied.

2. In the high-pressure region large non-Newtonian effects may lead to a decrease of $\bar{\eta}_X$ and/or $\bar{\eta}_Y$ such that the Poiseuille terms become significant. It does not happen for the Eyring model for which the decrease of the effective viscosities is moderate but may occur for the limiting shear stress models.

In this case patches appear where Gauss-Seidel relaxation should be applied in the midst of a distributed Jacobi region. The changes of film thickness and pressure required to solve the equation are then too large and cause instability. From a physical point of view, the occurrence of significant distortion of the film and pressure profiles in the central region of the contact is not likely. For this reason, it seems best to decouple almost completely the film and pressure calculations from the shear stress calculations. In practice whenever H and P are such that $\bar{\tau}_X = \bar{\tau}_m + \mathcal{N}_2 H\partial P/\partial X \geq 1$, $\bar{\tau}_X$ is chosen very close to but smaller than 1 for the calculation of the effective viscosities. It means that the pressure and

film thickness profiles are not allowed to vary significantly from their Newtonian values. It is obviously a crude approximation but the consequences for the friction coefficient calculations are small. Indeed at this end of the traction curve the values of the friction coefficient are close to 1 and the error made can not be large. Note that the perturbational approach described in [24] does not explicitely use $(h/2)(\partial p/\partial x)$. The approach proved nevertheless unstable due to the overestimated decrease of the effective viscosities in the high-pressure region. This lead Ehret et al. [26] to use Newtonian film thickness and pressure profiles for their traction calculations.

As a consequence of the approach chosen, the limiting shear stress models can not be used for the study of roughness effects on friction later in this work. Indeed the variation of friction due to roughness are caused by pressure and film thickness variations that the present approach can not properly describe. The analysis of roughness effects presented in Chapt. 6 is therefore limited to the Eyring model.

Summarizing, the effects of non-Newtonian behaviour are negligible for the Eyring model and voluntarily limited for the limiting shear stress models. The relaxation schemes developed for the Newtonian case can therefore be applied without changes to the solution of the non-Newtonian Reynolds equation.

3.3.3 Implementation

Two different schemes are required to solve the non-Newtonian Reynolds equation. The switch from one to the other depends on the value of min $(\epsilon^X/h^2, \epsilon^Y/h^2)$. Line Gauss-Seidel relaxation is used if min $(\epsilon^X/h^2, \epsilon^Y/h^2) > 0.3$. Otherwise line distributed Jacobi is used.

3.3.3.1 Line Gauss-Seidel relaxation

The non-Newtonian Reynolds equation is relaxed along a line of constant Y to obtain the pressure. At each relaxation sweep a new approximation $\bar{P}_{i,j}$ in each point i for a given j is computed simultaneously from the previous approximation $\tilde{P}_{i,j}$, $\bar{P}_{i,j} = \tilde{P}_{i,j} + \delta_i$ and the changes are applied immediately. The value of the changes δ_i can be obtained from:

$$\frac{\epsilon^X_{i+1/2,j}[(P_{i+1,j}+\delta_{i+1})-(P_{i,j}+\delta_i)] + \epsilon^X_{i-1/2,j}[(P_{i-1,j}+\delta_{i-1})-(P_{i,j}+\delta_i)]}{h_x^2} + \kappa^2 \frac{\epsilon^Y_{i,j+1/2}[P_{i,j+1}-(P_{i,j}+\delta_i)] + \epsilon^Y_{i,j-1/2}[P_{i,j-1}-(P_{i,j}+\delta_i)]}{h_y^2} - \frac{1.5\check{\rho}_{i,j}\bar{H}_{i,j} - 2.0\check{\rho}_{i-1,j}\bar{H}_{i-1,j} + 0.5\check{\rho}_{i-2,j}\bar{H}_{i-2,j}}{h_x} = 0 \quad (3.11)$$

where for each i, $\bar{H}_{i,j} = \tilde{H}_{i,j} + \sum_k K_{i,k,j,j}\delta_k$. The magnitude of the kernel decreases so fast with distance that this summation may be approximated by its three first terms only:

$$\bar{H}_{i,j} = \tilde{H}_{i,j} + \sum_{k=i-1}^{i+1} K_{i,k,j,j}\delta_k \quad (3.12)$$

Eq. 3.11 may be rewritten:

$$q_{i+1}\delta_{i+1} + q_i\delta_i + q_{i-1}\delta_{i-1} + q_{i-2}\delta_{i-2} + q_{i-3}\delta_{i-3} = r_{i,j} \quad (3.13)$$

where $r_{i,j}$ is the residual. This leads to a band matrix which can be solved using Gaussian elimination. The coefficients of the band matrix are given by:

$$q_{i+1} = \frac{\epsilon^X_{i+1/2,j}}{h_x^2} - \frac{1.5\check{\rho}_{i,j}K_{i,i+1,j,j}}{h_x} \quad (3.14)$$

$$q_i = -\left(\frac{\epsilon^X_{i+1/2,j}+\epsilon^X_{i-1/2,j}}{h_x^2} + \kappa^2\frac{\epsilon^Y_{i,j+1/2}+\epsilon^Y_{i,j-1/2}}{h_y^2}\right) - \frac{1.5\check{\rho}_{i,j}K_{i,i,j,j} - 2.0\check{\rho}_{i-1,j}K_{i-1,i,j,j}}{h_x} \quad (3.15)$$

$$q_{i-1} = \frac{\epsilon^X_{i-1/2,j}}{h_x^2} - \frac{1.5\check{\rho}_{i,j}K_{i,i-1,j,j} - 2.0\check{\rho}_{i-1,j}K_{i-1,i-1,j,j} + 0.5\check{\rho}_{i-2,j}K_{i-2,i-1,j,j}}{h_x} \quad (3.16)$$

$$q_{i-2} = -\frac{-2.0\check{\rho}_{i-1,j}K_{i-1,i-2,j,j} + 0.5\check{\rho}_{i-2,j}K_{i-2,i-2,j,j}}{h_x} \quad (3.17)$$

$$q_{i-3} = -\frac{0.5\check{\rho}_{i-2,j}K_{i-2,i-3,j,j}}{h_x} \quad (3.18)$$

3.3.3.2 Line distributed Jacobi relaxation

For the line distributed Jacobi relaxation, the changes to the pressure computed at one point of the line are distributed to its neighbours. This is equivalent to saying that at a given point the new pressure $\bar{P}_{i,j}$ results from the summation of the changes coming from neighbouring points and of the old approximation $\tilde{P}_{i,j}$, $\bar{P}_{i,j} = \tilde{P}_{i,j} + \delta_{i,j} - (\delta_{i+1,j} + \delta_{i-1,j} + \delta_{i,j+1} + \delta_{i,j-1})/4$. The changes are applied only at the end of a complete relaxation sweep over the whole contact. They are obtained from:

$$\frac{\epsilon^X_{i+1/2,j}[(P_{i+1,j}+\delta_{i+1}-(\delta_i+\delta_{i+2})/4)-(P_{i,j}+\delta_i-(\delta_{i-1}+\delta_{i+1})/4)]}{h_x^2}+$$
$$\frac{\epsilon^X_{i-1/2,j}[(P_{i-1,j}+\delta_{i-1}-(\delta_{i-2}+\delta_i)/4))-(P_{i,j}+\delta_i-(\delta_{i-1}+\delta_{i+1})/4)]}{h_x^2}+$$
$$\kappa^2\,\frac{\epsilon^Y_{i,j+1/2}[P_{i,j+1}-\delta_i/4-(P_{i,j}+\delta_i-(\delta_{i-1}+\delta_{i+1})/4)]}{h_y^2}+$$
$$\kappa^2\,\frac{\epsilon^Y_{i,j-1/2}[P_{i,j-1}-\delta_i/4-(P_{i,j}+\delta_i-(\delta_{i-1}+\delta_{i+1})/4)]}{h_y^2}-$$
$$\frac{1.5\breve{\rho}_{i,j}\bar{H}_{i,j}-2.0\breve{\rho}_{i-1,j}\bar{H}_{i-1,j}+0.5\breve{\rho}_{i-2,j}\bar{H}_{i-2,j}}{h_x}=0 \quad (3.19)$$

where for each i $\bar{H}_{i,j}=\tilde{H}_{i,j}+\sum_k \Delta K_{i,k,j,j}\delta_k$ and $\Delta K_{i,i,j,j}=K_{i,i,j,j}-(K_{i,i-1,j,j}+K_{i,i+1,j,j}+K_{i,i,j,j-1}+K_{i,i,j,j+1})/4$. Taking once again the three most important terms of the summation only, the coefficients of the matrix to solve for each line are:

$$q_{i+2}=-\frac{\epsilon^X_{i+1/2,j}}{4h_x^2} \quad (3.20)$$

$$q_{i+1}=\frac{5\epsilon^X_{i+1/2,j}+\epsilon^X_{i-1/2,j}}{4h_x^2}+\kappa^2\,\frac{\epsilon^Y_{i,j+1/2}+\epsilon^Y_{i,j-1/2}}{h_y^2}-\frac{1.5\breve{\rho}_{i,j}\Delta K_{i,i+1,j,j}}{h_x} \quad (3.21)$$

$$q_i=-\frac{5}{4}\left(\frac{\epsilon^X_{i+1/2,j}+\epsilon^X_{i-1/2,j}}{h_x^2}+\kappa^2\,\frac{\epsilon^Y_{i,j+1/2}+\epsilon^Y_{i,j-1/2}}{h_y^2}\right)$$
$$-\frac{1.5\breve{\rho}_{i,j}\Delta K_{i,i,j,j}-2.0\breve{\rho}_{i-1,j}\Delta K_{i-1,i,j,j}}{h_x} \quad (3.22)$$

$$q_{i-1}=\frac{\epsilon^X_{i+1/2,j}+5\epsilon^X_{i-1/2,j}}{4h_x^2}+\kappa^2\,\frac{\epsilon^Y_{i,j+1/2}+\epsilon^Y_{i,j-1/2}}{h_y^2}$$
$$-\frac{1.5\breve{\rho}_{i,j}\Delta K_{i,i-1,j,j}-2.0\breve{\rho}_{i-1,j}\Delta K_{i-1,i-1,j,j}+0.5\breve{\rho}_{i-2,j}\Delta K_{i-2,i-1,j,j}}{h_x} \quad (3.23)$$

$$q_{i-2}=-\frac{\epsilon^X_{i-1/2,j}}{4h_x^2}-\frac{-2.0\breve{\rho}_{i-1,j}\Delta K_{i-1,i-2,j,j}+0.5\breve{\rho}_{i-2,j}\Delta K_{i-2,i-2,j,j}}{h_x} \quad (3.24)$$

$$q_{i-3}=-\frac{0.5\breve{\rho}_{i-2,j}\Delta K_{i-2,i-3,j,j}}{h_x} \quad (3.25)$$

3.3.3.3 Cavitation boundary

The Reynolds equation has a complementarity equation imposing $P \geq 0$. In practice whenever $P_{i,j} < 0$, $P_{i,j}$ is set to 0. The position of the cavitation boundary is not fixed, it may vary during the iterative solution process. Line relaxation schemes lack flexibility

to treat free boundary problems: the equation is solved at each point of the line with the information of the previous entire sweep. If the solution at point (i,j) is put to 0, this information is not known to the following points which will take into account the previous value of the pressure at point (i,j). The resolution of the Reynolds equation in the points close to the cavitation boundary as calculated in the previous sweep should be decoupled from their neighbouring points. In that way a sort of point Gauss-Seidel relaxation is introduced. In practice, when a point is close to the boundary, the extra-diagonal terms of the matrix are put to zero.

The position of the free boundary is local information. Accordingly, in a multilevel solver the localisation of the boundary should be done on the finest level. On coarser levels and in the transfers between the different levels special treatment is used close to the cavitation boundary, see [74].

3.4 Film thickness equation

The evaluation of the elastic deformation integral in a straightforward way requires $O(n^2)$ operations, with n the number of points on the grid. If the evaluation is performed in this way the gain in complexity obtained by applying multilevel methods to the other equations is lost and the overall complexity of the EHL solver would be $O(n^2)$. However Brandt and Lubrecht [15] showed that it was possible to reduce this complexity to $O(n)$ for smooth kernels and $O(n \ln n)$ for singular smooth kernels.

The method developed is called multilevel multi-integration. It takes advantage of the smoothness of the kernel to interpolate it on coarser grids where the evaluation can be performed at a fraction of the cost needed on the fine grid. If the kernel is singular, as the elastic deformation kernel, the errors introduced by interpolating the kernel close to the singularity need to be corrected. Local correction patches are then defined. The size of the patches depends on the kernel [75] but can be taken small enough such that at most $O(\ln(n))$ extra work is done per grid-point.

In practice the film thickness is calculated at the end of a relaxation sweep with the new values of the pressure obtained from the Reynolds equation.

3.5 Force balance equation

The force balance equation is relaxed indirectly by changing the value of the mutual approach Δ. This happens on the coarsest level only. One reason for this is that the changes caused by the relaxation of the force balance equation are global, i.e. low frequency, and should therefore be relaxed on the coarsest level. A second reason is that on the coarsest grid, relaxation is efficient enough to accommodate the changes in film thickness caused by the relaxation of the force balance equation. There Δ may be changed and the residu-

als of the Reynolds equation reduced significantly before transferring the corrections to a finer level. On the finest level only very small changes of Δ would be acceptable without ruining the stability of the scheme and in order for these changes to be accommodated quickly.

3.6 Characteristic results and numerical accuracy

The system of equations describing the lubrication of non-Newtonian EHL contacts is solved numerically according to the method described in the previous sections. The output of the calculations are the film thickness, pressure and shear stress distributions. From the latter the friction coefficient can be calculated.

It is well-known that the film thickness and pressure profiles obtained with a lubricant following the Eyring model differ only slightly from Newtonian results [20, 51, 42]. The ratio of minimum to central film thickness varies slightly with slip and the amplitude of the pressure spike decreases. The approach chosen in this work to consider limiting shear stress models also results in distributions close to those obtained for a Newtonian situation. In all calculations performed in this work, the main characteristics of Newtonian EHL contacts were therefore found. An almost flat central plateau with a constriction at the outlet for the film thickness and a roughly semi-ellipsoidal pressure distribution approaching the dry contact solution for high loads and/or low speeds, see Fig. 3.1. For more information about the characteristics of Newtonian EHL contacts the reader is referred to [71].

The pressure, film thickness and shear stress distributions obtained for the Eyring model are presented for one case in Fig. 3.1(a-c). In Fig. 3.1(d) the shear stress distribution obtained using the circular model ($n = 2$) for the same conditions is shown. The conditions are $M = 500$, $L = 6$ corresponding to a Hertzian pressure of 0.789 GPa, $\tau_0 = 4$ MPa or $\gamma = 0.06$ and the slip is 0.1%. The lubricant is incompressible and its pressure-viscosity behaviour is given by Barus.

For the Eyring model the shear stress distribution has a semi-ellipsoidal shape with a maximum around $\tau = 8\tau_0$. With the circular model, the limiting shear stress is reached under those conditions over a large part of the contact zone.

The variation of the shear stress distributions and of the friction coefficient with slip are presented in Fig. 3.2(a-f) for the Eyring and the circular ($n = 2$) models. A circular contact is considered lubricated with either an incompressible fluid following the Barus viscosity-pressure relation or a compressible fluid following the Roelands viscosity-pressure relation. The conditions are identical to those taken to calculate the distributions shown in Fig. 3.1. The slip is varied from 0.005 to 10%. The shear stress distributions are presented by means of cross-sections in the running direction ($Y = 0$, Fig. 3.2(a)(b)) and in the transverse direction ($X = 0$, Fig. 3.2(c)(d)). The overall reduced friction coefficient is given as a function of slip in Fig. 3.2(e)(f).

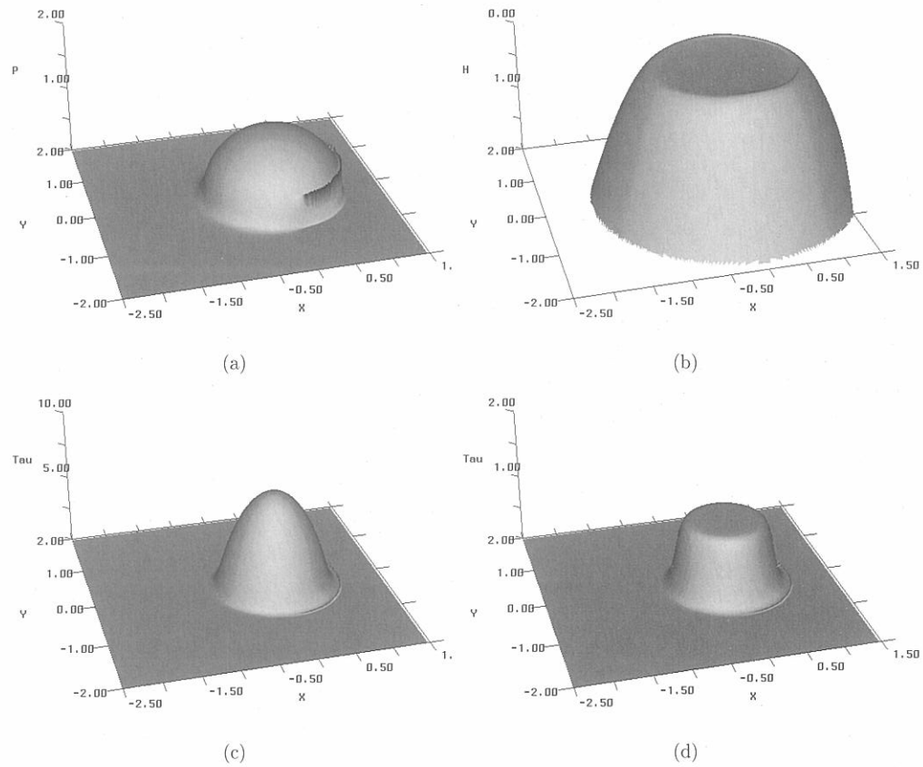

Figure 3.1: Pressure (a), film thickness (b) and shear stress distributions (c)(d) obtained with the Eyring model (a-c) and the circular model (d). $M = 500$, $L = 6$, $S = 0.1\%$, $\tau_0 = 4$ MPa or $\gamma = 0.06$. (257x257).

In this figure it can be seen that the shear stress increases with slip for both rheological models. For the Eyring model the shape of the shear stress distribution remains roughly constant but its magnitude increases with slip. For the circular model, at low slip values the shape does not change but only the magnitude increases with slip. However at higher slip rates, the limiting shear stress is reached in the centre of the contact and a $\tau = \tau_L$ region spreads from the centre to the sides of the contact.

The pressure-viscosity relation chosen influences both the magnitude and the shape of the shear stress distribution. The Roelands relation predicts significantly lower values for the viscosity than the Barus relation for $p \geq 0.5$ GPa. Accordingly, in the centre of the contact where $p \sim p_H$ the shear stress is lower for the contact where the lubricant follows Roelands' relation. At the edges of the contact where the pressures are low, however, both models predict almost identical shear stress distributions.

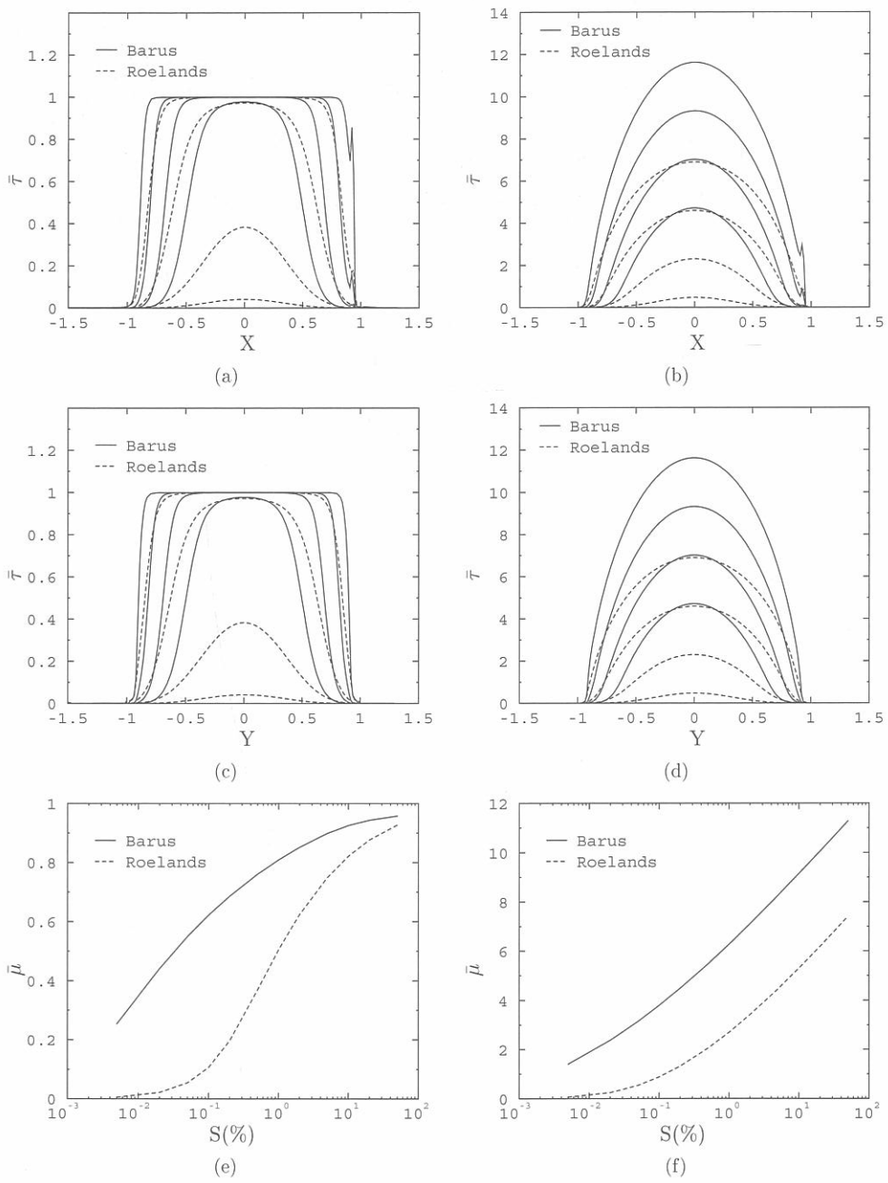

Figure 3.2: Shear stress distributions $\bar{\tau}(X, Y = 0)$(a)(b), $\bar{\tau}(X = 0, Y)$(c)(d) and reduced friction coefficient $\bar{\mu}$(e)(f) as a function of slip. For the shear stress distributions the curves correspond in increasing order of magnitude to $S = 0.01,\ 0.1,\ 1$ and 10%. Left column: limiting shear stress model; right column: Eyring model. (257x257).

Note that in the case of the circular model, beyond a certain value of the slip rate the limiting shear stress is reached in most of the contact and the differences between the results of the different piezo-viscous models decrease. This is reflected in the traction curves, see Fig. 3.2(e): for the large values of S the predicted values of the reduced friction coefficient $\bar{\mu}$ for both models are quite close. At that point $\bar{\mu}$ is close to its asymptotic value of 1. By contrast, for the Eyring model the traction curves for the different piezo-viscous relations do not come closer to one another, see Fig. 3.2(f). On a log-linear graph the traction curves show a linear increase of $\bar{\mu}$ with S beyond $S \sim 1\%$ which is characteristic for the Eyring model.

The numerical accuracy of the friction coefficient calculations can be estimated by comparing the value of $\bar{\mu}$ obtained using different grid densities. This is presented in Table 3.1 for $M = 500,\ L = 6,\ S = 0.1\%,\ \tau_0 = 4$ MPa or $\gamma = 0.06$ and $S = 1\%$. The reduced friction coefficient is given for both rheological models for the case of a piezo-viscous behaviour according to Barus' relation, $\bar{\mu}_B$, and according to Roelands' relation, $\bar{\mu}_R$. The difference between the values obtained on two subsequent grids, $|\bar{\mu}^h - \bar{\mu}^H|$, is also given. The difference decreases in all cases by a factor 4 or more when the mesh-size is halved showing that the friction coefficient is converging with second order accuracy. The oscillation observed in the case of the circular model and Barus' piezo-viscous behaviour is not unusual: it can also occur in a similar way in film thickness calculations and may be caused by the pressure spike.

n_xxn_y	Eyring				circular			
	$\bar{\mu}_B$	$\lvert\bar{\mu}^h - \bar{\mu}^H\rvert$	$\bar{\mu}_R$	$\lvert\bar{\mu}^h - \bar{\mu}^H\rvert$	$\bar{\mu}_B$	$\lvert\bar{\mu}^h - \bar{\mu}^H\rvert$	$\bar{\mu}_R$	$\lvert\bar{\mu}^h - \bar{\mu}^H\rvert$
65x65	6.6515		3.0607		0.8266		0.5694	
129x129	6.3298	0.3217	2.7562	0.3045	0.8121	0.0145	0.5165	0.0529
257x257	6.2669	0.0629	2.6915	0.0647	0.8095	0.0026	0.5046	0.0119
513x513	6.2572	0.0097	2.6758	0.0157	0.8101	0.0006	0.5017	0.0029

Table 3.1: Reduced friction coefficient $\bar{\mu}$ as a function of the grid density.

Between the values of $\bar{\mu}$ obtained on a grid of 257x257 and 513x513 points, the difference is less than 1%. All calculations in this work are performed on grids of 257x257 points so the error is generally below 2%.

Chapter 4

Friction in isothermal smooth contacts

The tools developed to analyze numerically non-Newtonian EHL contacts have been described in Chapt. 3 together with examples of shear stress distributions and traction curves. In this chapter the numerical solver is used for an extensive analysis of the friction generation in isothermal smooth EHL contacts. A large number of cases is considered covering a wide range of variations of the operating conditions for both types of rheological models: the Eyring and the limiting shear stress models. It is shown that a unique parameter exists that characterizes the friction generation. In terms of this new parameter all computed results collapse on a generalized traction curve. The shape of this curve reflects the type of rheological model chosen. A validation of the observations is then performed using experimental results published in the literature. The chapter is concluded with a comparison of the Eyring and limiting shear stress models. It is shown that a relation between τ_0 and τ_L can be found such that both models predict the same friction.

4.1 Contacts, conditions, lubricant characterization

In isothermal smooth EHL contacts, the level of friction depends on three factors: the properties of the lubricant, the operating conditions and the contact geometry. The properties of the lubricant are its rheological parameters, γ or τ_0, its compressibility and its piezo-viscous behaviour. The operating conditions (load, speed etc..) can be represented by three dimensionless parameters M, L and $\bar{S}$, see Chapt. 2. Finally, the contact geometry can be a line (band) $R_X/R_Y = 0$, elliptic $R_X/R_Y \neq 1$ or circular $R_X/R_Y = 1$. Friction generation is mapped over the entire range of variations by means of 6 cases. The cases are defined as:

circ IB	Circular contact with an incompressible lubricant following Barus' pressure-viscosity relation, $\alpha = 22$ GPa^{-1}.
circ CR	Circular contact with a compressible lubricant following Roelands' pressure-viscosity relation, $\alpha = 22$ GPa^{-1} and $z_R = 0.67$.
circ CY	Circular contact with a compressible lubricant following Yasutomi's pressure-viscosity relation corresponding to HVI 650 at 100°C, $\alpha = 17.7$ GPa^{-1}, see Appendix.
$R_X/R_Y = 1/2$ CR	Elliptic contact with a compressible lubricant following Roelands' pressure-viscosity relation, $\alpha = 22$ GPa^{-1} and $z_R = 0.67$.
$R_X/R_Y = 1/5$ CR	Elliptic contact with a compressible lubricant following Roelands' pressure-viscosity relation, $\alpha = 22$ GPa^{-1} and $z_R = 0.67$.
line IB	Line contact with an incompressible lubricant following Barus' pressure-viscosity relation, $\alpha = 22$ GPa^{-1}.

For each case, the operating conditions are varied widely: $50 \leq M \leq 1000$, $5 \leq L \leq 20$. This corresponds to Hertzian pressures ranging from $p_H = 0.3$ to $p_H = 4$ GPa. The slip is varied from very low values up to 2%. For the Eyring model $2 \leq \tau_0 \leq 8$ MPa. For the limiting shear stress models $0.06 \leq \gamma \leq 0.1$ and $\tau_{L0} = 10^5$ Pa.

4.2 Numerical analysis

An analysis is performed to identify the mechanism of friction generation using the friction data computed for the cases described above. Using multiple regression on the case in which the smallest number of parameters appear, circ IB, it can be shown that the friction depends on a combination of the parameters M, L and $\bar{S}$. Subsequently, the physical quantities represented by this combination are identified resulting in a parameter that reflects the mechanism of friction generation.

4.2.1 Eyring model

The Eyring model is considered first. In view of deriving a correlation between the variables describing the operating conditions and friction, the case presenting the smallest number of variables is chosen to start with: circ IB. The friction data calculated for the range of values of M, L and $\bar{S}$ is analyzed with multiple regression. It can be shown that the influence of the various variables on the reduced friction coefficient $\bar{\mu}$ can be combined in one parameter, see Fig. 4.1.

$$\bar{\mu} = f\left(\bar{S}^{1/4} M L^3\right) \tag{4.1}$$

Using $\bar{\alpha} = L/\pi\,(3/2M)^{1/3}$, Eq. 4.1 can be rewritten as:

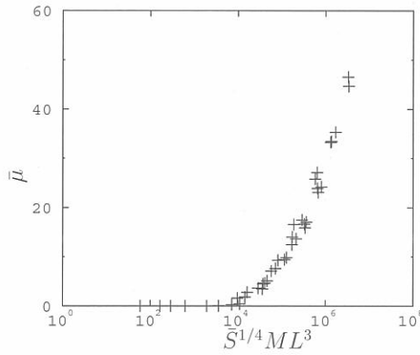

Figure 4.1: Computed reduced friction coefficient, $\bar{\mu}$, as a function of $\bar{S}^{1/4} M L^3$. Circ IB.

$$\bar{\mu} = f(\bar{S}\bar{\alpha}^{12}) \tag{4.2}$$

Taking the high power of $\bar{\alpha}$ as a representation of the viscosity, the reduced coefficient of friction appears to be related to the viscosity at the centre of the contact multiplied by a parameter representing the slip. This strongly suggests that the underlying physical parameter is the shear stress in the centre, $\bar{\tau}_c$:

$$\bar{\mu} = f\left(\frac{\bar{\eta}(p_H)\bar{S}}{H_c}\right) = f\left(\bar{\tau}_c\right) \tag{4.3}$$

where $H_c = 1.7\,M^{-1/9}L^{3/4}$ is the central film thickness, see [71]. Eq. 4.3 provides an understanding of the mechanism of friction generation where Eq. 4.1 only gives a combination of variables. It indicates that the friction coefficient is determined by the shear stress in the centre of the contact, $\bar{\tau}_c$. This is confirmed by Fig. 4.2(a) where the reduced friction coefficient is plotted as a function of $\bar{\tau}_c$: the data points now fall closer together on a single line, a friction "master" curve.

For other viscosity-pressure relations or contact configurations the mechanism of friction generation remains the same: the shear of a highly pressurized mostly uniform lubricant film in the centre of the contact. This is shown in Fig. 4.2(b) where the friction results of the other cases are added and also fall on the same line as circ IB when plotted as a function of $\bar{\tau}_c$.

The friction mastercurve obtained is accurately approximated by:

$$\bar{\mu} = \sinh^{-1}(\bar{\tau}_c/5) \tag{4.4}$$

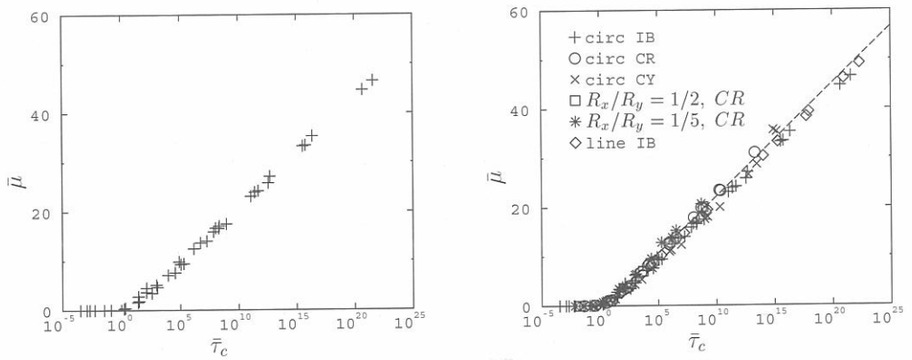

(a) (b)

Figure 4.2: Computed reduced friction coefficient, $\bar{\mu}$, as a function of $\bar{\tau}_c$. (a) Circ IB, (b) all cases. The dotted line is given by Eq. 4.4.

The shape of the curve reflects the rheological model chosen. The constant 1/5 was found by curvefitting the data points and can be seen as the result of an averaging of the shear stress distribution over the contact. This is confirmed by the fact that a simplified analytical analysis of the shear stress distribution in the centre of the contact would give a similar value, see [35].

Summarizing, it seems that for rolling/sliding EHL contacts in which the lubricant exhibits non-Newtonian behaviour following the Eyring model, the coefficient of friction is directly related to a characteristic shear stress $\bar{\tau}_c$. This $\bar{\tau}_c$ reflects the mechanism of friction generation, the shear of a highly pressurized film of lubricant. The form of the resulting generalized traction curve, Eq. 4.4, mirrors the rheological model chosen.

4.2.2 Limiting shear stress models

It is expected that the choice of the limiting shear stress type of models instead of the Eyring model has little influence on the mechanism of friction in sliding contacts. Only the response to shear and the magnitude and behaviour of the resultant friction coefficient will differ. Hence, the parameter $\bar{\tau}_c$ should still be the characteristic parameter determining the value of $\bar{\mu}$ for the limiting shear stress models with Eq. 4.4 replaced by another form.

This is illustrated below with the circular model, $n = 2$. The friction data obtained for the case circ IB is plotted in Fig. 4.3 as a function of $\bar{\tau}_c$. Note that now $\bar{S} = (L/\alpha)^2/(E'\tau_L(p_H))$ and $\bar{\mu} = \mu p_H/\tau_L(p_H)$.

The figure shows that the data points follow a single curve but a large spread occurs in

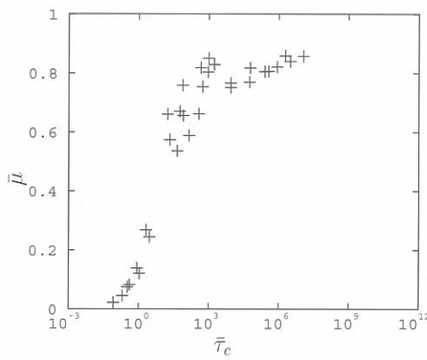

Figure 4.3: Computed reduced friction coefficient $\bar{\mu}$ as a function of $\bar{\tau}_c$ for the circular model ($n = 2$). Circ IB.

the transition region where the friction coefficient starts to approach its limiting value and its rate of increase with $\bar{\tau}_c$ decreases strongly. It implies that $\bar{\tau}_c$ still crudely represents the friction generation mechanism but apparently it is not only the shear in the centre that determines the value of $\bar{\mu}$.

To identify the origin of the spread, the shear stress distribution obtained with the circular model along the central line ($Y = 0$) for increasing slip i.e. increasing friction coefficient, is compared to that obtained under the same conditions with the Eyring model, see Fig. 4.4.

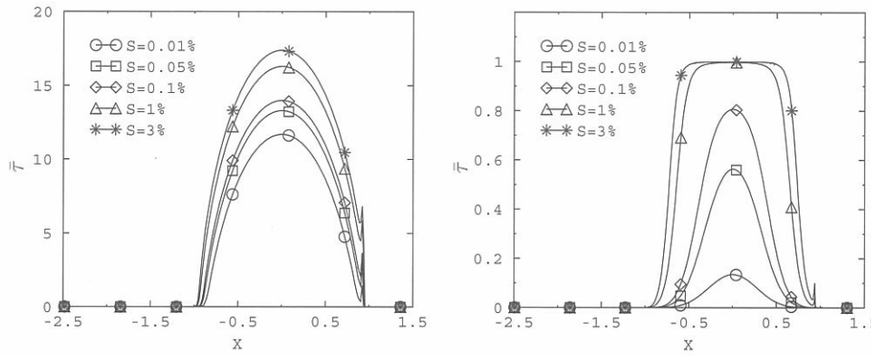

(a) Eyring (b) $n = 2$

Figure 4.4: Dimensionless shear stress profiles in the running direction ($Y = 0$) for the Eyring model and the circular model. Circ IB, $M = 500$, $L = 8$, $\tau_0 = 2$MPa, $\gamma = 0.1$.

The shape of the distribution for the Eyring model remains roughly the same when the slip increases: it is dominated by the shear stress value in the centre of the contact. For low slip values the use of the circular model gives a shear stress profile with a shape similar to that obtained with the Eyring model but very soon the limiting shear stress is reached and a region where $\tau = \tau_L$ starts to spread. So, beyond a certain point, the level of friction is no longer determined entirely by the value of $\bar{\tau}_c$ at the the central point but by the growth of a $\tau = \tau_L$ patch. An unifying parameter for this case needs to reflect the fact that a proportion of the contact is covered by a $\tau = \tau_L$ patch. This can be achieved by calculating $\bar{\tau}_c$ using the average value $\bar{p}$ instead of p_H. However, this should be done only for high values of p_H as for low values it is still the value of the shear stress in the centre that determines the frictional behaviour as for the Eyring model. A simple way to switch from the use of p_H to $\bar{p}$ is to define a pressure quantity p^* which approximates p_H for low values of p_H and $\bar{p}$ for large values of p_H:

$$p^* = p_H \left(1 - \chi \frac{p_H/10^9}{1 + p_H/10^9}\right) \tag{4.5}$$

The value of χ in Eq. 4.5 depends on the contact geometry: for circular and elliptic contacts, $\bar{p} = (2/3)p_H$ so $\chi = 1/3$ whereas for line contacts $\bar{p} = (\pi/4)p_H$ so $\chi = 1 - \pi/4$.

Fig. 4.5(a) shows the same data points as plotted in Fig. 4.3 but presented in terms of $\bar{\tau}_c(p^*)$ where p^* is given by Eq. 4.5. The points now fall much closer together.

The friction results obtained for the other cases are now plotted together with circ IB in Fig. 4.5(b) as a function of $(\bar{\tau}_c(p^*),\ \bar{\mu})$. The friction data computed for the other cases fall on the same curve as the circ IB case, which confirms that $\bar{\tau}_c(p^*)$ accurately represents the friction generation mechanism.

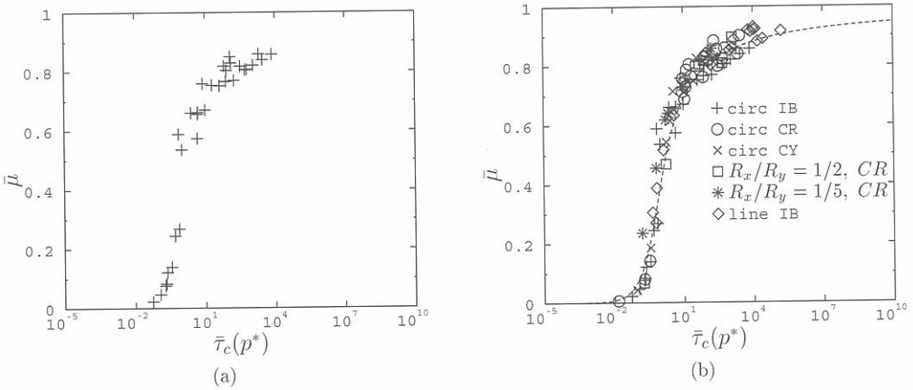

(a) (b)

Figure 4.5: Computed reduced friction coefficient $\bar{\mu}$ as a function of $\bar{\tau}_c(p^*)$ for the circular model ($n = 2$). (a) circ IB, (b) all cases. The dotted line is given by Eq. 4.7.

Finally Fig. 4.6 shows the data obtained for the other three limiting shear stress models plotted as a function of $\bar{\tau}_c(p^*)$.

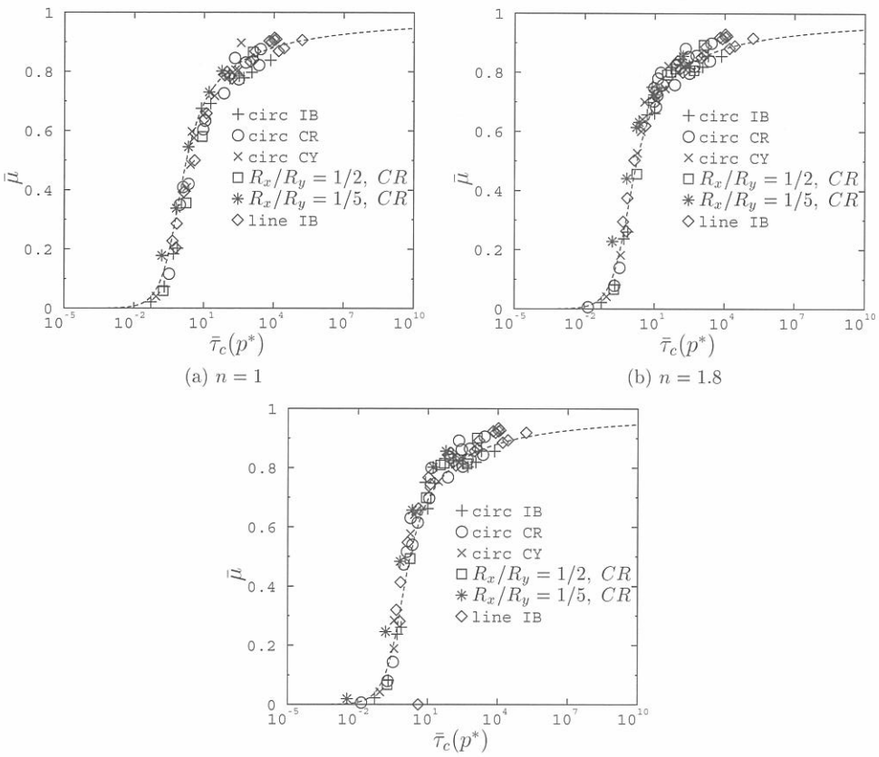

(a) $n = 1$ (b) $n = 1.8$

(c) Gecim & Winer

Figure 4.6: Computed reduced friction coefficient $\bar{\mu}$ as a function of $\bar{\tau}_c(p^*)$ for the various models. The dotted line is given by Eq. 4.7.

Just as for the circular model the friction data collapses on a single curve when plotted as a function of $\bar{\tau}_c(p^*)$. The shape of the mastercurve differs slightly for each limiting shear stress model. Using $n = 2.8$ to approximate Gecim and Winer's model with the general model, the equation of the mastercurves is given by:

$$\bar{\mu} = \left[1 + \frac{1 + 1/(2n)}{\sinh^{-1}(\bar{\tau}_c(p^*))}\right]^{-1} \tag{4.6}$$

The differences between the mastercurves are however small. The models vary in the rate at which they approach the limiting shear stress but on the scale of the mastercurve where $\bar{\tau}_c$ varies by several orders of magnitude the difference is not significant. For simplicity, Eq. 4.6 can be replaced by a unique relation independent of n:

$$\bar{\mu} = \left[1 + \frac{4/3}{\sinh^{-1}(\bar{\tau}_c(p^*))}\right]^{-1} \tag{4.7}$$

where:

$$\bar{\mu} = \mu \frac{p_H}{\tau_L(p_H)} \quad , \qquad \bar{\tau}_c(p^*) = \frac{\bar{\eta}(p^*)\bar{S}}{H_c} \tag{4.8}$$

$$\bar{S} = \frac{(L/\alpha)^2}{E'\tau_L(p^*)} \quad , \qquad p^* = p_H\left(1 - \chi\frac{p_H/10^9}{1 + p_H/10^9}\right) \tag{4.9}$$

with $\chi = 1/3$ for circular and elliptic contacts and $\chi = 1 - \pi/4$ for line contacts.

By slightly modifying $\bar{\tau}_c$ to account for the difference in the friction generation mechanism compared to the Eyring model, the friction results obtained for all cases with the limiting shear stress models can be represented on a single curve which is accurately approximated by Eq. 4.7. Note that again the shape of the curve reflects the rheological model itself.

4.3 Experimental validation

In the previous section it has been shown that the calculated friction data can be brought together on a single curve when plotted in terms of a characteristic shear stress. In this section, an experimental validation is performed using measured traction curves published in the literature. Two points need to be verified. Firstly, whether the experimental traction data obtained under various conditions follows a single line when plotted as a function of $(\bar{\tau}_c, \bar{\mu})$. Secondly, whether the curve thus found follows Eq. 4.4 or Eq. 4.7.

The experimental validation requires an accurate and independent knowledge of the lubricant characteristics, γ or τ_0, and of the piezo-viscous behaviour. Independent in this context means that the values have not been derived from the tests that are being replicated or from similar tests. In particular, the value of τ_0 is usually derived from the slope of measured traction curves. A prediction of measured traction curve with the Eyring model is meaningless if τ_0 is obtained in this manner. However, the experimental results can still be used to verify whether $\bar{\tau}_c$ brings the various friction results together. On the other hand, the limiting shear stress proportionality constant γ can be obtained independently enabling a full validation of the limiting shear stress mastercurve.

Lubricant	p_H(GPa)	T(°C)	u_m(m/s)	γ	τ_0(MPa)
5P4E	0.6	100	0.5	0.06	2.7
S50	0.8	100	1	0.07	5
HVI650	0.8	100	1	0.028	7
DOP	1.04	90	6.4	0.03	9
DOP	1.27	90	6.4	0.03	10

Table 4.1: Operating conditions of the experiments.

4.3.1 Experiments

The accuracy of the validation depends on the accuracy of γ and of the viscosity. With respect to the viscosity only traction tests under conditions within the range of viscosity measurements have been used. With high-pressure viscometers this corresponds to pressures lower than 1.4 GPa at high-temperatures and lower than 1 GPa at ambient temperatures. The Free Volume (Yasutomi [78]) relation is used to approximate the measured viscosity data. The limiting shear stress proportionality constant γ is known with an accuracy of around 20 to 30 %. This has little influence on the horizontal position of the data points on the $(\bar{\tau}_c, \bar{\mu})$ graph considering that $\bar{\tau}_c$ varies by several orders of magnitude. However, this inaccuracy can result in significant vertical shifts: $\bar{\mu} \sim \mu/\gamma$. It is therefore possible that values of $\bar{\mu}$ larger than 1 are observed.

Traction data: The friction data is read from experiments conducted on two-disc machines reported in the literature. Traction curves were measured for a synthetic polyphenylether 5P4E, a mineral oil HVI 650 and a traction fluid Santotrac 50 (S50) for line contact conditions, see [29] and a di(2-ethylhexyl)phthalate (DOP) for elliptic contact conditions, see [59].

Viscosity: The viscosity should be obtained independently of traction measurements to avoid the need for assumptions regarding the rheological behaviour of the lubricants. Here, data obtained with falling body viscometers is used, see [78] for 5P4E, [8] for HVI 650 and [7] for S50 and DOP. The viscosity at the Hertzian pressure is calculated using the Free Volume relation within the range of the high pressure viscometer i.e. the Free Volume relation is not used to extrapolate values at lower temperatures or higher pressures than actually tested.

Limiting shear stress: For all cases but one the limiting shear stress proportionality constant γ is obtained independently from traction tests. It is taken either from measurements on a constant pressure stress-strain apparatus [5] (5P4E) or from measurements done with a high pressure chamber [41] (HVI 650 and S50). Unfortunately, for the case of DOP no such data is available and a value based on the traction curves has been used.

Eyring stress: The values of τ_0 are read from the $\tau_0 = f(p, T)$ graphs given in [28].

Table 4.1 gives the conditions of the traction tests considered for the different lubricants as well as the values of γ and τ_0.

4.3.2 Validation

The experimental data is plotted in terms of ($\bar{\tau}_c$, $\bar{\mu}$) in Fig. 4.7 for the Eyring model and the limiting shear stress model. In the figure it can be seen that the data indeed groups around a single curve. However whereas the data points for S50, HVI 650 and DOP are relatively close together the results for 5P4E are shifted to the right-hand side of the graphs.

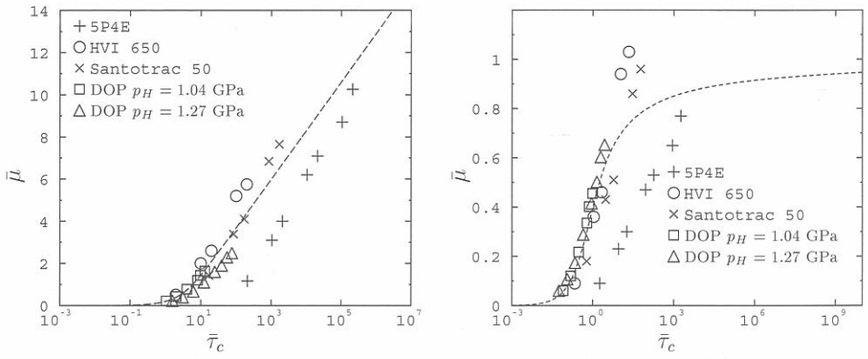

(a) Eyring (b) Limiting shear stress

Figure 4.7: Experimental traction results plotted as a function of ($\bar{\tau}_c$, $\bar{\mu}$). The dotted line is given by Eq. 4.4 (Eyring model) or Eq. 4.7 (limiting shear stress model).

This discrepancy may be explained by thermal effects in the contact. Although the traction experiments were carefully controlled to ensure isothermal conditions a slight increase of temperature δT may already have a large effect on the viscosity and thus on the value of $\bar{\tau}_c$ resulting in a shift of the data points to the left. This is illustrated by Fig. 4.8(a) and (b) in which the same friction results are presented but with $\bar{\tau}_c$ calculated assuming a slightly different temperature, see table 4.2.

Lubricant	p_H(GPa)	T(^{o}C)	δT(Lim)	δT(Eyr)
5P4E	0.6	100	15	7
S50	0.8	100	5	0
HVI650	0.8	100	0	0
DOP	1.04	90	0	0
DOP	1.27	90	0	10

Table 4.2: Temperature increase δT for the Eyring and limiting shear stress models.

The spread in the results is decreased. Another explanation for the case of the limiting shear stress models has been suggested by Bair [9]. It ascribes the shift of the data points

to the right of the curve to shear-thinning effects. These effects do not change the shape of the traction curve but result in a shift to higher shear rates. This corresponds quite well to what is observed in Fig. 4.7(b).

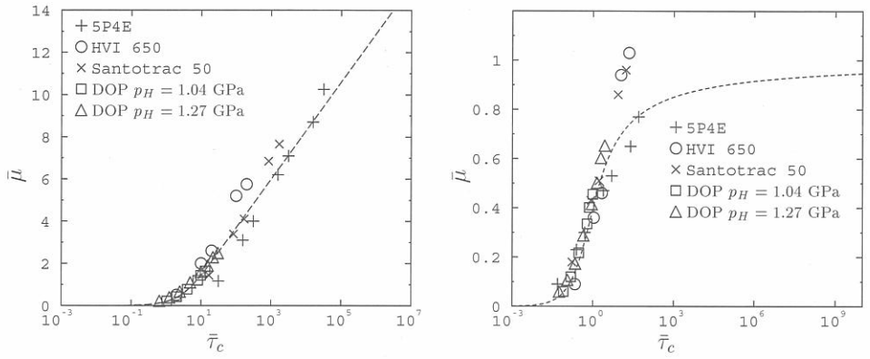

(a) Eyring (b) Limiting shear stress

Figure 4.8: Experimental traction results plotted as a function of ($\bar{\tau}_c$, $\bar{\mu}$) at $T + \delta T$, see Table 4.2. The dotted line is given by Eq. 4.4 (Eyring model) or Eq. 4.7 (limiting shear stress model).

Allowing for a slight temperature increase in the centre of the contact the experimental data confirms that $\bar{\tau}_c$ accurately represents the mechanism of friction generation in sliding EHL contacts. For the limiting shear stress model the use of independent viscosity and limiting shear stress measurements enables a fully independent validation of Eq. 4.7. The good agreement observed strongly supports the limiting shear stress mastercurve as prediction tool for friction in rolling/sliding EHL contacts.

4.4 Comparison of the mastercurves

The friction generation in isothermal contacts can now be mapped simply using Eq. 4.4 and Eq. 4.7 for the two main types of rheological models. The experimental validation has however underlined that Eq. 4.4 predicting the friction coefficient for the Eyring model can hardly be applied in practice as values of τ_0 obtained independently of traction tests are not available. Without entering the discussion about whether that disqualifies the Eyring model as a whole, the presence of one expression for the Eyring model and one for the limiting shear stress model allows for a mathematical comparison of the two models. Realizing that after all both types of model seek to describe the same phenomenon, the objective of this section is to find out whether a relation can be found between the characteristic parameters of both models, τ_0 and τ_L, such that the predictions of Eq. 4.4

The calculated values of τ_0 are quite close to the measured values allowing for some uncertainty in the value of γ. The comparison is less favorable for DOP. The explanation of the discrepancy may be found in the limited range of shear rates considered which fails to cover much of the linear region suitable to measure τ_0.

Summarizing, based on a mathematical analysis an equation relating τ_0 to τ_L has been found. It allows for independent prediction of friction using the Eyring model. Applied to a particular case, the difference between limiting shear stress and Eyring models was shown to be small.

4.5 Conclusions

A large set of friction data has been calculated mapping friction in rolling/sliding EHL contacts for the Eyring and four different limiting shear stress models. The analysis of the data has shown that the friction generation is dominated by the shear of the highly pressurized lubricant film in the centre of the contact. This can be characterized by a characteristic shear stress $\bar{\tau}_c$, calculated at the Hertzian pressure (Eyring model) or at an intermediate pressure (limiting shear stress model). Plotting the friction data in the form $\bar{\mu} = f(\bar{\tau}_c)$ all data points collapse on a single curve with the form of $f(\bar{\tau}_c)$ reflecting the rheological models used.

An experimental validation has been performed for both mastercurves using measured friction data published in the literature. For the Eyring model the verification has been largely hampered by the fact that the Eyring stress τ_0 can not be obtained independently from the traction tests. For the limiting shear stress models a fully independent validation gives a good agreement between the mastercurve and the experimental data.

A comparison between the mastercurves derived for both types of rheological model results in a relation between τ_0 and τ_L (Eq. 4.17) such that both models give the same friction. Using Eq. 4.17 independent friction predictions can now be performed with the Eyring model.

Chapter 5

A simplified approach of frictional heating

In rolling/sliding EHL contacts, the shear stress in the lubricant film is so large that frictional heating will not be negligible. The heat generated in the film may affect the structure of the material close to the surface. It also leads to a reduction of the friction coefficient due to a decrease of the viscosity of the lubricant in the centre of the contact. At large shear rates, the isothermal analysis presented in Chapt. 4 needs to be corrected for thermal effects.

To introduce thermal effects requires an extension of the model with the energy equation to be solved across the film simultaneously with the other equations. It adds a dimension to the problem as a description of the flow across the film is needed, see [51, 68]. To avoid this complexity one could either assume a given temperature profile shape across the film (parabolic for instance [54, 25]) which effectively removes the need for an analysis across the film, or assume given film thickness and pressure profiles and concentrate on solving the energy equation, see [56]. The validity of these simplified approaches relies on an accurate description of the flow of the lubricant. The existence of several rheological models encompassing behaviour ranging from Eyring to slip bands shows that the exact characteristics of the flow are still unclear. The models coexist because each of them can describe the overall frictional behaviour with some accuracy.

In this chapter a simplified thermal model for rolling/sliding EHL contacts is described based on the friction mastercurves derived in the previous chapter and the results of the analysis of thermal effects in dry contacts by Bos [13]. The surface temperature increase and friction coefficient predicted by the simplified model are compared with numerical results obtained with full numerical simulations to check the validity of the assumptions. Subsequently the predictions of the model are validated against measurements of surface temperature increase and of traction curves.

5.1 Model description

As a first approximation the rolling/sliding EHL contact is considered with respect to thermal effects as a dry contact in which the value of the friction coefficient is given by the mastercurves (Eqs. 4.4 and 4.7). Assuming a semi-ellipsoidal heat supply distribution combined with a constant value of the friction coefficient results in a heat distribution close to that obtained in EHL contacts where the shear stress distribution is almost semi-ellipsoidal. By considering the contact as a thermal dry contact it becomes possible to use the function fits derived in [13] giving the maximum surface temperature increase. Note that using a dry contact analysis implies that the surface temperature distributions are equal on each surface.

The temperature increase in the contact influences in a nonlinear way the value of the friction coefficient. Using a parabolic heat distribution across the film and taking advantage of the fact that the mastercurves require the calculation of the shear stress at one point in the contact only, the maximum temperature in the film can be related to the maximum surface temperature calculated with the dry contact analysis. The relation obtained is solved numerically giving the maximum temperature increase at the surface and at mid-film as well as the value of the friction coefficient incorporating thermal effects.

Below some of the results of the dry contact analysis by Bos [13] are recalled. The simplified model for the heat distribution across the lubricant film and its combination with the dry contact results are explained next.

5.1.1 Dry contact results

The local temperature rise of sliding bodies has been studied by Bos [13]. Assuming a heat source distribution which is either uniform or semi-ellipsoidal, he calculated numerically the surface temperature distribution of a semi-infinite body moving along the heat source. For the case of two bodies with conductivity of the same order of magnitude the partition problem is solved assuming the surface temperatures to be equal at each point of the contact area. The closed form function fits derived for the maximum and average temperature increase are recalled below. According to the thermal dry contact theory, the surface temperature increase δT_S is related to the friction coefficient μ by:

$$\delta T_S = c_S \mu \tag{5.1}$$

Where c_S takes into account the thermal properties of the surfaces and their velocities:

$$\delta T_S = c_S \mu = \frac{2\pi}{3} \frac{p_H \sqrt{ab} |u_2 - u_1|}{\sum_i (K_i/\theta_i)} \mu \tag{5.2}$$

with:

$$\theta_i = \left[(\theta_l S(\kappa))^s + \left(\frac{\theta_h}{\sqrt{\kappa Pe_i}} \right)^s \right]^{1/s}, \qquad i = 1, 2 \tag{5.3}$$

where:

$$s = \frac{1}{2} e^{1-\kappa} - \frac{5}{2} \quad \text{and} \quad S(\kappa) = \frac{2}{\pi} \frac{2\sqrt{\kappa}}{1+\kappa} \mathcal{K}\left(\frac{|1-\kappa|}{1+\kappa} \right) \tag{5.4}$$

For $\kappa = 1$, $S(\kappa)$ reduces to unity. θ_h is defined as:

$$\theta_h = \frac{\theta_r + t\theta_s}{1+t} \tag{5.5}$$

with:

$$t = \max\left(0, \frac{-q}{1+q}\right), \qquad q = \text{sign}(u_1 u_2) \min(p, 1/p) \tag{5.6}$$

and $p \equiv \sqrt{Pe_2/Pe_1}$. Note that for velocities in the same direction $\theta_h = \theta_r$.

The values of the θ's depend on the shape of the heat supply distribution and on whether the maximum or average temperature increase is calculated. Here a semi-ellipsoidal heat supply distribution is assumed. In that way the heat supply distribution approximates the distribution that would be obtained for an EHL contact where the pressure distribution is semi-ellipsoidal with a constant friction coefficient. In that case: $\theta_l = 0.375$, $\theta_r = 0.589487$ (maximum) or $\theta_l = 0.281250$, $\theta_r = 0.322991$ (average).

5.1.2 Lubricated contacts

According to the dry contact model the maximum surface temperature increase is related to the friction coefficient by:

$$\delta T_S = c_S \mu = c_S \frac{\tau_r}{p_H} \bar{\mu} \tag{5.7}$$

with $\tau_r = \tau_0$ for the Eyring model and $\tau_L(p_H)$ for the limiting shear stress model.

Due to thermal effects the friction coefficient in Eq. 5.7 does not take its isothermal value but a lower value. To calculate the thermal friction coefficient the temperature increase in the middle of the lubricant film, δT_l, needs to be known. If the mastercurves Eq. 4.4 or Eq. 4.7 are used to calculate $\bar{\mu}$ then the temperature increase needs only to be known at the centre of the contact. Assuming that at $x = y = 0$ and $z = h/2$ the temperature increase is δT_l then Eq. 5.7 becomes:

$$\delta T_S = c_S \frac{\tau_r}{p_H} \bar{\mu}(T_0 + \delta T_l) \tag{5.8}$$

Assuming that the heat generation is uniform in the film volume and recalling that the surface temperatures are equal then the profile of the temperature increase across the film is parabolic and:

$$\delta T_l = \delta T_S + \frac{q''' h^2}{8K_l} \tag{5.9}$$

Where q''' is the heat generated by a unit volume. For a circular contact:

$$q''' = \frac{(u_2 - u_1)f}{\pi a^2 h}\mu \tag{5.10}$$

Using $\mu = \bar{\mu}(\tau_r/p_H)$ and expressing f as a function of p_H and a, Eq. 5.9 can be rewritten as:

$$\delta T_l = \delta T_S + c_l \frac{\tau_r}{p_H}\bar{\mu}(T_0 + \delta T_l) \qquad \text{with:} \qquad c_l = \frac{p_H h(u_2 - u_1)}{12K_l} \tag{5.11}$$

Introducing Eq. 5.8 in Eq. 5.11 results in an equation for the maximum temperature increase in the lubricant film:

$$\delta T_l = \frac{\tau_r}{p_H}(c_S + c_l)\bar{\mu}(T_0 + \delta T_l) \tag{5.12}$$

The temperature increase influences the value of the friction coefficient through a decrease of the viscosity and a change of the value of τ_r. The reduced friction coefficient $\bar{\mu}(T_0+\delta T_l)$ is given by:

$$\bar{\mu}(T_0 + \delta T_l) = f\left(\frac{S(L/\alpha)^2}{H_c E'}\frac{\bar{\eta}(T_0 + \delta T_l)}{\tau_r(T_0 + \delta T_l)}\right) \tag{5.13}$$

where f is given by Eq. 4.4 and Eq. 4.7 for the Eyring and limiting shear stress models respectively.

The viscosity is assumed to vary with temperature according to $\bar{\eta}(T_0+\delta T_l) = \bar{\eta}(T_0) f_\eta(\delta T_l)$. $f_\eta(\delta T_l)$ may take several forms. The simplest relation was given by Barus and reads:

$$f_\eta(\delta T_l) = e^{-\beta \delta T_l} \tag{5.14}$$

Another relation commonly used is that of Vogel:

$$f_\eta(\delta T_l) = \exp\left(\frac{-\beta_1 \delta T_l}{1 + \beta_2 \delta T_l}\right) \tag{5.15}$$

For the cases considered in this work the differences between both models are negligible. In what follows the dependence of viscosity on temperature follows Barus' relation.

The variation of the characteristic shear stress with temperature is quite unclear. Just as for the viscosity it is assumed that $\tau_r(T_0 + \delta T_l) = \tau_r(T_0) f_\tau(\delta T_l)$. For the Eyring model, Evans and Johnson [28] showed that τ_0 varies roughly linearly with temperature. For one oil it was found to decrease with temperature whereas for two others it increased. Let $f_\tau(\delta T_l)$ now be given by:

$$f_\tau(\delta T_l) = 1 - \frac{\omega \delta T_l}{\tau_0(T_0)} \tag{5.16}$$

where ω may be positive or negative.

For the limiting shear stress, the few measurements available suggest that γ, the limiting shear stress pressure dependency coefficient, decreases roughly linearly with pressure [5] [41]. At some point however the rate of decrease of γ with δT has to slow down to prevent meaningless negative values. The following relation is used:

$$\gamma = \gamma_r \exp(-\omega(T + 273)) \tag{5.17}$$

where γ_r is a reference value, see Appendix, and T is given in °C. The fit of Eq. 5.17 with the experimental values is also shown in the Appendix. Given the value of $\gamma = \gamma_0$ at $T = T_0$, the value at $T_0 + \delta T_l$ is given by: $\gamma(T_0 + \delta T_l) = \gamma_0 f_\tau(\delta T_l)$ with:

$$f_\tau(\delta T_l) = \exp(-\omega \delta T_l) \tag{5.18}$$

Defining:

$$\bar{\tau}_c(T_0) = \frac{S(L/\alpha)^2 \bar{\eta}(T_0)}{H_c E' \tau_r(T_0)} \tag{5.19}$$

Eq. 5.12 reads for the Eyring model:

$$\delta T_l = (c_S + c_l)\frac{\tau_0}{p_H}\left(1 - \frac{\omega \delta T_l}{\tau_0(T_0)}\right)\sinh^{-1}\left(\frac{\bar{\tau}_c(T_0)}{5}\frac{\exp(-\beta \delta T_l)}{1 - \dfrac{\omega \delta T_l}{\tau_0(T_0)}}\right) \tag{5.20}$$

and for the limiting shear stress model:

$$\delta T_l = (c_s + c_l)\frac{\tau_L}{p_H}\exp(-\omega \delta T_l)\left[1 + \frac{4/3}{\sinh^{-1}\left(\bar{\tau}_c(T_0)\dfrac{\exp(-\beta \delta T_l)}{\exp(-\omega \delta T_l)}\right)}\right]^{-1} \tag{5.21}$$

Eqs. 5.20 and 5.21 can be solved numerically without difficulties. Once δT_l is calculated the corrected value of the friction coefficient simply follows from $\bar{\mu}(T_0 + \delta T_l)$. The maximum surface temperature increase δT_S is given by Eq. 5.8.

5.2 Numerical validation

The model described above is based on various simplifying assumptions. To check that the assumptions are valid, the results of the model are compared to numerical data obtained using a more complex model, see Kim et al. [52]. The complex model consists of a full numerical solver incorporating both non-Newtonian effects (Eyring model) and the energy equation. The temperature distribution across the film is however assumed to be parabolic such that no resolution in this direction is needed.

The complex model has been used in [52] to predict the surface temperature increase in a pure sliding steel ball/sapphire disc contact and traction curves in a steel ball/steel disc configuration. The results shown here are taken from Fig. 1, 5 and 6 of [52]. The predictions of the simplified model are compared in both cases to the results of the complex model.

Free Volume							
η_g	T_{g0}	A_1	A_2(GPa^{-1})	B_1	B_2(GPa^{-1})	C_1	C_2
10^7	-30.4	309.1	0.3064	0.2186	29.99	10.264	27.04

Roelands			
η_0	α(GPa^{-1})	z_R	β
0.14	22.9	0.5885	0.075

	Steel ball	Sapphire disc	Lubricant
Density(kg/m^3)	7850	3850	884
Thermal conductivity(W m/K)	47	36.7	0.125
Specific heat(J/kg K)	460	800	2100

Table 5.1: Lubricant characteristics and thermal properties of the steel ball and sapphire disc.

Table 5.1 gives the lubricant characteristics and the thermal properties of the steel ball and the sapphire disc. For the surface temperature increase calculations both the Free Volume and the Roelands piezo-viscosity relation are used whereas for the calculation of the traction curves only the Roelands relation is considered. The Eyring model is used assuming an Eyring stress value independent of temperature: $\tau_0 = 3.3$ MPa.

The maximum surface temperature increase obtained for both models is listed in Table 5.2. In this table the subscript $_R$ means that Roelands' relation was used whereas the subscript $_F$ indicates that the Free Volume relation (Yasutomi) was used. The result of the full numerical simulations are indicated by the reference [52]. Two sets of results are given for the simplified model. One obtained using $\tau_0 = 3.3$ MPa, the other using $\tau_0 = 3.8$ MPa. The agreement between the models is very good. For the largest velocity values considered the simplified model predicts a slightly larger temperature increase than the

Lubricant	T_0(°C)	R_x(m)	E'(GPa)	S
HVI650	60	0.0127	286	2

p_H(GPa)	0.88				1.02				1.2			
u_m(m/s)	0.25	0.5	0.75	1	0.25	0.5	0.75	1	0.25	0.5	0.75	1
δT_R [52]	12	18.5	23	26	16	24	29	31	22	31	37	41
δT_R	12	18.8	23.4	26.5	15.5	23.9	29.5	33.3	20.3	30.8	37.6	42.3
δT_R(3.8 MPa)	13.3	20.5	25.2	28.2	17.2	26.2	31.8	35.5	22.5	33.7	40.6	45.1
δT_F [52]	12.5	18.5	21	23	16	22.5	26	28.5	21	30	34	36
δT_F	12.3	18.5	22.2	24.7	26	23.5	28.1	31.1	20.9	30.2	35.8	39.5
δT_F(3.8 MPa)	13.5	19.8	23.5	25.8	17.6	25.3	29.8	32.6	22.9	32.4	38	41.5

Table 5.2: Comparison of the surface temperature increase predicted by the complex model [52] and by the simplified model. $\beta = 0.124$, 0.14 and 0.162 for $p_H = 0.88$, 1.02 and 1.2 GPa respectively.

complex model. At lower velocity values the agreement is remarkably good. In all cases the differences are lower than 10 %.

The predicted traction curves are shown in Fig. 5.1(a) for one load and three different values of the velocity and in Fig. 5.1(b) for one velocity and three values of the load.

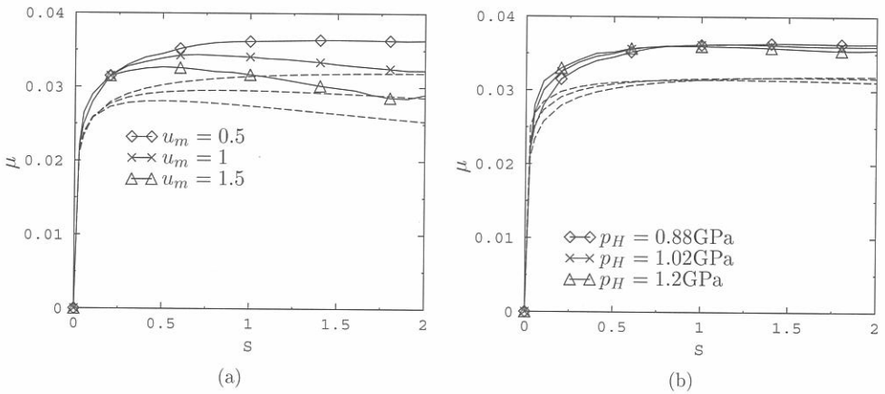

Figure 5.1: Comparison of traction curves predicted by Kim et al. [52] (plain lines) and by the simplified model (dashed lines). Left: $p_H = 0.88$ GPa; right: $u_m = 0.5$ m/s. $\tau_0 = 3.3$ MPa.

Fig. 5.1 shows that the traction predicted with the simplified model is lower than with the complex model but that the rate of decrease of μ due to thermal effects is very similar. The traction curves obtained with the simplified model appear to be shifted slightly

downwards compared to the traction curves given by the complex model. There is a difference at very low slip values already, see Fig. 5.1(a) for instance, for which thermal effects are negligible. This implies that the isothermal predictions of the mastercurve are not correct. To compare only the thermal effects predicted by both models, the isothermal predictions should match. A good agreement of both models at low slip values is achieved by changing slightly the value of τ_0 used in the mastercurve from 3.3 to 3.8 MPa. Note that the resulting maximum surface temperature increase remains close to that obtained with the complex model, see Table 5.2. In that case the thermal effects predicted by the simplified model compare well with the prediction of the complex model, see Fig. 5.2.

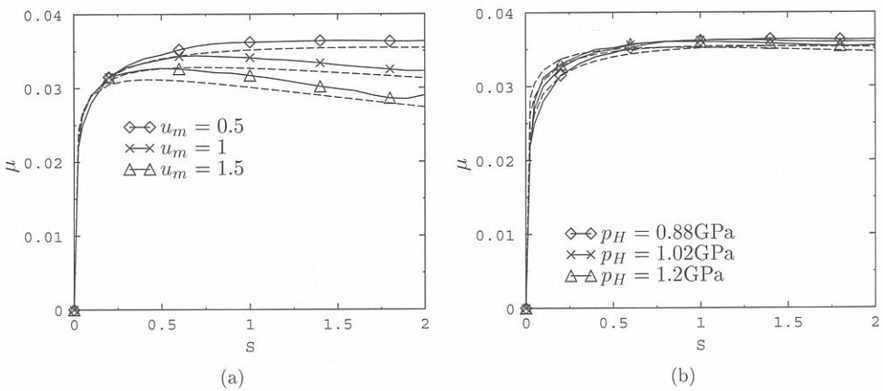

Figure 5.2: Comparison of traction curves predicted by Kim et al. [52] (plain lines) and by the simplified model (dashed lines). Left: $p_H = 0.88$ GPa; right: $u_m = 0.5$ m/s. $\tau_0 = 3.8$ MPa.

The good agreement between the surface temperature increase predicted with the simplified model and the complex model and between the traction curves shows that the assumptions made to derive the simplified model are justified. With almost no loss of accuracy the effect of frictional heating can now be predicted by solving a simple equation.

5.3 Experimental validation

The predictions of the model: the maximum surface temperature increase and the friction coefficient, are now compared to experimental data. The limiting shear stress mastercurve is used to ensure an independent validation.

5.3.1 Lubricant parameters

Just as in Sect. 4.3 for the experimental validation of the friction mastercurves, great care is taken to ensure an independent verification. This implies that the lubricant characteristics must be known independently and accurately. The choice from measurements published in the literature is therefore restricted to lubricant and operating conditions for which the viscosity $\bar{\eta}(p_H, T_0)$ and the pressure-limiting shear stress proportionality constant γ are known.

Viscosity η: The Free Volume model [78] is used to describe the piezo-viscous effects. The parameters of the model are obtained from viscosity pressure measurements with falling body viscometers, see [78] for a naphthenic oil N1, [8] for HVI 650 and [7] for Santotrac 50. The values of the parameters are listed in the Appendix.

Temperature-viscosity coefficient β: The temperature viscosity coefficient β is obtained by averaging $1/\eta(\partial\eta/\partial T)$ over a range of δT between 10 and 100°C under the conditions considered in the tests.

Pressure-limiting shear stress coefficient γ: γ has been measured for N1 in the range $25 \leq T \leq 67$°C using a constant pressure stress-strain apparatus, see [5]. Values of γ at ambient temperature $T \leq 40$°C have also been obtained on the same apparatus for HVI 650 and Santotrac 50. For measurements at higher temperatures, up to 100°C see [41] where a high pressure chamber has been used.

Temperature-limiting shear stress coefficient ω: The data available for γ at different temperatures, see above, is curvefitted using Eq. 5.17. The curvefits are shown in the Appendix.

5.3.2 Surface temperature increase

The maximum surface temperature increase predicted by Eq. 5.21 is compared to experimental measurements published in the literature [61, 18, 31, 36]. In the experiments the temperature is measured at the surface of a steel ball pressed against a sapphire disk by infrared spectroscopy. For further details the reader is referred to [61]. The maximum surface temperature increase is extracted from the temperature profiles measured in this way and compared to the results of Eq. 5.21.

The list of lubricants and operating conditions considered is given in tables 5.3, 5.4 and 5.5 together with the comparison of measured and calculated maximum surface temperatures δT_m and δT_c respectively. For Santotrac 50 and HVI 650 two values of δT_c are mentioned. The mention of δT_c indicates results from calculations performed using γ_0 given by Eq. 5.18. Whereas $\delta T_c(1.3\gamma_0)$ or $\delta T_c(1.5\gamma_0)$ indicate that the surface temperature increase have been computed using 1.3 or 1.5 times this value of γ_0. The modified values reflect the fact that the values of coefficient of friction measured during a traction curve are for those lubricants higher than the limiting shear stress values obtained from out of contact measurements. For instance Evans and Johnson [29] report friction coefficient values

Nagaraj et al. [61]						
Lubricant	p_H(GPa)	T(^{o}C)	R_x(mm)	γ_0	ω	β
N1	1.02	80	15.9	0.0845	0.00742	0.034

S	2				
u_m(m/s)	0.175	0.35	0.70	1.27	2.54
δT_m	38	58	78	89	95
δT_c	26.4	40.1	56.9	73.5	94.9

S	0.12	0.4	0.6	1.04	1.3	1.5	2
u_m(m/s)	1						
δT_m	7	12	23	38	39	47	65
δT_c	10.9	23.8	29.6	38.5	42.5	45.1	66.6

S	-0.12	-0.4	-0.9	-1.52	-2
u_m(m/s)	1				
δT_m	11	20	31	50	89
δT_c	10.9	23.8	36	45.4	70.9

Glovnea and Spikes [31]						
Lubricant	p_H(GPa)	T(^{o}C)	R_x(mm)	γ_0	ω	β
Santotrac 50	1.11	60	12.5	0.112	0.0063	0.166

S	2
u_m(m/s)	1
δT_m	43
δT_c	47.5
$\delta T_c(1.3\gamma_0)$	56.5

Grieve and Spikes [36]						
Lubricant	p_H(GPa)	T(^{o}C)	R_x(mm)	γ_0	ω	β
HVI 650	1.17	80	17.9	0.0304	0.00662	0.116

S	1.33	1	0.8	0.67	0.57	0.5
u_m(m/s)	0.3	0.4	0.5	0.6	0.7	0.8
δT_m	13	10	10	9	9	9
δT_c	11.8	11.8	11.8	11.8	11.7	11.7
$\delta T_c(1.5\gamma_0)$	16.9	16.8	16.8	16.8	16.6	16.6

Lubricant	p_H(GPa)	T(^{o}C)	R_x(mm)	γ_0	ω	β
HVI 650	1.33	80	9.5	0.0304	0.00662	0.13

S	2
u_m(m/s)	0.2
δT_m	17
δT_c	12.1
$\delta T_c(1.5\gamma_0)$	17.3

Table 5.3: Comparison of measured and calculated maximum surface temperature rises (1).

higher than 0.065 at 40^{o}C and p_H = 1.57 GPa while at this temperature out of contact limiting shear stress measurements give a value of γ of 0.036 [41] (0.046 at 26^{o}C [3]).

Cann and Spikes [18]						
Lubricant	p_H(GPa)	T(^{o}C)	R_x(mm)	γ_0	ω	β
Santotrac 50	0.88	40	12.7	0.0974	0.0063	0.24

S	2		
u_m(m/s)	0.25	0.5	1
δT_m	33	46	62
δT_c	26	39	53.7
$\delta T_c(1.3\gamma_0)$	32	46.7	61.3

Lubricant	p_H(GPa)	T(^{o}C)	R_x(mm)	γ_0	ω	β
Santotrac 50	1.02	40	12.7	0.0974	0.0063	0.242

S	2		
u_m(m/s)	0.25	0.5	1
δT_m	42	62	86
δT_c	32.5	47.6	63.6
$\delta T_c(1.3\gamma_0)$	39.7	56.2	71.2

Lubricant	p_H(GPa)	T(^{o}C)	R_x(mm)	γ_0	ω	β
Santotrac 50	1.2	40	12.7	0.0974	0.0063	0.222

S	2		
u_m(m/s)	0.25	0.5	1
δT_m	58	88	114
δT_c	41	58.4	76.1
$\delta T_c(1.3\gamma_0)$	49.6	68.2	84.3

Lubricant	p_H(GPa)	T(^{o}C)	R_x(mm)	γ_0	ω	β
HVI 650	0.88	60	12.7	0.0347	0.00662	0.124

S	2			
u_m(m/s)	0.25	0.5	0.75	1
δT_m	14	21	24	28
δT_c	9.68	15.5	19.8	23.3
$\delta T_c(1.5\gamma_0)$	13.9	21.7	27.2	31.6

Lubricant	p_H(GPa)	T(^{o}C)	R_x(mm)	γ_0	ω	β
HVI 650	1.02	60	12.7	0.0347	0.00662	0.14

S	2			
u_m(m/s)	0.25	0.5	0.75	1
δT_m	22	31	36	38
δT_c	12.6	19.8	25	29.1
$\delta T_c(1.5\gamma_0)$	17.9	27.4	34	38.9

Table 5.4: Comparison of measured and calculated maximum surface temperature rises (2).

Cann and Spikes [18]						
S	2					
Lubricant	p_H(GPa)	T(°C)	R_x(mm)	γ_0	ω	β
HVI 650	1.2	60	12.7	0.0347	0.00662	0.162
u_m(m/s)	0.25	0.5	0.75	1		
δT_m	29	42	48	53		
δT_c	16.6	25.5	31.7	36.6		
$\delta T_c(1.5\gamma_0)$	23.5	34.9	42.5	48.1		

Table 5.5: Comparison of measured and calculated maximum surface temperature rises (3).

In all cases the order of magnitude is correctly predicted and in most cases the prediction is actually quite close to the measured value. The maximum difference is around 30 %. It shows that the assumption of a semi-ellipsoidal heat distribution and constant friction coefficient is justified.

Note that in most cases the slide/roll ratio is large and therefore the friction coefficient close to its maximum value. In this respect the comparison with the experimental results performed above is only a validation of the approach chosen. It is hardly a validation of the limiting shear stress mastercurve itself. To do this the effects of frictional heating on the shape of the traction curve need to be analyzed. In the next section measured traction curves showing thermal effects at high slip values are compared to the prediction obtained using the limiting shear stress mastercurve.

5.3.3 Traction curves

Traction curves were measured to validate the effect of temperature increase in the contact on the friction coefficient predicted by the model. The experimental set-up consists of a ball-on-disc apparatus, see Fig. 5.3, in which a steel ball of radius $R = 0.02$ m is pressed against a steel disc. The lubricant used is HVI 650. The conditions of the test are given in Table 5.6.

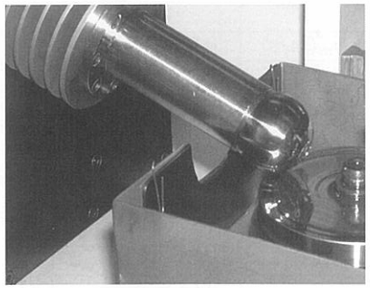

Figure 5.3: Ball-on-disc apparatus used for the experimental validation.

The comparison of the predicted surface temperature increase with experimental data in the previous section has shown that the value of the limiting shear stress proportionality constant γ should be taken higher than that given by out of contact experiments. A correction factor of 1.5 times is used, see Table 5.6.

T(°C)	p_H(GPa)	u_m(m/s)	γ
60	0.662, 0.834	0.75, 1.25	0.0521
90	0.834	1.6, 3.35	0.0427

Table 5.6: Operating conditions of the traction measurements.

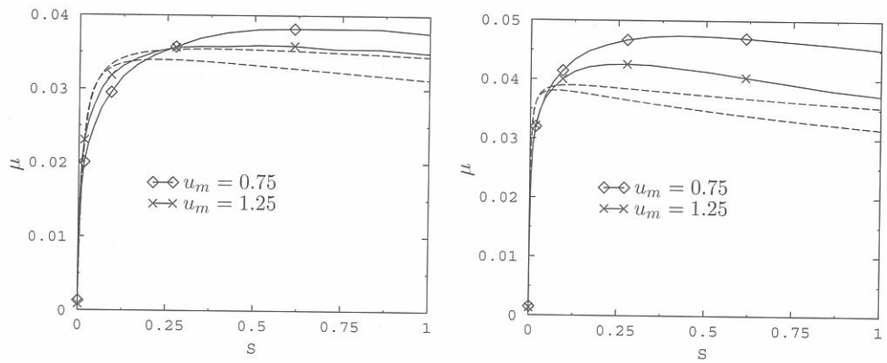

(a) $T_0 = 60°C$, $p_H = 0.662$ GPa

(b) $T_0 = 60°C$, $p_H = 0.834$ GPa

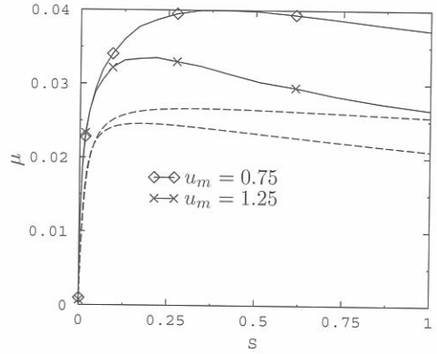

(c) $T_0 = 90°C$, $p_H = 0.834$ GPa

Figure 5.4: Comparison of measured (plain lines) and predicted (dashed lines) traction curves. Limiting shear stress model.

The predicted and measured traction curves are shown in Fig. 5.4. Consider Fig. 5.4(a) and (b) obtained at $T = 60°C$. In both cases the prediction is lower than the measurements for $S \geq 0.25$. For $S \leq 0.25$ the opposite happens. In this region thermal effects are very small which implies that the limiting shear stress mastercurve does not correctly represent the isothermal frictional behaviour at low slip values. At $T = 90°C$ the calculated friction coefficient is very low compared to the measurements, see Fig. 5.4(c).

Summarizing the agreement is quite poor between the calculated and measured traction curves. However the behaviour observed at low slip values may indicate that the limiting shear stress model is not appropriate for characterizing the lubricant rheological behaviour. The large discrepancies at $T = 90^oC$ on the other hand may result from incorrect viscosity and/or limiting shear stress input data.

A further verification is therefore performed with the Eyring model. Using Eq. 4.17 a value of the Eyring stress τ_0 can be found corresponding to the limiting shear stress value, see Sect. 4.4. Recall that the value of τ_0 depends on the slip. Fig. 5.5 shows the value of τ_0 corresponding to τ_L for the different cases as a function of $\bar{\tau}_c$. The rule defined in Sect. 4.4 for the choice of τ_0 is applied here: the value of τ_0 is chosen at $\bar{\tau}_c = 1$. This implies that in the nonlinear region of the traction curves, before the curve levels off towards its limiting value in the case of the limiting shear stress, both models predict very similar values of the friction coefficient.

For all conditions considered here this corresponds to $\tau_0 = 5$ MPa. Because the variation of τ_0 with temperature is unknown, τ_0 is assumed to be independent of the temperature in the calculations. The predicted traction curves are shown in Fig. 5.6. The agreement is very good for $T = 60^oC$: for the entire range of slip values including $S \leq 0.25$ the predicted and measured traction curves are quite close together. For $T = 90^oC$ the discrepancy remains. It seems that using the Eyring mastercurve in the simplified thermal model results in an accurate estimation of the effect of frictional heating on the friction coefficient.

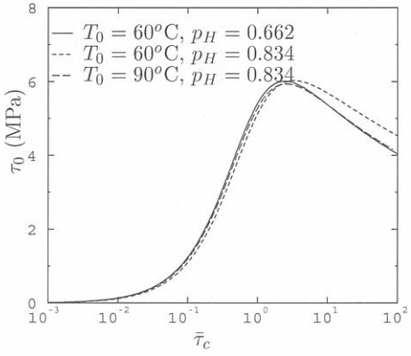

Figure 5.5: Eyring stress τ_0 derived from the limiting shear stress value using Eq. 4.17.

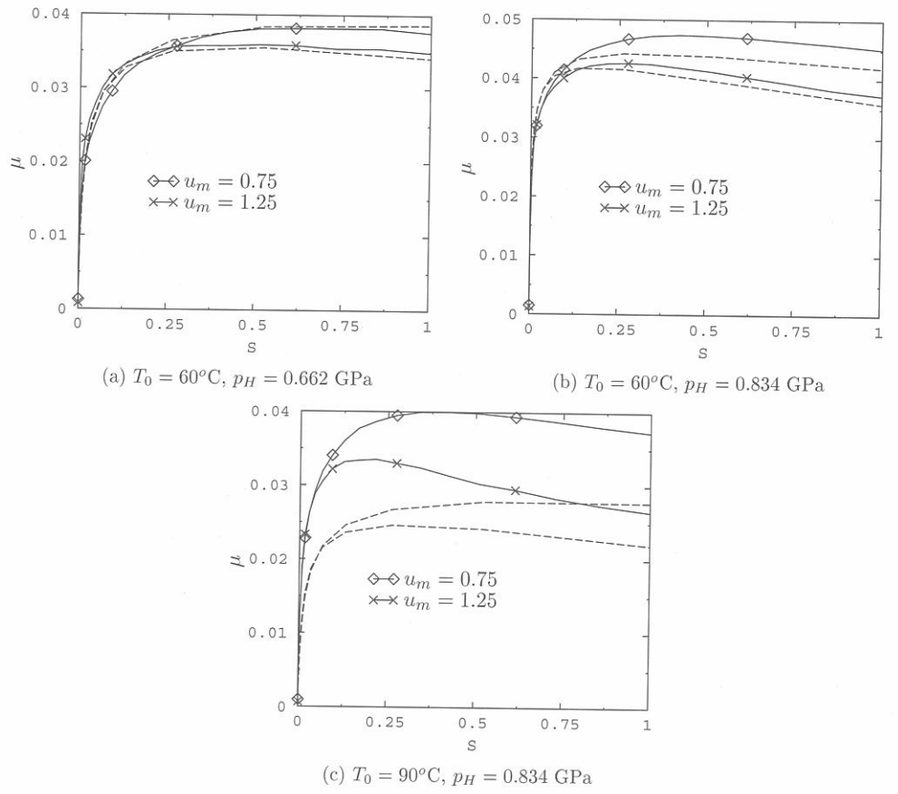

(a) $T_0 = 60^oC$, $p_H = 0.662$ GPa

(b) $T_0 = 60^oC$, $p_H = 0.834$ GPa

(c) $T_0 = 90^oC$, $p_H = 0.834$ GPa

Figure 5.6: Comparison of measured (plain lines) and predicted (dashed lines) traction curves. Eyring model, $\tau_0 = 5$ MPa.

5.4 Conclusions

The thermal effects caused by frictional heating in rolling/sliding EHL contacts can be estimated with a simplified model in which the thermal dry contact analysis of Bos [13] and the friction mastercurves established in Chapt. 4 are combined. The maximum lubricant temperature increase can be easily calculated by solving numerically Eq. 5.20 or Eq. 5.21 for the Eyring model and the limiting shear stress model respectively. The corrected friction coefficient is subsequently obtained by using the isothermal mastercurves taking into account the temperature increase. A relation giving the maximum surface

temperature increase is also given.

The model has been compared to data obtained using full numerical calculations, see [52], to check the validity of the simplifications. The predictions of the model show a good agreement with the numerical data.

Finally an experimental verification has been performed. The predicted temperature increase compared quite well with infrared measurements published in the literature. The prediction of the effect of frictional heating on the traction curves proved to be quite accurate at intermediate temperatures. At high temperatures the discrepancy observed between predicted and measured friction coefficient may possibly be attributed to inaccurate lubricant characteristics.

The simplified approach to frictional heating described in this chapter gives an accurate prediction of thermal effects in rolling/sliding thermal contacts. In this way the validity and usefulness of the mastercurves can be extended to much larger shear rates.

Chapter 6

Friction in rough contacts

The mechanism of friction generation in EHL contacts between perfectly smooth surfaces has been described in Chapt. 4. However in reality the contacting surfaces are never perfectly smooth and even under full film lubrication the surface roughness will influence the level of friction experienced in the application. This chapter presents a systematic study of the variations of the coefficient of friction $\delta\bar{\mu}/\bar{\mu}$ due to longitudinal roughness. At first the influence of a single harmonic component is considered. The relative variation of friction $\delta\bar{\mu}/\bar{\mu}$ is computed for a wide range of operating conditions and waviness geometries. From the results a general prediction formula is derived based on an out-of-contact description of the waviness and a newly derived parameter characterizing the response of the contact to pressure variations. The analysis is then repeated for a combination of two waves and a combination formula is established allowing the representation of complex roughness geometries as an equivalent wave. The validity of the combination formula is verified numerically by comparing its prediction with the results of full numerical simulations for the case of a real rough profile.

6.1 Operating conditions, lubricant characteristics

The presence of roughness on one of the contacting surfaces causes relative variations $\delta\bar{\mu}/\bar{\mu}$ on the friction level $\bar{\mu}$ that would be obtained with perfectly smooth surfaces. The magnitude of these variations depends on the operating conditions, on the lubricant characteristics and on the roughness geometry. In particular it depends on the response of the shear stress to viscosity fluctuations induced by the pressure variations caused by the roughness. As in Chapt. 4, the various influences are investigated by means of six cases. However the cases considered are slightly different and correspond to circular contacts only. The influence of the contact geometry is studied later in this chapter. The importance of the piezo-viscous behaviour is reflected in the choice of two cases for each pressure-viscosity relation, see Fig. 6.1. The cases are denoted:

IB1	Circular contact with an incompressible lubricant following Barus' pressure-viscosity relation, $\alpha = 20$ GPa^{-1}.
IB2	Same configuration except that $\alpha = 30$ GPa^{-1}.
CR1	Circular contact with a compressible lubricant following Roelands' pressure-viscosity relation, $\alpha = 20$ GPa^{-1} and $z_R = 0.67$.
CR2	Same configuration but now with $\alpha = 15$ GPa^{-1} and $z_R = 0.87$.
CY1	Circular contact with a compressible lubricant following Yasutomi's pressure-viscosity relation corresponding to Shell TT9 at 40°C ($\alpha = 21.6$ GPa^{-1}), see Appendix.
CY2	Same configuration except that the lubricant now corresponds to HVI 650 at 60°C ($\alpha = 22.9$ GPa^{-1}), see Appendix.

For each case, the operating conditions are varied: $100 \leq M \leq 1000$, $5 \leq L \leq 15$. The slip is varied between 0.1 and 2%. The Eyring stress τ_0 is taken $2 \leq \tau_0 \leq 8$ MPa.

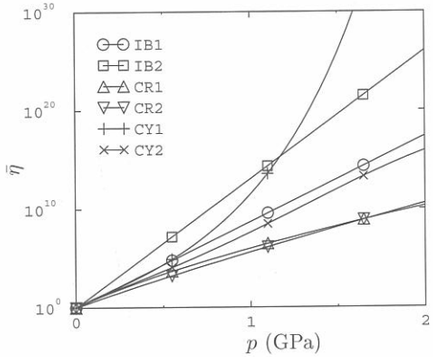

Figure 6.1: Dimensionless viscosity $\bar{\eta}$ as a function of the pressure for the cases considered.

The analysis in this chapter is based on the Eyring model only. The limiting shear stress models lead to predicted pressure profiles and film shapes with physically unrealistic distortions when applied with no-slip boundary conditions as is the case in this work, see Chapt. 3. The introduction of large pressure gradients due to the roughness will aggravate this tendency. The Eyring model on the contrary predicts no such distortions. Moreover calculations of the deformation of wavy surfaces in a rolling/sliding EHL contact using the Eyring model have shown good agreement with experimental measurements, see [73].

6.2 Roughness description

The roughness of the rings and rollers of rolling bearings usually has a complex topography. In general the simulation of such complex roughness distributions adds little to

the understanding of roughness effects. A much more fruitful approach is to describe the roughness as the sum of harmonic components using Fourier decomposition. The effect of a single harmonic component is a problem simple enough to be understood and accurately modeled. Subsequently these effects can be combined to predict the overall variation due to the original complex roughness distribution.

This approach has been very useful in studies of roughness effects on the film thickness in EHL contacts, see for instance [33, 60, 57]. In that case it was shown that the deformation of a rough profile could be computed by adding the deformation of each of its harmonic components. Of course with respect to friction variation the process is non-linear and superposition is not possible. Nevertheless the method is also very useful as will be shown. The analysis starts by studying the effects of single harmonic components followed by a combination of these components.

In this work the roughness is assumed to be longitudinal i.e. the lay of the roughness is aligned with the running direction. It is the type of roughness lay obtained on the rings of rolling bearings after the most common finishing processes. The dimensionless film thickness equation for the case of a single harmonic component on a smooth surface reads:

$$H(X,Y) = -\Delta + \mathcal{S}X^2 + (1-\mathcal{S})Y^2 - \mathcal{A}\cos\left(2\pi(Y/\mathcal{W}+\phi)\right) + \frac{1}{\pi\mathcal{K}}\int\int_S \frac{P(X',Y')\,dX'\,dY'}{\sqrt{\kappa^2(X-X')^2+(Y-Y')^2}} \quad (6.1)$$

The waviness is characterized by its dimensionless amplitude $\mathcal{A}$ and wavelength $\mathcal{W}$ and its relative position to the contact centerline $Y = 0$ by ϕ. Regarding the amplitude it is useful to introduce another dimensionless quantity, the relative amplitude $\bar{\mathcal{A}}$ defined as $\bar{\mathcal{A}} = \mathcal{A}/H_c$ where H_c is the dimensionless smooth central film thickness. The values of $\bar{\mathcal{A}}$ and $\mathcal{W}$ considered in this work are $\bar{\mathcal{A}} = 0.25,\ 0.5\ 0.75$, $\mathcal{W} = 1/10,\ 1/8,\ 1/6\ ,1/4,\ 1/2$.

A typical example of pressure, film thickness and shear stress distributions is given in Fig. 6.2 for case IB1 with $M = 500$, $L = 10$, $S = 0.5\%$ and $\tau_0 = 4$ MPa; $\bar{\mathcal{A}} = 0.5$ and $\mathcal{W} = 1/6$. Fig. 6.2(b) shows that the waviness is not totally deformed in the contact as the sinusoidal variations can still clearly be seen in the central region. Accordingly the pressure and shear stress distributions also exhibit sinusoidal variations.

In real applications it is impossible to know exactly the lateral position of the roughness. However the value of $\delta\bar{\mu}/\bar{\mu}$ depends on this position. For the harmonic components all values of ϕ between 0 and 1/2 will result in different values of $\delta\bar{\mu}/\bar{\mu}$. The influence of roughness on friction can thus be characterized in different ways, by taking the average value of $\delta\bar{\mu}/\bar{\mu}$ for instance or its maximum value. It is chosen here to consider only the maximum value. Indeed, introducing roughness will in most cases result in an increase of the friction coefficient and monitoring $\max(\delta\bar{\mu}/\bar{\mu})$ will thus give an estimation of the worst case.

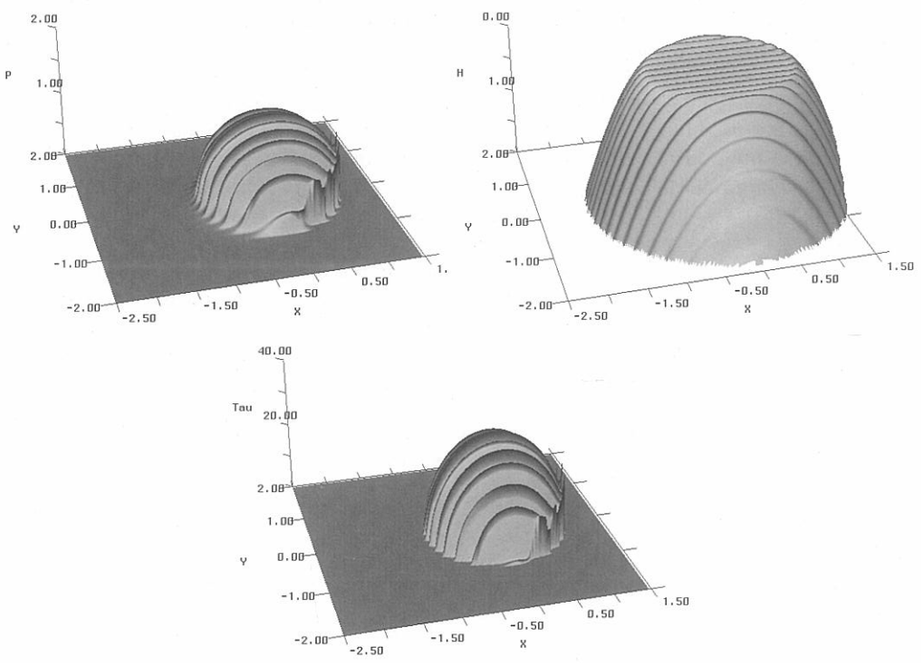

Figure 6.2: Pressure (top left), film thickness (top right), and shear stress distribution (bottom) for IB1: $M = 500$, $L = 10$, $S = 0.5\%$ and $\tau_0 = 4$ MPa; $\bar{\mathcal{A}} = 0.5$ and $\mathcal{W} = 1/6$.

Calculating $\delta\bar{\mu}/\bar{\mu}$ for the entire range of ϕ taking many values is however not practical. As a consequence $\delta\bar{\mu}/\bar{\mu}$ is calculated for $\phi = 0$ and $\phi = 1/2$ only. The larger value is taken to represent the maximum value of $\delta\bar{\mu}/\bar{\mu}$. When real roughness is studied, see Sect. 6.6, more lateral positions are considered. The maximum value of $\delta\bar{\mu}/\bar{\mu}$ will then be given by $\overline{(\delta\bar{\mu}/\bar{\mu})} + 2\sigma$ where $\overline{(\delta\bar{\mu}/\bar{\mu})}$ is the average of the friction variations calculated for each position and σ its standard deviation.

6.3 Numerical analysis

The relative friction variation $\delta\bar{\mu}/\bar{\mu}$ is calculated for the cases IB1 to CY2 and the waviness geometries described in section 6.2. The aim is to derive from the data a general formula giving the friction variation $\delta\bar{\mu}/\bar{\mu}$ as a function of the operating conditions and waviness geometry. To be generally applicable and easy-to-use this relation should have only well-known contact characteristics as input. With respect to the waviness, the relative amplitude $\bar{\mathcal{A}}$ and wavelength $\mathcal{W}$ are the only two variables known a priori.

Alternatively the film thickness variations δH and pressure changes δP caused by the roughness could be mapped enabling the use of δH and δP as parameters. However this approach is invalidated by the manner in which the friction variation is generated in the contact. Consider a circular integration domain S centered on $X = Y = 0$ of dimensionless radius r. The integral of the shear stress variations $\delta\bar{\tau}(r)$ over this domain should be close to $\delta\bar{\mu}$ when r approaches 1. By monitoring the ratio of $\iint_S \delta\bar{\tau}\, dX\, dY$ to $\delta\bar{\mu}$ as a function of r, it is possible to identify which parts of the contact contributes most to $\delta\bar{\mu}$. Fig. 6.3 shows the results of the numerical integration of $\iint_S \delta\bar{\tau}\, dX\, dY$ divided by the friction changes $\delta\bar{\mu}$ calculated over the whole contact in case IB1 for two sets of operating conditions and two wavelengths.

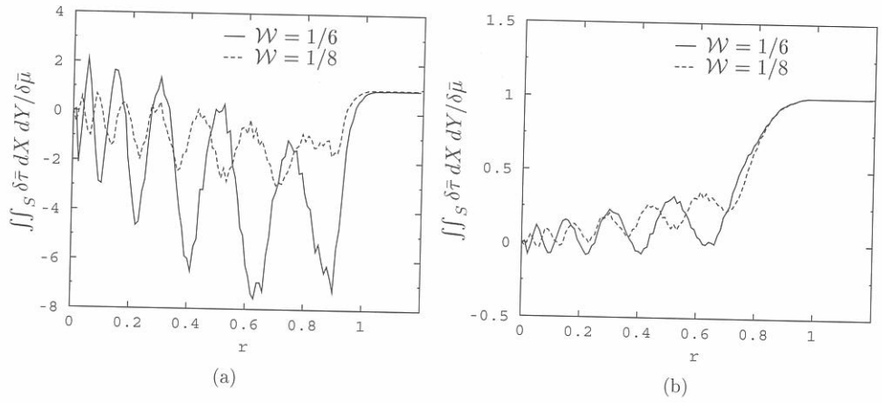

Figure 6.3: Friction variations $\iint_S \delta\bar{\tau}\, dX\, dY/\delta\bar{\mu}$ as a function of the radius r of the integration zone. IB1 (a) $M = 500$, $L = 15$, $S = 0.5\%$ and $\tau_0 = 4$ MPa, (b) $M = 1000$, $L = 5$, $S = 2\%$ and $\tau_0 = 8$ MPa. $\bar{\mathcal{A}} = 0.5$.

The figure shows that the ratio of the integral of the shear stress variations to the overall friction variation $\delta\bar{\mu}$ oscillates for $r \leq 0.8$ reaching its final value just before $r = 1$. The amplitude of the oscillations can reach several times $\delta\bar{\mu}$, see Fig. 6.3(a). There appears to be no pattern in the behaviour of the amplitude of the variations of $\iint_S \delta\bar{\tau}\, dX\, dY/\delta\bar{\mu}$ as a function of r. An accurate determination of $\delta\bar{\mu}$ can therefore only be done when the whole contact is taken into account.

This implies that the friction variation $\delta\bar{\mu}/\bar{\mu}$ can only be related to δH and δP if they are known over most of the contact. This does not appear to be very practical and leaves $\bar{\mathcal{A}}$

and $\mathcal{W}$ as the best parameters to define roughness insofar as a general predictive formula is the goal of the analysis.

6.4 Single wave

The influence of a single longitudinal harmonic waviness on friction is studied first. The relative friction variation $\delta\bar{\mu}/\bar{\mu}$ is calculated for the cases IB1 to CY2, see sect. 6.1.

Consider the maximum friction variation $\delta\bar{\mu}/\bar{\mu}$ caused by a waviness on the upper surface of amplitude $\bar{\mathcal{A}} = 0.5$ and wavelength $\mathcal{W} = 1/6$. In Fig. 6.4 the relative friction variation $\delta\bar{\mu}/\bar{\mu}$ is plotted as a function of the characteristic shear stress defined for smooth contacts $\bar{\tau}_c$ for all six cases.

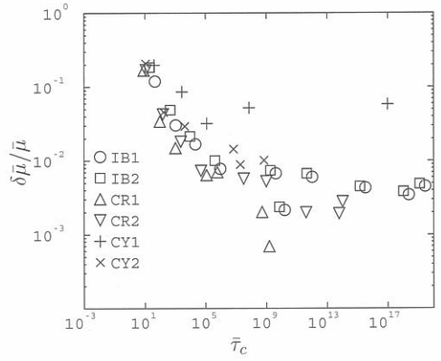

Figure 6.4: Friction variations $\delta\bar{\mu}/\bar{\mu}$ as a function of $\bar{\tau}_c$ for $\bar{\mathcal{A}} = 1/2$ and $\mathcal{W} = 1/6$.

In the figure it can be seen that the general trend is that $\delta\bar{\mu}/\bar{\mu}$ decreases with increasing $\bar{\tau}_c$. However the rate of decrease of $\delta\bar{\mu}/\bar{\mu}$ with $\bar{\tau}_c$ varies. In each individual case the spread can be quite large. IB1 and IB2 show a very similar behaviour: a steep initial decrease followed by a region of slowly decreasing $\delta\bar{\mu}/\bar{\mu}$ for $\bar{\tau}_c \geq 10^9$. CR1 and CR2 are also very similar but compared to the IB cases $\delta\bar{\mu}/\bar{\mu}$ decreases faster with $\bar{\tau}_c$. In case CR1 the rate of decrease is higher than in case CR2. Finally CY1 and CY2 show very different behaviour. The behaviour of CY2 is similar to that shown by the IB cases and it has the same rate of decrease. CY1 is also similar initially but for $\bar{\tau}_c \geq 10^5$ the data points start to stray away from the IB cases and stay at a roughly constant level which is considerably larger than the level of all other cases.

The behaviour shown by the different cases cannot be explained simply by the type of pressure-viscosity relation used: two different pressure-viscosity relations can give very

similar results, see CY2 and the IB cases, whereas very different behaviour can be observed when using the same pressure-viscosity relation, see CY2 and CY1.

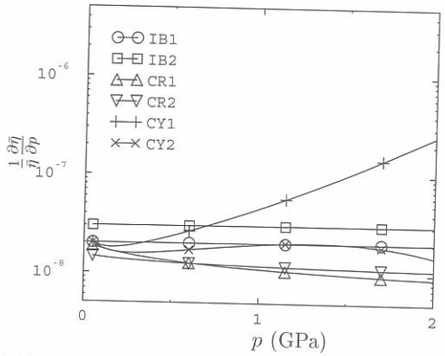

Figure 6.5: $(1/\bar{\eta})(\partial\bar{\eta}/\partial p)$ as a function of the pressure for the cases IB1 to CY2.

The explanation lies in the response of the viscosity to pressure variations. This is illustrated in Fig. 6.5 where $(1/\bar{\eta})(\partial\bar{\eta}/\partial P)$ is plotted as a function of the pressure. Comparing Fig. 6.4 with Fig. 6.5 it can be deduced that there is a clear relation between the ranking of the cases as a function of $(1/\bar{\eta})(\partial\bar{\eta}/\partial P)$ and the rate of decrease of $\delta\bar{\mu}/\bar{\mu}$ with $\bar{\tau}_c$. Take for instance CY1 and CY2. For CY2 the value of $(1/\bar{\eta})(\partial\bar{\eta}/\partial P)$ is very close to that of the IB cases whereas CY1 shows values much higher than that of the IB cases even at low pressures. Correspondingly, on the $\delta\bar{\mu}/\bar{\mu} = f(\bar{\tau}_c)$ graph, CY2 stays near the data points of the IB cases whereas the data points for CY1 are much higher. Similarly, the fact that for the CR cases $(1/\bar{\eta})(\partial\bar{\eta}/\partial P)$ is smaller than for the IB cases is reflected by $\delta\bar{\mu}/\bar{\mu}$ in Fig. 6.4.

If a parameter exists that characterizes the mechanism behind the friction variations due to waviness it should in principle account for this behaviour. To find such a parameter assume for simplicity that the behaviour of $\delta\bar{\mu}/\bar{\mu}$ can be ascribed to what happens in the centre of the contact. Note that strictly this is not allowed because the friction variation depends on the contribution of the whole contact, see Sect. 6.3. Assume also that the influence of the pressure variations on $\delta\bar{\mu}/\bar{\mu}$ is much greater than that of the film thickness variations. Then based on the mastercurve obtained for the smooth contacts the friction coefficient for a rough surface can be approximated by :

$$\bar{\mu}_R = \bar{\mu}(1+\delta P) = \sinh^{-1}(\bar{\tau}_c(1+\delta P)/5) \tag{6.2}$$

To a first order approximation Eq. 6.2 reads:

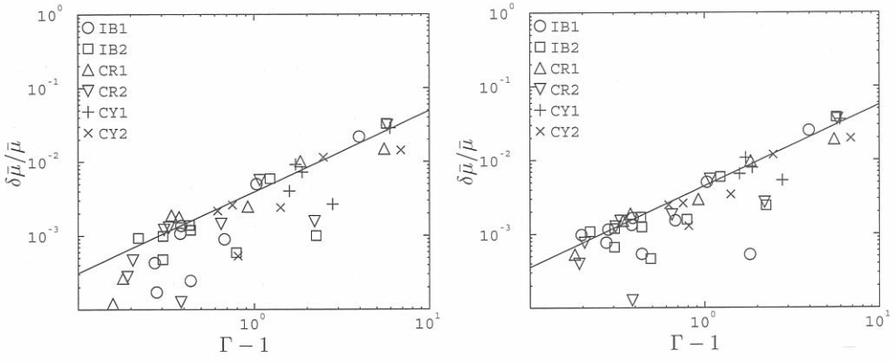

(a) $\bar{\mathcal{A}} = 0.25,\ \mathcal{W} = 1/10$

(b) $\bar{\mathcal{A}} = 0.25,\ \mathcal{W} = 1/8$

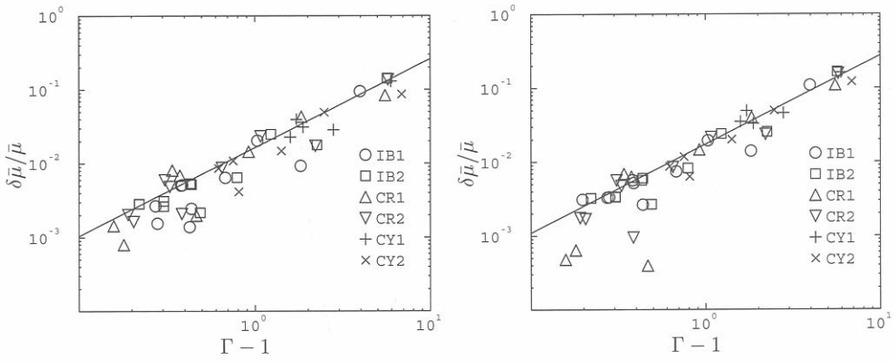

(c) $\bar{\mathcal{A}} = 0.5,\ \mathcal{W} = 1/10$

(d) $\bar{\mathcal{A}} = 0.5,\ \mathcal{W} = 1/8$

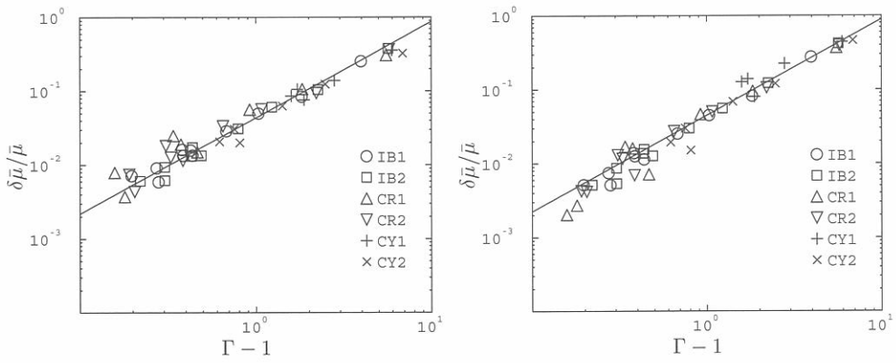

(e) $\bar{\mathcal{A}} = 0.75,\ \mathcal{W} = 1/10$

(f) $\bar{\mathcal{A}} = 0.75,\ \mathcal{W} = 1/8$

Figure 6.7: Friction variations $\delta\bar{\mu}/\bar{\mu}$ as a function of $(\Gamma - 1)$ for varying $\bar{\mathcal{A}}$ and $\mathcal{W}$. Plain line, Eq. 6.8.

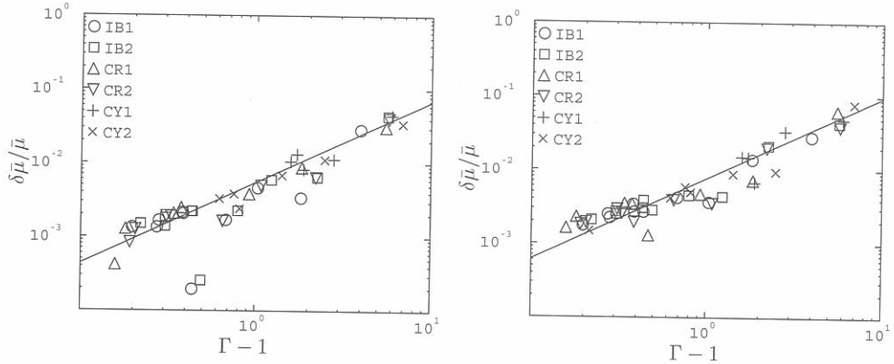

(a) $\bar{\mathcal{A}} = 0.25,\ \mathcal{W} = 1/6$

(b) $\bar{\mathcal{A}} = 0.25,\ \mathcal{W} = 1/4$

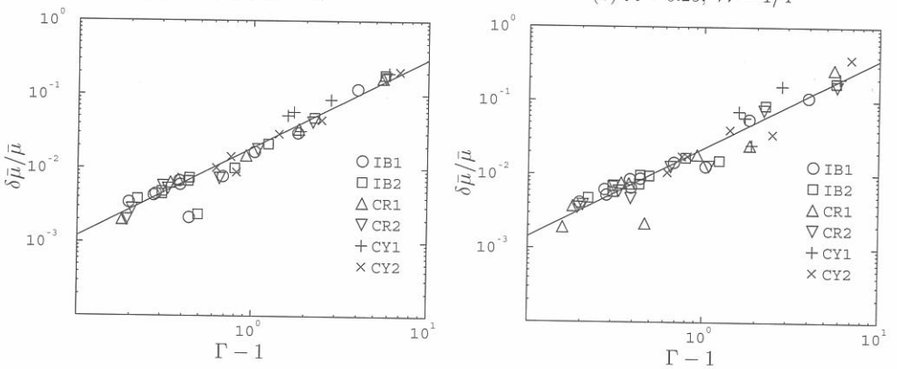

(c) $\bar{\mathcal{A}} = 0.5,\ \mathcal{W} = 1/6$

(d) $\bar{\mathcal{A}} = 0.5,\ \mathcal{W} = 1/4$

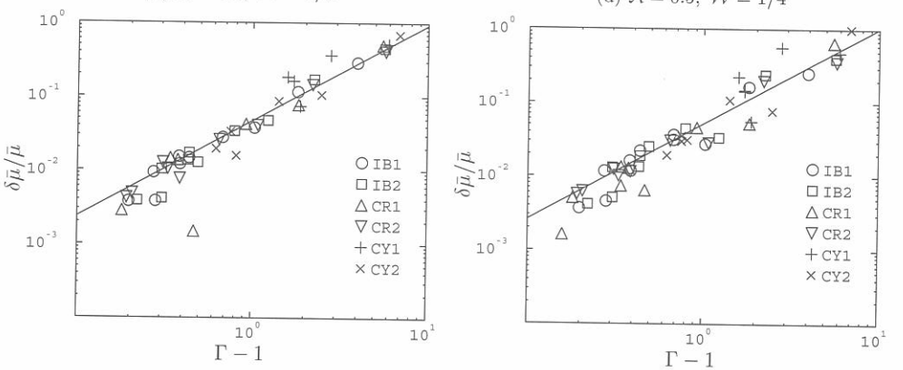

(e) $\bar{\mathcal{A}} = 0.75,\ \mathcal{W} = 1/6$

(f) $\bar{\mathcal{A}} = 0.75,\ \mathcal{W} = 1/4$

Figure 6.8: Friction variations $\delta\bar{\mu}/\bar{\mu}$ as a function of $(\Gamma - 1)$ for varying $\bar{\mathcal{A}}$ and $\mathcal{W}$. Plain line, Eq. 6.8.

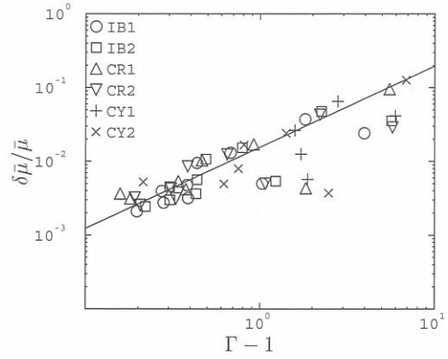

(a) $\bar{A} = 0.25,\ \mathcal{W} = 1/2$

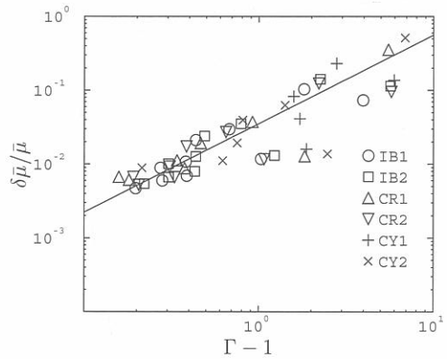

(b) $\bar{A} = 0.5,\ \mathcal{W} = 1/2$

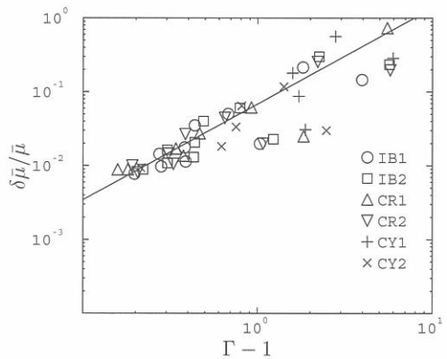

(c) $\bar{A} = 0.75,\ \mathcal{W} = 1/2$

Figure 6.9: Friction variations $\delta\bar{\mu}/\bar{\mu}$ as a function of $(\Gamma - 1)$ for varying $\bar{A}$ and $\mathcal{W}$. Plain line, Eq. 6.8.

For small $(\Gamma - 1)$ values, the calculated $\delta\bar{\mu}/\bar{\mu}$ values for this value of ϕ are found to be larger than those obtained for $\phi = 0$ or $\phi = 1/2$ and the agreement of the data points with Eq. 6.8 is much better.

6.4.1 Elliptic contacts

The validity of Eq. 6.8 is checked for elliptic contacts using a smaller data set. Instead of a full factorial analysis with respect to $\bar{A}$ and $\mathcal{W}$, for each combination $(M, L, \bar{S}, \tau_0)$ only one random pair $(\bar{A}, \mathcal{W})$ is studied. The results are compared to the prediction of Eq. 6.8 in Fig. 6.10(a) for $R_X/R_Y = 1/2$ and in Fig. 6.10(b) for $R_X/R_Y = 1/5$. The first conclusion in both cases is that the results from the calculations and those obtained using Eq. 6.8 are quite close. The spread is quite large but not higher than that observed for the circular contact. The points far away to the bottom left of the curve for low $\delta\bar{\mu}/\bar{\mu}$ can also be found in Fig. 6.7(a-d). Recall that Eq. 6.8 was chosen such that an upper bound to the friction variations is calculated. For low values of $\delta\bar{\mu}/\bar{\mu}$ this sometimes results in a large overestimation of the $\delta\bar{\mu}/\bar{\mu}$.

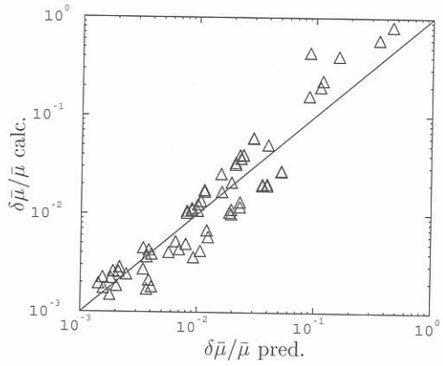

(a)

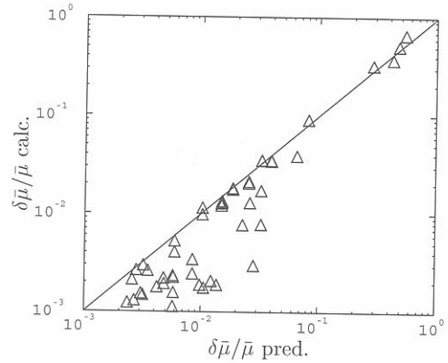

(b)

Figure 6.10: Comparison of friction variations calculated for $R_X/R_Y = 1/2$ (a) or $R_X/R_Y = 1/5$ (b) and Eq. 6.8.

Summarizing, a parameter Γ has been found characterizing the effect of roughness induced pressure variations on the variations of the friction coefficient in EHL contacts. A predictive formula has been derived giving $\delta\bar{\mu}/\bar{\mu}$ as a function of $\bar{A}$, $\mathcal{W}$ and Γ, see Eq. 6.8. The ellipticity enters indirectly through the parameter Γ. At this point its physical meaning remains to be found.

6.5 Two waves

The extension of this analysis to several harmonic components is not straightforward. The total friction variation caused by waviness is an average of the shear stress variations over the entire contact. The addition of another harmonic component complicates the shear stress distribution and influences the total friction variation in a non-linear way. In this section the case of two harmonic components is studied first to get an indication of the manner in which each harmonic component contributes to the total friction variation.

case	$\bar{\mathcal{A}}_1$	$\mathcal{W}_1$	$\bar{\mathcal{A}}_2$	$\mathcal{W}_2$
1	0.4	1/4	0.4	1/8
2	0.5	1/4	0.25	1/8
3	0.25	1/4	0.5	1/8
4	0.25	1/4	0.25	1/8
5	0.7	1/4	0.2	1/8
6	0.2	1/4	0.7	1/8

Table 6.1: Combinations of $\bar{\mathcal{A}}$ and $\mathcal{W}$ considered in the two waves study.

The relative friction variation $\delta\bar{\mu}/\bar{\mu}$ is calculated for the case of a waviness formed by two components in phase and with wavelengths $\mathcal{W}_1 = 1/4$ and $\mathcal{W}_2 = 1/8$ and varying amplitudes. The combinations of wavelength and amplitude considered are presented in Table 6.2. For each of them the friction variation $\delta\bar{\mu}/\bar{\mu}$ is calculated for more than 30 cases each time varying M, L, S, τ_0 and the cases considered IB1 to CY2 randomly. The calculated values of $\delta\bar{\mu}/\bar{\mu}$ are plotted as a function of $(\Gamma - 1)$ in Fig. 6.11.

The objective of this section is to seek wether it is possible to approximate the friction variations caused by two waves with an equivalent, single, wave. The predictions of the one wave curvefit for waves of amplitudes $\bar{\mathcal{A}}_i$ or $\sum\bar{\mathcal{A}}_i$ and wavelengths $\bar{\mathcal{W}}_i$ with $i = 1, 2$ are therefore plotted on Fig. 6.11 with the results of the full calculations. By comparing the single wave predictions with the results of the calculations it is possible to get an indication of the value of the amplitude and wavelength of the equivalent, single, wave which would result in the same friction variation $\delta\bar{\mu}/\bar{\mu}$ as the combination of two waves when used in Eq. 6.8.

For illustration, consider case 1, 2 and 3 in Fig. 6.11(a-c):

case 1: The amplitude is the same for both wavelengths. The calculated $\delta\bar{\mu}/\bar{\mu}$ data points lie between the curvefits obtained for $\bar{\mathcal{A}}$ and $2\bar{\mathcal{A}}$.

case 2: A low amplitude high frequency component $(\bar{\mathcal{A}}_2, \mathcal{W}_2)$ is superimposed on a high amplitude low-frequency component $(\bar{\mathcal{A}}_1, \mathcal{W}_1)$. The values of the data points are slightly above the curvefit of $(\bar{\mathcal{A}}_1, \mathcal{W}_1)$.

case 3: The opposite situation is considered: the high frequency component has a large amplitude $(\bar{\mathcal{A}}_2, \mathcal{W}_2)$ whereas the low-frequency component has a low amplitude $(\bar{\mathcal{A}}_1, \mathcal{W}_1)$. The values of $\delta\bar{\mu}/\bar{\mu}$ are close to the curvefit for $(\bar{\mathcal{A}}_2, \mathcal{W}_2)$.

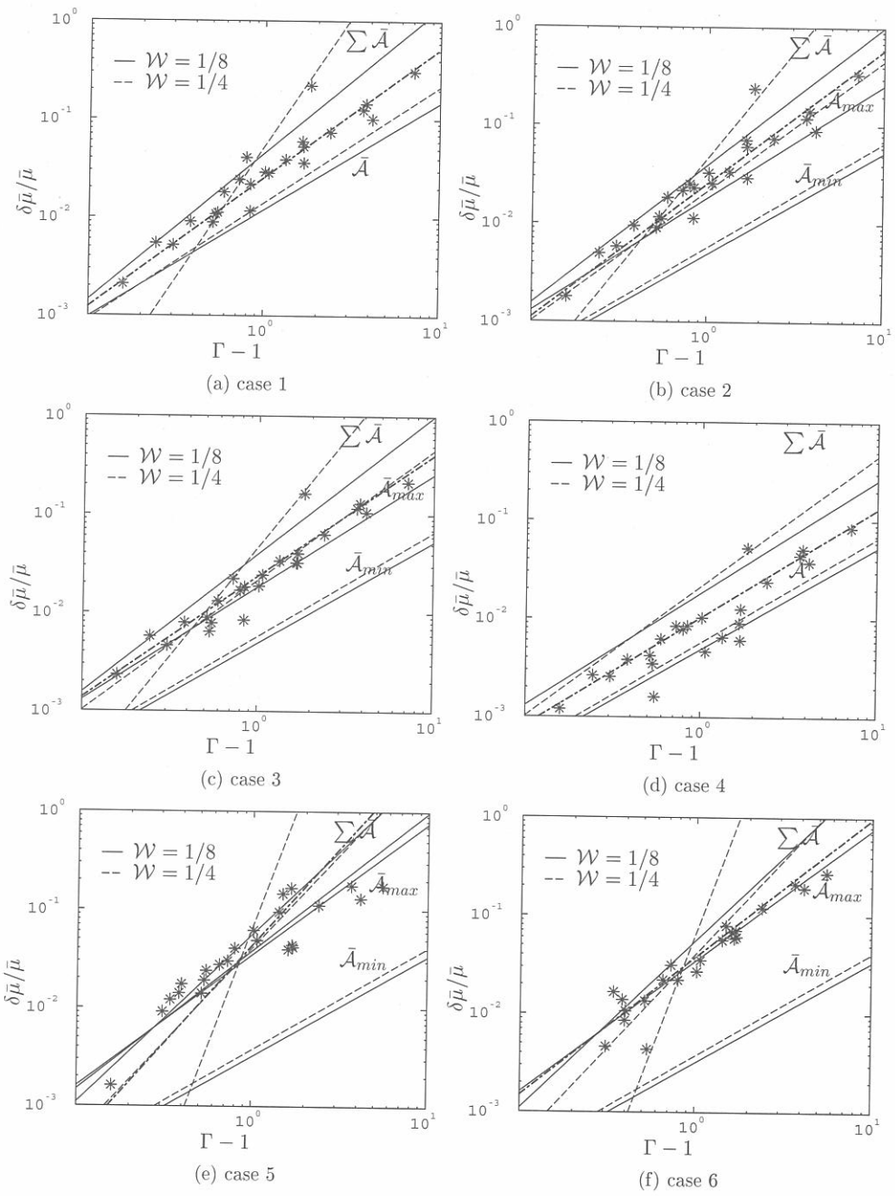

Figure 6.11: Friction variations $\delta\bar{\mu}/\bar{\mu}$ as a function of $(\Gamma - 1)$ for the different two-waves combinations, see Table 6.2. The bold dot-dash lines are given by Eq. 6.8 used with $\bar{\mathcal{A}}^*$ and $\mathcal{W}^*$.

It seems therefore that when one component has a clearly larger amplitude, the case of the combined waves behaves as that of one wave with an amplitude slightly larger than the maximum amplitude of its components. Its equivalent wavelength is close to the wavelength of the large amplitude component. When the amplitudes are almost equal an averaging process seems to take place.

Fom those observations, a possible definition of the equivalent wave's wavelength and amplitude is:

$$\bar{A}^* = \sqrt{\sum_i \bar{A}_i^2}, \qquad \mathcal{W}^* = \frac{\sum_i \bar{A}_i \mathcal{W}_i}{\sum_i \bar{A}_i} \tag{6.9}$$

The values of $\bar{A}^*$ and $\mathcal{W}^*$ corresponding to the cases described in Table 6.1 are listed in the Table 6.2. The curvefits obtained by using Eq. 6.8 with $\bar{A}^*$ and $\mathcal{W}^*$ given by Eq. 6.9 are shown in bold dot-dash lines in Fig. 6.11. For all cases they are a good approximation of the calculated values of $\delta\bar{\mu}/\bar{\mu}$ within the accuracy range of the one-wave analysis.

case	$\bar{A}_1$	$\mathcal{W}_1$	$\bar{A}_2$	$\mathcal{W}_2$	$\bar{A}^*$	$\mathcal{W}^*$
1	0.4	1/4	0.4	1/8	0.565	0.1875
2	0.5	1/4	0.25	1/8	0.559	0.208
3	0.25	1/4	0.5	1/8	0.559	0.167
4	0.25	1/4	0.25	1/8	0.353	0.1875
5	0.7	1/4	0.2	1/8	0.728	0.222
6	0.2	1/4	0.7	1/8	0.728	0.153

Table 6.2: Combinations of $\bar{A}$ and $\mathcal{W}$ considered in the two waves study together with the equivalent amplitudes and wavelengths obtained from Eq. 6.9.

Note however that Eq. 6.8 is much less sensitive to $\mathcal{W}$ than to $\bar{A}$. It is therefore difficult to validate the definition of $\mathcal{W}^*$ given in Eq. 6.9. Other combinations of $\mathcal{W}_i$ and $\bar{A}_i$ could probably be used with little difference on the predicted value of $\delta\bar{\mu}/\bar{\mu}$.

The friction variations caused by the combination of two harmonic components have been analyzed. It can be shown that an equivalent harmonic component of wavelength $\mathcal{W}^*$ and amplitude $\bar{A}^*$ exists giving the same value of $\delta\bar{\mu}/\bar{\mu}$ using Eq. 6.8 as that calculated for the combination of two harmonic components. The equivalent wavelength and amplitude are given by Eq. 6.9.

6.6 Real roughness

In the previous section it has been shown that the friction variation $\delta\bar{\mu}/\bar{\mu}$ caused by a waviness composed of two harmonic components can still be calculated using the single-wave

prediction formula Eq. 6.8. This is achieved by defining an equivalent, single component, waviness giving the same friction variation when using Eq. 6.8. The amplitude and wavelength of the equivalent waviness are given by Eq. 6.9. This section presents a verification of the validity of this combination for a complex rough profile described by a large number of harmonic components. An equivalent single wave is derived using Eq. 6.9. The friction variation predicted using Eq. 6.8 with this equivalent amplitude and wavelength is then compared to the result of full numerical calculations.

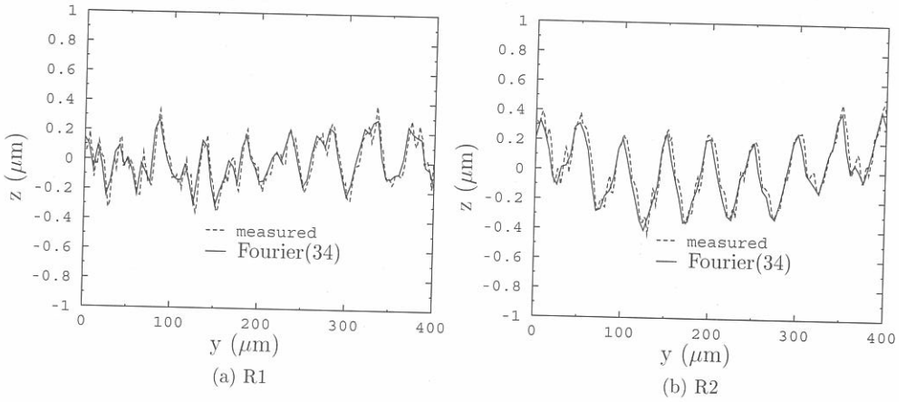

(a) R1 (b) R2

Figure 6.12: Measured roughness profiles and truncated (n=34) Fourier reconstruction.

The complex rough profiles are taken from measurements of real surface roughness of two balls used on the ball-on-disc machine finished with a predominantly longitudinal roughness lay. In order to use Eqs. 6.8 and 6.9 the roughness needs to be described as a sum of harmonic components. This is achieved by applying Fast Fourier Transform to the measured profiles. Concurrently full numerical simulations are performed for comparison with the rough profiles as an input. The complex rough profiles considered in the calculations are obtained by Inverse Fast Fourier Transform. However the reconstruction is restricted to the Fourier components with wavelengths larger or equal to 1/10th of the Hertzian half width of the contact because of the restricted range of frequencies that the numerical solver can accurately represent on a grid. Fig. 6.12 shows the two cross-section R1 and R2 taken from the 3D roughness distribution measured with an optical profiler and the results of the truncated Fourier reconstruction.

As the objective is to show that the combination formula can be used for more than two waves skipping the high-frequency information is not harmful as long as the main irregularities of the profile remain. Fig. 6.12 shows that this is the case. The reconstructed profile based on 34 harmonic components is sufficiently irregular to represent a good test

of the validity of Eq. 6.9. Note that although in reality the roughness varies slightly along the running direction, for the numerical calculations it is assumed to remain constant.

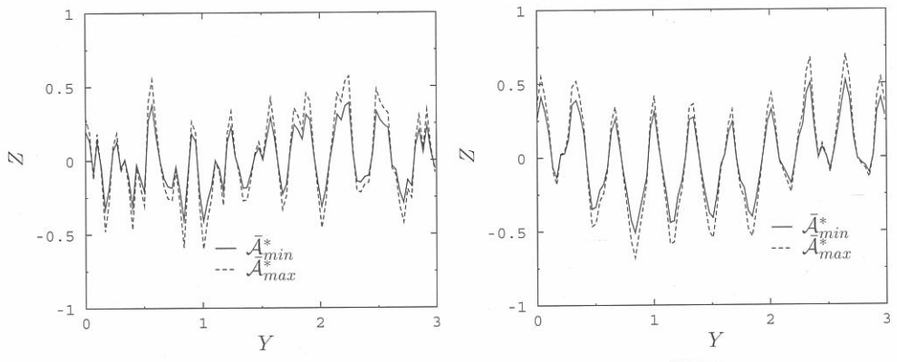

(a) R1 (b) R2

Figure 6.13: Dimensionless reconstructed roughness profiles R1 and R2. R1: $\bar{A}^* = 0.27$, 0.39 and $\mathcal{W}^* = 0.3$; R2: $\bar{A}^* = 0.31$, 0.41 and $\mathcal{W}^* = 0.36$.

The friction variation $\delta\bar{\mu}/\bar{\mu}$ caused by the profiles R1 and R2 on the upper surface is calculated for all six cases IB1 to CY2. Previously the value of $\bar{A}$ and the operating conditions could be varied independently. Now because the roughness information is defined out of the contact, the operating conditions have to be chosen such that $\bar{A}$ takes a certain value. In practice M and L values are taken to obtain a given film thickness in the contact using the Venner and Lubrecht film thickness formula [74] and therefore a certain relative amplitude of the roughness. For each of the six cases the values of M and L needed to obtain a constant value of $\bar{A}$ are slightly different. Two levels of roughness are considered for each rough profile: $\bar{A}^*$= 0.27 and $\bar{A}^*$= 0.39 for R1 and $\bar{A}^*$= 0.31 and $\bar{A}^*$= 0.41 for R2, see Fig. 6.13. The equivalent wavelengths are $\mathcal{W}^* = 0.3$ and $\mathcal{W}^* = 0.36$ for R1 and R2 respectively. For all configurations the maximum Hertzian pressure is $p_H = 1.07$ GPa. An example of the computed film thickness and pressure profile along the central line of the contact is given in Fig. 6.14 for R1 ($\bar{A}^* = 0.27$) and R2 ($\bar{A}^* = 0.31$).

Eq. 6.9 predicts the maximum friction variation $\delta\bar{\mu}/\bar{\mu}$ and should be compared to the maximum friction variation calculated for both profiles. Obviously the value of $\delta\bar{\mu}/\bar{\mu}$ obtained with the numerical solver depends on the lateral position of the profile. To get an approximation of the maximum friction variation $\delta\bar{\mu}/\bar{\mu}$ has been calculated for nine positions of the roughness profiles representing a total shift of $\Delta Y = 2$. Instead of using the largest of the values calculated for the nine cases to represent the maximum friction variation a statistical approach is used. From the set of results an average friction

variation $\overline{(\delta\bar{\mu}/\bar{\mu})}$ and a standard deviation σ can be calculated. A good representation of the maximum friction variation is then $\delta\bar{\mu}/\bar{\mu} \sim \overline{(\delta\bar{\mu}/\bar{\mu})} + 2\sigma$.

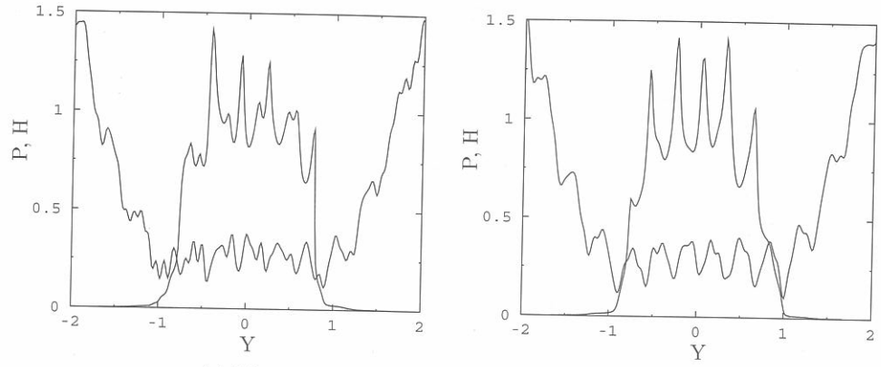

(a) R1 (b) R2

Figure 6.14: Film thickness and pressure profile for R1 ($\bar{A}^* = 0.27$) and R2 ($\bar{A}^* = 0.31$). IB1 is considered.

Fig. 6.15 compares $\delta\bar{\mu}/\bar{\mu}$ obtained by full numerical simulations and the results of Eq. 6.8 used with ($\bar{A}^*$, $\mathcal{W}^*$) derived from Eq. 6.9. For indication the interval $\delta\bar{\mu}/\bar{\mu} \pm \sigma$ is shown. The predictions of Eq. 6.9 and Eq. 6.8 are slightly below the calculated values of $\delta\bar{\mu}/\bar{\mu}$ for R1 and slightly above for R2. For both profiles, the agreement is good except in the case of CY1. Recall that CY1 is the case that also differed most from the others with respect to $\delta\bar{\mu}/\bar{\mu} = f(\bar{\tau}_c)$ behaviour. Even when plotted using $(\Gamma - 1)$ as a parameter the data points for CY1 sometimes stray away significantly above the curvefit of Eq. 6.8. With the rough profile, those differences may add up and eventually the difference between the calculated and predicted $\delta\bar{\mu}/\bar{\mu}$ can become quite large.

Nevertheless the comparison with full numerical calculations shows that Eq. 6.9 can be used quite well for a combination of more than two harmonic components. It appears that Eq. 6.9 can be applied to the Fourier transform of any longitudinal rough surface. This enables the calculation of the friction changes induced by an arbitrary roughness distribution with a similar accuracy as was obtained for the single wave study in a simple way.

The validity of Eqs. 6.8 and 6.9 needs to be checked experimentally. However the complexity of the experimental set-up required which should be able to measure small friction changes with great accuracy and repeatability and the difficulty in manufacturing well controlled (close to sinusoidal) longitudinal roughness put this verification beyond reach of this thesis.

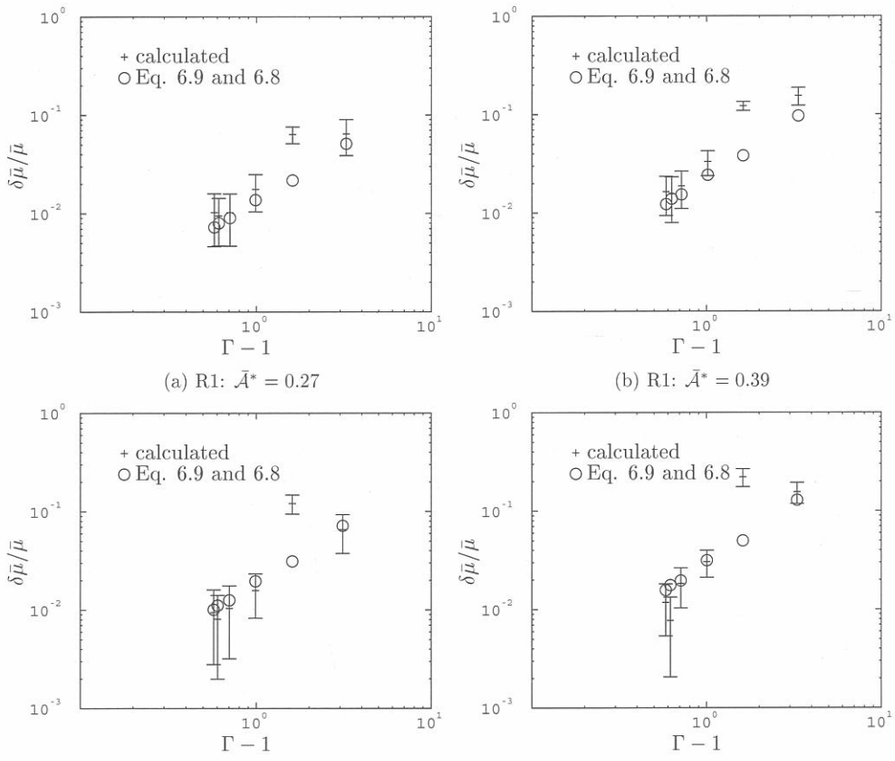

(a) R1: $\bar{A}^* = 0.27$

(b) R1: $\bar{A}^* = 0.39$

(c) R2: $\bar{A}^* = 0.31$

(d) R2: $\bar{A}^* = 0.41$

Figure 6.15: Comparison of the friction variation $\delta\bar{\mu}/\bar{\mu}$ obtained for the reconstructed profiles by full numerical calculation and by Eq. 6.9 and Eq. 6.8. From left to right IB2, CR1, IB1, CY2, CY1 and CR2.

6.7 Conclusions

The influence of sinusoidal waviness on the friction coefficient has been studied extensively. A general predictive formula has been derived, Eq. 6.8, relating the changes in friction $\delta\bar{\mu}/\bar{\mu}$ to the out-of-contact geometry of the waviness and a parameter Γ characterizing the response of the contact to pressure variations.

The analysis has been extended to several harmonic components. It is shown that the

effect of several components on the friction variation can be modeled by defining an equivalent single wave. The wavelength and amplitude of the equivalent wave are obtained by combining in a non-linear way the wavelengths and amplitudes of the various components. The validity of the combination formula, Eq. 6.9, has been verified numerically in the case of real rough profiles.

Eq. 6.8 and Eq. 6.9 give the possibility to evaluate the friction changes introduced by any arbitrary longitudinal roughness. The real roughness distribution can be decomposed in harmonic components using Fourier transform which can subsequently be used to calculated the equivalent wave and its effect on friction.

Conclusions and recommendations

In this thesis the friction generation mechanisms in rolling/sliding EHL contacts have been studied extensively using a numerical solver based on multilevel techniques.

The solver has been used at first to compute systematically the coefficient of friction of smooth isothermal EHL contacts for a wide range of operating conditions and contact configurations. An analysis of the results shows that the mechanisms of friction generation can be characterized by a single parameter $\bar{\tau}_c$ valid for both the Eyring and the limiting shear stress models. For each type of rheological model a simple, easy to use, engineering formula has been derived giving the friction coefficient as a function of $\bar{\tau}_c$. By comparing the formulas for both models a relation can be found between the Eyring stress τ_0 and the limiting shear stress τ_L such that both models predict the same friction coefficient. This relation could prove useful to remedy to the fact that no independent data exist concerning the value of τ_0 hampering an independent prediction of the friction coefficient with the Eyring model. For the limiting shear stress model, however, a totally independent validation is possible. A close agreement was observed between the calculations and experimental results published in the literature.

The thermal effects due to frictional heating at high shear rates have been taken into account by means of a simplified analysis. The contact is assumed to behave as a thermal "dry contact" for which the value of the friction coefficient is given by the friction mastercurves derived for the isothermal case. The maximum surface temperature increase and friction reduction can then simply be calculated. The predictions of simplified model have been successfully compared to results of full numerical analyses and to experimental data.

Finally the numerical solver has been used to study the effect of longitudinal roughness on friction in the same systematic way. For a single wave the variations of the friction coefficient caused by the introduction of roughness can be predicted with a simple formula as a function of the out-of-contact amplitude and wavelength of the waviness and a newly derived parameter characterizing the response of the contact to pressure variations. Then it is shown that the effects on friction of the combination of several waves can be predicted by considering an equivalent single wave. In that way the friction variations caused by any complex longitudinal roughness distribution can be estimated using the single-wave formula.

The present work can be extended in several ways. Some of the possible directions of further research are listed below.

In addition to the rheological models studied in this thesis, Bair [9] has recently applied shear thinning to describe the non-Newtonian behaviour of the lubricant. It seems that this model could explain some of the discrepancies between measured and predicted traction curves, see Sect. 4.3. Moreover this model has a strong physical basis and its parameters can be measured independently. It would certainly be worthwhile to redo the analysis with this model to see if a mastercurve can be obtained there too.

An obvious extension to Chapt. 6 is the study of the effects of transverse roughness. It is likely that the current prediction formula would remain valid as the model is too coarse to distinguish differences in the in-contact geometry of the waviness or out of phase effects in the pressure distribution for instance. Nevertheless a thorough verification of this hypothesis is required.

An experimental validation of the effects of roughness is required. Simple surface roughness should be manufactured in order to be able to verify both the single-wave prediction formula and the combination formula. An experimental set-up should be developed ensuring high accuracy and repeatability in the measurement of the friction coefficient. Ideally, the measurement of the film thickness at the same time as the friction measurements would allow to check if the conditions in terms of relative roughness amplitude used in the calculations are correct. In addition precautions should be taken to ensure isothermal conditions.

Finally, in addition to the problem of which rheological model to trust, the accurate prediction of friction relies first and foremost on an accurate knowledge of the lubricant characteristics under the conditions experienced in rolling/sliding EHL contacts. The data available in the literature is scarce and covers a limited range. There is a great need for systematic measurements.

Acknowledgments

This research was supported by and conducted at SKF Engineering and Research Centre in Nieuwegein. I gratefully acknowledge their support.

I am most thankful to my mentors, Kees Venner from the University of Twente, and Piet Lugt from SKF ERC for their continuous support and enthusiasm. Thanks also to John Tripp for many interesting discussions and suggestions and to Harry Hoeijmakers for his valuable contribution to this thesis.

I have been very fortunate to be able to work at SKF ERC for the last four years. A lot of people have contributed to make of this time a very pleasant one, among them Marie-Laure Dumont, Benny Wemekamp, Ralph Meeuwenoord, Rinke Vos, Guillermo Morales-Espejel, Antonio Gabelli, Bengt Rydell and Hans Kuypers. From SKF I also thank Stathis Ioannides for his encouraging support.

Many thanks also to the members of the Tribology group at the University of Twente who made me feel that I belonged there during my rare and short visits at the university: Jan-Willem Sloetjes, Marc Masen, Qiang Liu, Patrick Pirson, Wijtze ten Napel, Walter Lette, Belinda Bruinink, Dik Schipper and Matthijn de Rooij.

I would also like to thank the students who worked with me for their master's thesis: Robert Nagelhoud and Emil Coyajee.

The last four years have been quite an intense period during which I rejoiced a few times, cursed a lot but all in all learned a lot. I would like to thank all the persons that helped me along this path. Thanks especially to Renske Munnikes. I also thank my wife, Anne-Laure, who contributed a lot to the balance between rejoicing and curse with her strategic and timely advises. I guess the figures and equations in this book would have looked much the same without her but I would have looked much worse.

Benoit Jacod

Nieuwegein, August 2002

Appendix: Lubricant characteristics

In this appendix the characteristics of the lubricants used for the experimental validations in Chapters. 4, 5 and 6 are listed. The Free Volume parameters of Shell TT9 used in Sect. 6.1 are also given. The origin of the values is indicated by referring to the paper in which they have been reported.

Viscosity

The values of the Free-Volume parameters are given together with the value of α and η_0.

Lubricant	η_g	T_{g0}	A_1	$A_2(GPa^{-1})$	B_1	$B_2(GPa^{-1})$	C_1	C_2	Ref.
5P4E	10^{12}	-28.8	134.2	1.929	4.815	0.16	16.01	20.69	[78]
Santotrac 50	10^{7}	-46.9	92.92	2.6	0.2965	16.275	10.51	20.70	[7]
HVI 650	10^{7}	-37.51	278.5	0.4082	0.2008	24.09	10.68	34.8	[8]
DOP	10^{7}	-80.5	185.6	0.709	0.1298	31.55	11.88	47.69	[7]
N1	10^{12}	-85.4	130	1.617	0.262	9.2	16.58	27.08	[78]
TT9	10^{7}	-76	228.3	0.7645	0.188	25.84	11.45	30.26	[10]

Table A.1: Free Volume parameters for the lubricants considered in this thesis.

Lubricant	T(^{o}C)	η_0(Pas)	$\alpha(GPa^{-1})$	Ref.	K(W/m/K)
5P4E	100	0.017	15.1	[28]	0.133
Santotrac 50	40	0.0348	29.6	[28]	0.104
	60	0.0131	22.8		
	100	0.0048	16.8		
HVI650	60	0.14	22.9	[28]	0.125
	80	0.071	19.9		
	100	0.03	17.7		
DOP	90	0.0049	13.3	[59]	0.1*
N1	80	0.0217	23.2	[70]	0.1*

Table A.2: Lubricant characteristics at the temperatures used in this thesis. For 5P4E, Santotrac 50 and HVI 650 at 40, 80 and 100(^{o}C) the values are extrapolated from the values at 30, 60, 90 and 120(^{o}C). * For N1 and DOP the value of K is assumed.

Limiting shear stress

The value of the limiting shear stress proportionality coefficient γ have been collected in the literature to establish the variation of γ with temperature used in Chapt. 5.

5P4E							
T	-10	10	20	38	40	60	80
γ	0.141	0.131	0.1	0.087	0.096 0.083	0.076	0.065
Ref.	[3]		[6]	[5]	[3]/[6]	[3]	[6]
Santotrac 50							
T	-40	-20	-10	25	40	70	100
γ	0.156	0.145	0.131	0.111	0.14	0.091	0.059
Ref.	[3]			[5]	[41]		
HVI 650							
T	26		40		70	100	
γ	0.0463		0.036		0.032	0.028	
Ref.	[5]		[41]				
N1							
T	-40	-20	0	25	26	46	60	67
γ	0.116	0.101	0.091	0.075 0.0875	0.072 0.07	0.053 0.051	0.0495	0.041
Ref.	[3]			[5]				

Table A.3: Limiting shear stress proportionality coefficient γ. When two values are mentioned for one temperature, they have been obtained under different pressures.

The decrease of the γ with temperature is approximated by the following equation:

$$\gamma = \gamma_r \exp(-\omega(T + 273)) \tag{A.10}$$

with T in ^{o}C. The fit of Eq. A.10 with the measured data can be seen in Fig. A.1. The parameters γ_r and ω are given in Table A.4.

Lubricant	γ_r	ω
N1	0.862	0.00842
5P4E	1.644	0.00928
Santotrac 50	0.7	0.0063
HVI 650	0.315	0.00662

Table A.4: Parameters of Eq. A.10 approximating the decrease of γ with temperature.

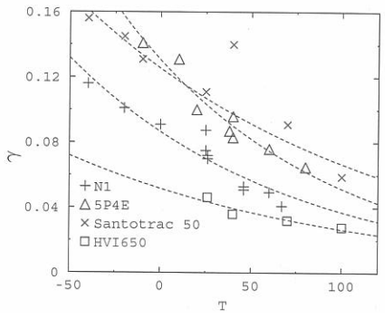

Figure A.1: Limiting shear stress proportionality coefficient γ as a function of the temperature. Dashed lines: Eq. A.10.

Eyring stress:

The values of the Eyring stress have been obtained from the slope of the traction curves by Evans and Johnson [28] and Moore [59]. They are recalled in Table A.5.

Lubricant	T(^{o}C)	p_H(GPa)	τ_0(MPa)	Ref.
5P4E	100	0.6	2.7	[28]
Santotrac 50	100	0.8	5	[28]
HVI650	100	0.8	7	[28]
DOP	90	1.04 1.27	9 10	[59]

Table A.5: Measured values of the Eyring stress τ_0.

References

[1] **Ai, X., Cheng, H.S.**, 1995, "The effect of surface texture on EHL point contacts", Trans. ASME, Journal of Tribology, **118**, 59-66.

[2] **Atkinson, K.E.**, 1989, "An Introduction to Numerical Analysis (2nd ed.)", John Wiley & Sons, United States, ISBN 0-471-62489-6.

[3] **Bair, S., Winer, W.O.**, 1979, "Shear strength measurements of lubricant at high pressure", Trans. ASME, J. Lubr. Tech., **101**, 251-257.

[4] **Bair, S., Winer, W.O.** , 1979, "A rheological model for elastohydrodynamic contacts based on primary laboratory data ", Trans. ASME, J. Lubr. Tech., **101**, 258-265.

[5] **Bair, S., Winer, W.O.**, 1982, "Some observations in high pressure rheology of lubricants", Trans. ASME, J. Lubr. Tech., **104**, 357-364.

[6] **Bair, S., Winer, W.O.**, 1992, "The high pressure high shear stress rheology of liquid lubricants", Trans. ASME, Journal of Tribology, **114**, 1-13.

[7] **Bair, S., Winer, W.O.**, 2000, "The pressure-viscosity coefficient at Hertzian pressure and its relation to concentrated contact traction", *Proc. 26th Leeds-Lyon Symposium on Tribology*, 433-443.

[8] **Bair, S.**, 2000, "Pressure-viscosity behavior of lubricants to 1.4 GPa and its relation to EHD traction", Tribology Trans., **43**, 91-99 .

[9] **Bair, S.**, 2001, "Ordinary shear thinning behavior in liquids and its effect upon EHD traction", *Proc. 27th Leeds-Lyon Symposium on Tribology*, 733-742 .

[10] **Bair, S.**, 2001, "The variation of viscosity with temperature and pressure for various real lubricants", Trans. ASME, Journal of Tribology, **123**, 433-436.

[11] **Bair, S.**, 2002, "The shear rheology of thin compressed liquid films", Proc Instn. Mech. Engrs., Part J, **216**, 1-17.

[12] **Barus, C.**, 1891, "Note on the dependence of viscosity on pressure and temperature", Proc. Am. Acad. Arts Sci., **27**, 13.

[13] **Bos, J.**, 1995, "Frictional heating of tribological contacts", PhD. Thesis, University of Twente, Enschede, The Netherlands, ISBN 90-9008920-9.

[14] **Brandt, A.**, 1984, "Multigrid Techniques: 1984 Guide with Applications to Fluid Dynamics", GMD-Studien: Nr. 85.

[15] **Brandt, A., Lubrecht, A.A.**, 1990, "Multilevel matrix multiplication and fast solution of integral equations", J. of Comp. Phys., **90**, 2, 348-370.

[16] **Bridgeman, P.W.**, 1942, Proc. Am. Acad. Arts Sci., **74**, 399-424.

[17] **Briggs, W.L.**, 1987, "A Multigrid Tutorial", Society for Industrial and Applied Mathematics, Philadelphia, Pennsylvania.

[18] **Cann, P.M.E., Spikes, H.A.**, 1989, "Determination of the shear stress of lubricants in elastohydrodynamic contacts", Tribology Transactions, **32**, 414-422.

[19] **Cann, P.M.E., Hutchinson, J., Spikes, H.A.**, 1996, "The development of a spacer layer imaging method (slim) for mapping elastohydrodynamic contacts", Tribology Transactions, **39**, 915-921.

[20] **Conry, T.F., Wang, S., Cusano, C.**, 1987, "A Reynolds-Eyring equation for elastohydrodynamic lubrication in line contacts", Trans. ASME, Journal of Tribology, **109**, 648-658.

[21] **Crook, A.W.**, 1961, "The lubrication of rollers, Part III", Phil. Trans. A, **254**, 237-258.

[22] **Dowson, D., Higginson, G. R.**, 1959, "A numerical solution to the elastohydrodynamic problem ", J. Mech. Eng. Sci. 1, **1**, 6-15.

[23] **Dowson, D., Higginson, G. R.**, 1966, "*Elastohydrodynamic Lubrication, The Fundamentals of Roller and Gear Lubrication*", Pergamon Press, Oxford.

[24] **Ehret, P., Dowson, D., Taylor, C.M.**, 1998, "On lubricant transport conditions in elastohydrodynamic conjunctions ", Proc. Roy. Soc., London, series A, **454**, 763-787.

[25] **Ehret, P., Dowson, D., Taylor, C.M.**, 1999, "Thermal effects in elliptical contacts with spin conditions", *Proc. 25th Leeds-Lyon Symposium on Tribology*, 685-703.

[26] **Ehret, P., Chevalier, F., Dowson, D., Taylor, C.M., Okamura, H., Sano, T.**, 2000, "Traction in EHL elliptical contacts with spin conditions ", *Proc. 26th Leeds-Lyon Symposium on Tribology*, 71-84.

[27] **Elsharkawy, A., Hamrock, B.**, 1991, "Subsurface stresses in micro-EHL line contacts", Trans. ASME, Journal of Tribology, **113**, 645-657.

[28] **Evans, C.R., Johnson, K.L.**, 1986, "The rheological properties of EHD lubricants", Proc. Instn Mech. Engrs, Part C, **200**, 303-312.

[29] **Evans, C.R., Johnson, K.L.**, 1986, "Regimes of traction in elastohydrodynamic lubrication", Proc. Instn. Mech. Engrs., Part C, **200**, 313-324.

[30] **Gecim, B., Winer, W.O.** , 1980, "Lubricant limiting shear stress effect on EHD film thickness ", Trans. ASME, J. Lubr. Tech., **102**, 213.

[31] **Glovnea, R.P., Spikes, H.A.**, 1995, "Mapping shear stress in elastohydrodynamic contacts", Tribology Transactions, **38**, 932-940.

[32] **Gohar, R., Cameron, A.**, 1963, "Optical measurements of oil film thickness under elastohydrodynamic lubrication", Nature, **200**, 458-459.

[33] **Greenwood, J.A., Morales-Espejel, G.E.**, 1993, "The behaviour of real transverse roughness in a sliding EHL contact", *Proceedings 19th Leeds-Lyon Symposium on Tribology*, 227-236.

[34] **Greenwood, J.A.**, 2000, "Two-dimensional flow of a non-Newtonian lubricant", Proc. Instn. Mech. Engrs., Part J, **214**, 29-41.

[35] **Greenwood, J.A.**, Private communication.

[36] **Grieve, R.S.A., Spikes, H.A.**, 2000, "Temperature and shear stress in thin EHD contacts", *Proc. 26th Leeds-Lyon Symposium on Tribology*, 511-522.

[37] **Hamrock, B.J., Dowson, D.**, 1976, "Isothermal elastohydrodynamic lubrication of point contacts, part I, theoretical formulation", Trans. ASME, J. Lubr. Tech., **98**, 223-229.

[38] **Hamrock, B.J., Dowson, D.**, 1977, "Isothermal elastohydrodynamic lubrication of point contacts, part III, fully flooded results ", Trans. ASME, J. Lubr. Tech., **99**, 264-276.

[39] **Harris, T.A.**, 2001, "Rolling bearing analysis", 4th Ed., Wiley-Interscience, ISBN 0-471-35457-0.

[40] **Hirst, W., Moore, A.J.**, 1974, "Non-Newtonian behaviour in elastohydrodynamic lubrication", Proc. Roy. Soc. London, **33**, 101-113.

[41] **Hoglund, E., Jacobson, B.**, 1986, "Experimental Investigation of the shear strength of lubricants subjected to high pressure and temperature", Trans. ASME Journal of tribology, **108**, 571-578.

[42] **Holt, C.A., Evans, H.P., Snidle, R.W.**, 1996, "Solution of the non-Newtonian elastohydrodynamic problem for circular contacts based on a flow continuity method", Proc. Instn. Mech. Engrs., Part J, **210**, 247-258.

[43] **Hsiao, H.-S., Hamrock, B.J.**, 1992, "A complete solution for thermal-elastohydrodynamic lubrication of line contacts using circular non-Newtonian fluid model", Trans. ASME, Journal of Tribology, **114**, 540-552.

[44] **Hsiao, H.-S., Hamrock, B.J.**, 1994, "Non-Newtonian and thermal effects on film generation and traction reduction in EHL line contact conjunctions", Trans. ASME, Journal of Tribology, **116**, 559-568.

[45] **Iivonen, H.T., Hamrock, B.J.**, 1991, "A non-Newtonian fluid model incorporated into elastohydrodynamic lubrication of rectangular contacts", Wear, **143**, 297-305.

[46] **Jacobson, B., Hamrock, B.J.** , 1984, "Non-Newtonian fluid model incorporated into elastohydrodynamic lubrication of rectangular contacts", Trans. ASME, Journal of Tribology, **106**, 275-284.

[47] **Jacobson, B.O.**, 1989, "A high pressure-short time shear strength analyser for lubricants", Trans. ASME, Journal of Tribology, **107**, 220-223.

[48] **Johnson, K.L., Tevaarwerk, J.L.**, 1977, "Shear behaviour of elastohydrodynamic oil films", Proc. Roy. Soc. London, series A, **356**(12), 215-236.

[49] **Johnson, K.L.**, 1993, "Non-Newtonian effects in elastohydrodynamic lubrication", *Proc. 19th Leeds-Lyon Symposium on Tribology*, 15-26.

[50] **Kellstrom, E.M.**, 1979, "Rolling contact guidance of rollers in spherical roller bearings", Joint ASME/ASLE Lubrication Conference, number 17-Lub-23.

[51] **Kim, K.H., Sadeghi, F.**, 1991, "Non-Newtonian Elastohydrodynamic Lubrication of Point Contacts", Trans. ASME, Journal of Tribology, **113**, 703-711.

[52] **Kim, H.J., Ehret, P., Taylor, C.M.**, 2001, "Thermal elastohydrodynamic analysis of circular contacts, Part 2: non-Newtonian model", Proc. Instn. Mech. Engrs., Part J., **215**, 353-362.

[53] **Lee, R-T., Hamrock, B.J.**, 1990, "A circular non-Newtonian model: Part 1-used in elasto-hydrodynamic lubrication", Trans. ASME, Journal of Tribology, **112**, 386-496.

[54] **Lee, R-T., Hsu, C.H., Kuo, W.F.**,1995, "Multilevel solution for thermal elastohydrodynamic lubrication of rolling/sliding circular contacts", Tribology International, **28**, 541-552.

[55] **Lubrecht, A.A.**, 1987, "The Numerical solution of elastohydrodynamically lubricated line- and point contact problem using Multigrid techniques", PhD. Thesis, University of Twente, Enschede, The Netherlands, ISBN 90-9001583-3.

[56] **Ma, M.-T.**, 1998, "Effects of the non-Newtonian behavior of lubricants on the temperature, traction, and film thickness in an elliptical EHD contact under heavy loads", Trans. ASME, Journal of Tribology, **120**, 685-694.

[57] **Masen, M.A., Venner, C.H., Lugt, P.M., Tripp, J.H.**, 2002, "Effects of surface micro-geometry on the lift-off speed of an EHL contact", Tribology Transactions, **45**, 21-30.

[58] **Moes, H.**, 1992, "Optimum similarity analysis with applications to elastohydrodynamic lubrication", Wear, **159**, 57-66.

[59] **Moore, A.J.**, 1981, "The Derivation of basic liquid flow properties from disc machine traction tests", *Proc. 7th Leeds-Lyon Symposium on Tribology*, 289-295.

[60] **Morales-Espejel, G.E., Greenwood, J.A., Venner, C.H.**, 2000, "Kinematics of real roughness in elastohydrodynamically lubricated line contacts unsing Fourier analysis", Proc. Instn. Mech. Engrs., Part J, **214**, 523-534.

[61] **Nagaraj, H.S., Sanborn, D.M., Winer, W.O.**, 1978, "Direct surface temperature measurement by infrared radiation in elastohydrodynamic contacts and the correlation with the Blok flash temperature theory", Wear, **49**, 43-58.

[62] **Nijenbanning, G., Venner, C.H., Moes, H.**, 1994, "Film thickness in elastohydrodynamically lubricated elliptic contacts", Wear, **176**, 217-229.

[63] **Petrusevitch, A.I.**, 1951, "Fundamental conclusions from the contact-hydrodynamic theory of lubrication ", Izv. Akad. Nauk. SSSR (OTN), **2**, 209-233.

[64] **Ramesh, K.T., Clifton, R.J.**, 1987, "A pressure shear plate experiment for studying the rheology of lubricants at high pressures and high shearing rates ", Trans. ASME, Journal of Tribology, **109**, 215-222.

[65] **Ramesh, K.T.** , 1989, "On the rheology of a traction fluid", Trans. ASME, Journal of Tribology, **111**, 614-619.

[66] **Roelands, C.**, 1966, "*Correlational aspects of the viscosity-temperature-pressure relationship of lubrication oils*", PhD Thesis, Technische Hogeschool Delft, The Netherlands.

[67] **Sharif, K.J., Morris, S.J., Evans, H.P., Snidle, R.W.**, 2001, "Comparison of non-Newtonian EHL models in high sliding applications", *Proc. 27th Leeds-Lyon Symposium on Tribology*, 787-796.

[68] **Sui, P.C., Sadeghi, F.**, 1991, "Non-Newtonian thermal elastohydrodynamic lubrication", Trans. ASME, Journal of Tribology, **113**, 390-397.

[69] **Trachman, E.G., Cheng, H.S.**, 1972, "Thermal and non-Newtonian effects on traction in elastohydrodynamic contacts", Proc. Instn. Mech. Engrs. .

[70] **Turchina, V., Sanborn, D.M., Winer, W.O.**, 1974, "Temperature measurements in sliding elastohydrodynamic point contacts", Trans. ASME, J. Lubr. Tech., **96**, 464-471.

[71] **Venner, C.H.**, 1991, "Multilevel solution of the EHL line and point contact problems", PhD. Thesis, University of Twente, Enschede, The Netherlands, ISBN 90-9003974-0.

[72] **Venner, C.H., Lubrecht, A.A.**, 1999, "Amplitude reduction of anisotropic harmonic surface patterns in EHL circular contacts under pure rolling", *Proc. 25th Leeds-Lyon Symposium on Tribology*, 151-162.

[73] **Venner, C.H., Kaneta, M., Nishikawa, H., Jacod, B.**, 2000, "Effects of waviness on the film thickness of a circular EHL contact under rolling/sliding", *Proc. International Tribology Conference, Nagasaki*, 631-636.

[74] **Venner, C.H., Lubrecht, A.A.**, 2000, "Multilevel methods in lubrication", *Tribology Series*, **37**, Ed. D. Dowson, ISBN 0-444-50503-2.

[75] **Wijnant, Y.H.**, 1998, "Contact dynamics in the field of elastohydrodynamic lubrication", PhD. Thesis, University of Twente, Enschede, The Netherlands, ISBN 90-36512239.

[76] **Wang. H., Hua, D.Y., Zhang, H.H.**, 1988, "A full numerical EHL solution for line contacts under pure rolling conditions with a non-Newtonian rheological model", Trans. ASME, Journal of Tribology, **114**, 583-586.

[77] **Xu, G., Sadeghi, F.**, 1996, "Thermal analysis of circular contacts with measured roughness", Trans. ASME, Journal of Tribology, **113**, 473-483.

[78] **Yasutomi, S., Bair, S., Winer, W.O.**, 1984, "An application of Free Volume model to lubricant rheology", Trans. ASME, Journal of Tribology, **106**, 291-303.